THE UNIVERSITY OF CHICAGO

IDENTIFYING, INVESTIGATING, AND MODULATING ANTI-CD19 CAR T CELLS FOR LARGE B-CELL LYMPHOMA

A DISSERTATION SUBMITTED TO
THE FACULTY OF THE DIVISION OF THE BIOLOGICAL SCIENCES
AND THE PRITZKER SCHOOL OF MEDICINE
IN CANDIDACY FOR THE DEGREE OF
DOCTOR OF PHILOSOPHY

INTERDISCIPLINARY SCIENTIST TRAINING PROGRAM:
BIOCHEMISTRY AND MOLECULAR BIOPHYSICS

BY
YIFEI HU

CHICAGO, ILLINOIS
DECEMBER 2022

TABLE OF CONTENTS

LIST OF FIGURES

LIST OF TABLES

ACKNOWLEDGEMENTS

This body of work is impossible without the collective support of my mentorship network, collaborators, and community. While the inspiration and central ideas behind this work were generally conceived by me. However, the execution of these projects and the emotional support I needed originated from many individuals, some of whom are not formally acknowledged.

I am deeply grateful to my primary mentor, Dr. Jun Huang. Jun fostered an environment where students drive self-conceived projects and own their successes/failures. As someone who aspires towards and values independence, I love the creative energy and multidisciplinary teamwork that demarked the Huang lab. As a mentor, Jun's greatest contribution to my future success is by emboldening my efforts on the broader scientific and clinical questions. I was asked many times in a multitude of ways whether and how my ideas, experiments, and findings advance the biggest questions in the cellular therapy field. Ultimately, Jun helped pull me away from thinking like a technician and push me towards thinking like an investigator. Furthermore, I never had to worry about financial restrictions that limit the scope of my projects. In addition to Jun, I am also grateful to every other member of my thesis committee (Drs. Erin Adams, Justin Kline, and Hans Schreiber). Erin met with me many times to provide guidance as a mentor and encourage me to work sustainably while preventing burnout. Justin provided me access to all clinical biospecimens, connected me with members of the cellular therapy community, and facilitated many experiments. Hans shared inspiring stories and important pieces of wisdom about the optimal career trajectory of a physician-scientist.

In addition, I thank all my collaborators who enabled this work. Many of these findings would not be possible without Guoshuai (Daniel) Cao, who performed single-cell data analysis. As the first senior student I met in the Huang lab, Daniel uniquely has influenced my entire PhD experience and informed almost every important decision. We differ in some organizing principles but share a set of core values centered on academic freedom and personal growth. Furthermore, I thank Nick Asby and Erting Tang. Nick, the quintessential team player and cloning master, can magically decrease the stress of anyone he interacts with. I am indebted to his special patience, soothing demeanor, and willingness to help in all situations. Erting has been the most capable, diligent, and reliable collaborator, and we enjoyed doing many of the most exciting experiments together. Finally, I want to thank my undergraduate mentees, Ali Rahman and Ashima Thusu, who gave me the privilege of being their mentor as they pursued medicine. My experiences as a mentor will shape how I nurture future mentees when I run my own lab.

Outside the university environment, I thank all my family and friends who supported my journey towards becoming a physician-scientist. My mom, dad, and grandparents taught me throughout my childhood to be kind unto others, to stay optimistic and calm in the face of adversity, and to value long-term educational gains over short-term pursuits. I also benefited from the enduring support of my girlfriend, best (lad) friend, and countless unnamed individuals who encouraged me and processed with me through many problems that inevitably come up during PhD. I have sufficient self-awareness to know that I was not always easy or fun to be around, especially if too much was going on in my mind. After all, my idealism was replaced with realism, I struggled with disappointment and anxiety, and I painfully learned that that people do not automatically work well together. As I went through various personal transformations, I surely felt burdensome to family and friends who listened to and empathized with my ramblings.

Finally, I wish to highlight what drew me towards science in the first place. My God seeded within my heart an undying flame and insatiable hunger for truth. Throughout my journeys into the exotic worlds of mathematics, quantum mechanics, organic chemistry, microbiology, and immunology, I have felt this seed blossom into a captivation for unveiling the liminal edge between nature’s order and mystery. My God provided me with natural curiosity and an identity as a scientist. As I continue down my path in science, my God has and will continue to guide and strengthen me through whatever lies ahead.

ABSTRACT

Anti-CD19 chimeric antigen receptor (CAR) T-cell therapy has improved treatment options for patients with relapsed/refractory diffuse large B-cell lymphoma (r/r DLBCL). During anti-CD19 CAR T-cell therapy, the patient's T cells are transduced with an anti-CD19 CAR – a synthetic immunoreceptor that directs the T cell to recognize, activate, proliferate, and kill in response to $CD19^+$ lymphoma cells. Despite encouraging ~40% complete response rates, non-responders generally succumb to their disease. Hence, improved CAR T-cell therapy formulations with higher response rates are urgently needed in the clinic. My research questions, experiments, findings, and conclusions in this dissertation are organized around this central clinical problem. In this body of work, after providing a brief introduction to CD19-directed CAR T-cell therapy (Section I), I first reviewed the existing methods used by CAR T-cell scientists to detect and investigate the CAR across the genomic, transcriptomic, proteomic, and organismal levels (Section II). With this background in mind, I designed, constructed, and validated antigen multimers as specific, sensitive, precise, and multifunctional high-avidity reagents to detect the CAR at the proteomic level (Section III). Using antigen multimers to sort CAR T cells from patient biospecimens for longitudinal, single-cell, multi-omics analysis, I next reported that CD28-costimulated CAR T cells undergo two distinct clonal expansion stages *in vivo*, each of which is dominated by unique phenotypes (Section IV). Finally, using findings from comparing the single-cell data from complete responders and non-responders, I leveraged the type I interferon/interferon response factor 7 pathway for increasing CAR T-cell efficacy *in vitro* (Section V). Collectively, these findings are expected to introduce a better CAR-detection reagent for CAR T-cell scientists, improve how we understand CAR T-cell expansion and persistence, and synergize CAR T-cell therapy with an existing pharmaceutical *in vitro*. Ultimately, I hope these efforts will translate into improved CAR T-cell therapy formulations and longer progression-free survival for patients with r/r DLBCL.

SECTION I: INTRODUCTION TO CAR T-CELL THERAPY FOR B-CELL LYMPHOMAS

Chimeric antigen receptor (CAR) T-cell therapy has improved therapeutic options for patients with diffuse large B-cell lymphoma (DLBCL), the most common aggressive non-Hodgkin's lymphoma in the United States.[1] Every year, ~18,000 Americans are newly diagnosed with DLBCL, which results in a 64% 5-year survival rate and presents with a tumor comprised of diffusely proliferating B cells at nodal or extranodal sites. Although up-front chemoimmunotherapy is often curative (50-60% of patients), patients with lymphomas that are refractory to up-front treatment or relapse after achieving remission (r/r DLBCL) often succumb to their cancer.[2,3] Effective treatment options were limited until the United States Food and Drug Administration approved autologous CD19-directed CAR T-cell therapies for r/r DLBCL in 2017.

Autologous CD19-directed CAR T-cell therapy involves virally transducing a patient's T cells *ex vivo* with an anti-CD19 CAR—an engineered receptor consisting of an extracellular anti-CD19 single-chain variable fragment (scFv), a hinge/transmembrane region, and intracellular costimulatory (CD28 or 4-1BB) and activation (CD3ζ) domains. Over the course of therapy, a patient's peripheral blood T cells are collected through apheresis, activated, retrovirally transduced with the CAR, expanded *ex vivo*, and infused back into the patient for cancer treatment. Upon scFv-dependent recognition of CD19 (antigen associated with normal and lymphoma B cells) on the surface of a lymphoma cell *in vivo*, CAR-transduced T cells (i.e., CAR T cells) activate, proliferate, differentiate, kill the target cell, and produce cytokines. Having elicited ~40% complete response rates, CAR T-cell therapy represents significantly improved survival for patients with r/r DLBCL.[4–7]

In this introduction to CD19-directed CAR T-cell therapy for r/r DLBCL, I will first present a concise history of CARs from their inception to the present day. Then, I will describe the state of and clinical/engineering frontiers associated with the current generation of CAR T-cell therapy formulations used to treat patients with r/r DLBCL. This introduction is not meant to be exhaustive.

The main goal is to contextualize the reader with the current state-of-the art, while providing the motivation and background to understand the following chapters.

I: Historical development of CD19-directed CAR T-cell therapy for r/r DLBCL

The earliest studies that spawned the development of CARs involved chimeric genes designed under Dr. Zelig Eshhar, a pioneer in T-cell engineering at the Weizmann Institute of Science. In these initial studies (published in 1989), the constant domains of TCRα and TCRβ were fused to the variable domains of an antibody fragment specific for the 2,4,6-trinitrophenyl (TNP) hapten. These chimeric constructs endowed T cells with MHC-independent recognition of TNP.[8] In a subsequent series of studies (published in 1993), the anti-TNP scFv was chimerically fused with the transmembrane region and intracellular domain of CD3γ or CD3ζ, activating subunits of the TCR-CD3 complex. Transduction of this chimeric construct into cytolytic hybridoma T cells endowed the ability to secrete IL-2 upon MHC-independent recognition of trinitrophenyl-decorated target cells.[9] These pioneering studies spawned interest in engineering effector lymphocytes, such as T cells or natural killer cells, to recognize tumor-associated antigens for cancer treatment. We now call these early constructs "1st-generation CARs". Despite effector functionality *in vitro*, 1st-generation CARs did not persist *in vivo*, which precluded clinical utility.

Poor persistence was eventually improved under critical studies spearheaded by the laboratory of Dr. Michel Sadelain at the Memorial Sloan-Kettering Cancer Center. The Sadelain group recognized that low expression of ligands for costimulatory receptors (i.e., B7 family ligands for CD28) on tumor cells hindered their immunogenicity by tumor-specific lymphocytes. Around this same time, it was increasingly recognized that T cells require signaling from both the TCR-CD3 complex (signal 1) and the CD28 costimulatory receptor (signal 2) for full T-cell activation. Signal 1 in the absence of signal 2 causes apoptosis through activation-induced cell death (AICD).[10,11] To ameliorate AICD, the Sadelain group (published in 1998) replaced the ligand recognition domain of CD28 with an scFv targeting GD2, a ganglioside overexpressed in many human cancers. Upon transduction into human T cells, this chimeric receptor produced signal 2 upon recognition of GD2 on target cells, thereby rescuing T cells from AICD and amplifying IL-2 secretion.[12] Subsequently in 2002, the Sadelain group published a study describing how they appended the CD3ζ intracellular domain to CD28 fused to an scFv targeting prostate-specific membrane antigen (PSMA). Upon transduction in human T cells, this chimeric receptor concomitantly provided signal 1 (via the CD3ζ domain) and signal 2 (via the CD28 domain) upon recognition of PSMA on target cells. Consequently, transduced T cells became activated, robustly proliferated, and secreted copious amounts of IL-2 in co-cultures with target cells.[13] We now call this construct a "CD28-costimulated 2nd-generation CAR". In 2007, the Sadelain group engineered a CD19-directed CD28-costimulated 2nd-generation CAR, and compared its antitumor efficacy with that of its first-generation counterpart in immunodeficient mice bearing CD19$^+$ tumor cells. These studies conclusively demonstrated that the CD28 domain increased T-cell persistence, augmented T-cell function, and prolonged survival of the host, leading to long-term survival in some cases.[14] With compelling preclinical data supporting its efficacy, the CD28-costimulated anti-CD19 CAR was quickly moved to clinical trials.

At the same time, a second CAR was being developed under a group of laboratories, including that of Dr. Carl June at the University of Pennsylvania. Simultaneously while the CD28-costimulated second-generation CAR was tested, it was increasingly recognized that TNFR family receptors, including 4-1BB, can also deliver signal 2.[15] In 2004, the laboratory of Dr. Campana at St. Jude Children's Hospital published a study detailing a chimeric receptor consisting of an anti-CD19 scFv, the CD8α transmembrane and hinge, and the 4-1BB and CD3ζ intracellular domains. Upon transduction into human lymphocytes, this chimeric construct enabled cytotoxicity, clonal expansion, and cytokine secretion against CD19$^+$ acute lymphoblastic leukemia cells.[16] We now call this construct a "4-1BB-costimulated 2nd-generation CAR". Then, in 2009, the June lab tested and compared the 4-1BB- and CD28-costimulated 2nd-generation CARs *in vivo* in xenograft leukemia models. These studies established that while both 2nd-generation CARs mediate greater *in vivo* efficacy than their 1st-generation counterparts, the 4-1BB costimulatory domain caused prolonged survival and greater efficacy than the CD28 costimulatory domain.[17] Later studies will dispute the latter claim.[18] With such remarkable preclinical data supporting its efficacy, the 4-1BB-costimulated anti-CD19 CAR was also moved to clinical trials.

At this point, the stage was set for the testing of both second-generation CARs in patients. In a landmark clinical study (NCT00924326) published in 2010, autologous T cells expressing the CD28-costimulated CAR were infused into a patient with follicular lymphoma that relapsed following chemoimmunotherapy. CAR T cells rapidly eradicated both the patient's lymphoma and B-cell precursors in the bone marrow, resulting in a complete response. B-cell aplasia and hypogammaglobulinemia continued at least 39 weeks after infusion, suggesting that functional CAR T cells persisted *in vivo*.[19] In a similarly remarkable clinical study (NCT01029366) published in 2011, autologous T cells expressing the 4-1BB-costimulated CAR were infused into three patients with chronic lymphocytic leukemia that was refractory to chemotherapy. CAR T cells expanded >1000-fold, trafficked to bone marrow, and rapidly lysed tumor cells, resulting in complete remission for two patients. CAR T cells were detectable for at least 6 months, mediating both B-cell aplasia and hypogammaglobulinemia.[20] It is noteworthy that this clinical study suggests CAR T-cell therapy is not a "silver bullet", since one of the three patients did not achieve a complete remission. Nonetheless, both clinical studies demonstrated that CD28- or 4-1BB-costimulated CAR T cells can graft and kill CD19$^+$ cancer cells *in vivo*.

Therefore, large-scale clinical studies were conducted to measure the efficacy and clinical utility of CAR T-cell therapy for patients with r/r DLBCL. In a multicenter study (ZUMA-1, NCT02348216), autologous CD28-costimulated CAR T-cell therapy (now called axicabtagene ciloleucel or "axicel") was administered to 101 patients, causing a 40% complete response rate 15 months after infusion.[4] Similarly, in a single-center study (JULIET, NCT02445248), autologous 4-1BB-costimulated CAR T-cell therapy (now called tisagenlecleucel or "tisacel") was administered to 93 patients, causing a 32% complete response rate 12 months after infusion.[5] In both studies, patients often exhibited adverse side effects shortly after infusion of CAR T cells, including cytokine release syndrome (CRS) and immune effector cell-associated neurotoxicity (ICANS). With CRS, patients experience fever, tachycardia, hypotension, among other signs of systemic inflammation. With ICANS, patients experience delirium, confusion, impaired consciousness, among other signs of neurotoxicity. Both CRS and ICANS occur presumably due to pro-inflammatory cytokines in serum or cerebrospinal fluid. Since patients in both trials had advanced disease and exhausted most other treatment options, CAR T-cell therapy undeniably improved treatment options and offered the possibility of remission. Hence in 2019, both formulations were approved by the US Food and Drug Administration for treating r/r DLBCL.

Subsequently, a third CAR T-cell therapy formulation (now called lisocabtagene maraleucel or “lisocel”) was also tested on patients with r/r DLBCL. The CAR construct used in lisocel consisted of the costimulatory domain from the CAR used in tisacel (4-1BB), but also the transmembrane domain from the CAR used in axicel (CD28). Moreover, CD4 and CD8 CAR T cells were infused at a fixed 1:1 ratio. In a multi-center study (TRANSCEND, NCT02631044), lisocel was administered to 269 patients, causing a 64% complete response rate 18 months after infusion. Notably, lisocel caused lower incidences of high-grade CRS or ICANS.[6,7] Hence in 2021, lisocel was approved by the US Food and Drug Administration for treating r/r DLBCL.

II: Current state and frontiers of CD19-directed CAR T-cell therapy for r/r DLBCL

As previously described, three formulations of autologous CD19-directed CAR T-cell therapy are FDA-approved for r/r DLBCL: axicel, tisacel, and lisocel. All formulations utilize CAR constructs (**Figure I-1**) featuring an anti-CD19 scFv (clone FMC63), but differ in the hinge, transmembrane, and costimulatory domains. Axicel utilizes the CD28 hinge, CD28 transmembrane, and CD28 costimulatory domains. Tisacel utilizes the CD8α hinge, CD8α transmembrane, and 4-1BB costimulatory domains. Lisocel utilizes the IgG4 hinge, CD28 transmembrane, and 4-1BB costimulatory domains. In axicel, the CAR is transduced γ-retrovirally, whereas in tisacel and lisocel, the CAR is transduced lentivirally. A final distinction is how the CAR T-cell infusion is prepared. With axicel and tisacel, all peripheral blood T cells are transduced, cultured, and infused, without controlling for the CD4:CD8 ratio. With lisocel, the peripheral blood CD4^{+} and CD8^{+} T cells are isolated, transduced, and cultured separately. Then, the CAR T cells are infused at a 1 to 1 CD4:CD8 ratio.

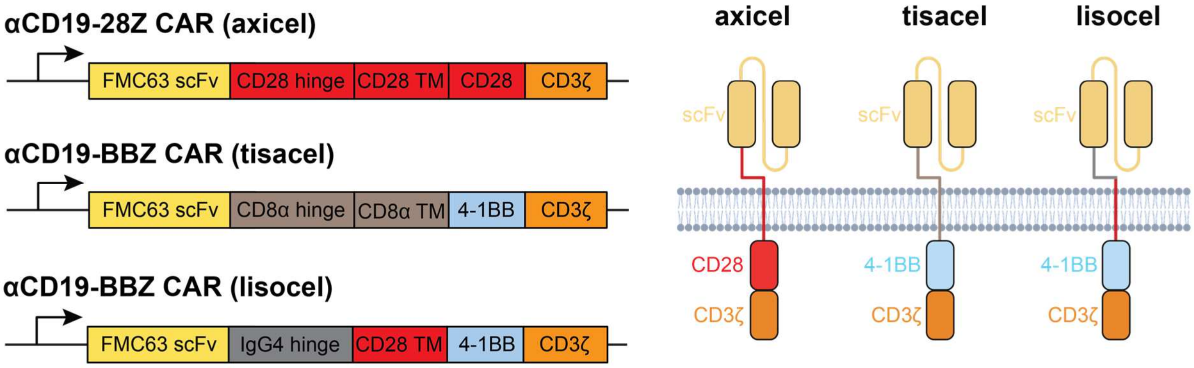

Figure I-1. Clinical CAR constructs used for treating r/r DLBCL. Diagrams detailing the construct (left) and protein (right) designs of the CARs used in axicel, tisacel, and lisocel. Colors used in the construct and protein diagrams are harmonized.

Clinical response rates do not differ between the three formulations. In a comprehensive meta-analysis of 33 studies involving 2172 CAR T-cell therapy patients, all three formulations achieved ~70% and ~54% objective and complete response rates, respectively. However, differences emerged in rates of high-grade side effects. Axicel, tisacel, and lisocel caused high-grade CRS in 9%, 21%, and 2% of patients, respectively. Furthermore, axicel, tisacel, and lisocel caused high-grade ICANS in 31%, 8%, and 10% of patients, respectively. Overall, axicel tends to cause ICANS while tisacel tends to cause CRS. Meanwhile, lisocel caused low incidences of both CRS and ICANS.[21] However, the data regarding lisocel completely originates from the trial used to establish efficacy for licensing. Lisocel is the newest formulation and lacks corresponding real-world data. Newer data may change these conclusions.

Physicians considering CAR T-cell therapy for treating patients with r/r DLBCL must choose between axicel, tisacel, and lisocel. Two important technical considerations are manufacturing turnaround time and frailty of the patient. In particular, axicel has the quickest manufacturing turnaround time and may be more appropriate for patients with aggressive disease. On the other hand, lisocel causes the lowest incidence of high-grade side effects and may be more appropriate for frailer or older patients who cannot tolerate toxicities. Other non-technical considerations include the hospital's access to the particular product, the clinical team's prior experience and expertise, and the different financial cost of each product.

Many current and exciting research frontiers exist for CAR T-cell therapy for r/r DLBCL, but most focus on two directions: addressing therapy non-response and broadening indications for CAR T-cell therapy. Since CAR T-cell therapy is a third-line therapy, non-responders do not have many treatment options and commonly succumb to their disease. Understanding therapy failure in non-responder patients may unveil avenues for improving response rates or useful biomarkers of clinical response. Clinical studies have demonstrated that therapy non-response correlates with molecular signatures of T-cell exhaustion in the infusion product.[22] Furthermore, non-responder CAR T cells from the infusion product exhibit less polyfunctional cytokine secretion upon target cell stimulation[23], which is a hallmark of T-cell exhaustion. In the T-cell immunoengineering field, T-cell exhaustion universally correlates with suboptimal tumor control.[24,25] In fact, preclinical studies have demonstrated that CAR T cells can get exhausted from a variety of sources, including the tumor microenvironment[26], tonic signaling[27], and TCR-mediated signaling[28]. Many strategies for ameliorating CAR T-cell exhaustion are being tested in preclinical studies, including synergizing CAR T-cell therapy with checkpoint blockade immunotherapy, enriching for stem-like CAR T cells, tuning elements of the CAR design, and application of cytokines or pharmaceuticals.[29,30]

The other frontier lies in broadening indications for CAR T-cell therapy. Current therapy formulations are FDA-approved only for patients with r/r DLBCL as a third-line therapy. Hence, response rates are likely limited by the advanced disease of the chosen patient population. Furthermore, autologous CAR T-cell therapy depends on the immune abilities of the patient's own

T cells, which may be compromised if the patient has undergone intense chemoimmunotherapy or autologous stem cell transplant. Many clinical trials have tested CD19-directed CAR T-cell therapy as second-line therapy, including ZUMA-7 (NCT03391466) for axicel[31], Belinda (NCT03570892) for tisacel[32], and Transform (NCT03575351) for lisocel[33]. Compared to the standard of care, both axicel and lisocel caused higher complete response rates, longer event-free survival, and longer progression-free survival. Disappointingly, tisacel did not improve upon the standard of care in these parameters, though this can be explained by longer manufacturing turnaround time and patients with more aggressive and/or advanced disease.[34] Moreover, newer clinical trials are beginning to test CD19-directed CAR T-cell therapy as first-line therapy. Recently, axicel was tested with high-risk large B-cell lymphoma as a first-line therapy in 40 patients in a multicenter trial (ZUMA-12, NCT03761056). High-risk large B-cell lymphoma has poorer outcomes under standard chemoimmunotherapy than other lymphoma subtypes. Complete response rate was 78% at 6 months following infusion.[35] These studies suggest a future when CAR T-cell therapy becomes a more ubiquitous and effective tool.

SECTION II: REVIEW OF EXISTING TOOLKIT FOR CAR DETECTION[1]

Chimeric antigen receptor (CAR) T-cell therapy is a promising frontier of immunoengineering and cancer immunotherapy. Methods that detect, quantify, track, and visualize the CAR, have catalyzed the rapid advancement of CAR T-cell therapy from preclinical models to clinical adoption. For instance, CAR-staining reagents have enabled flow cytometry analysis, imaging applications, cell sorting and high-dimensional clinical profiling. Molecular assays, such as quantitative polymerase chain reaction, integration site analysis, and RNA-sequencing, have characterized CAR transduction, expression, and *in vivo* CAR T-cell expansion kinetics. *In vitro* visualization methods, including confocal and total internal reflection fluorescence microscopy, have captured the molecular details underlying CAR immunological synapse formation, signaling, and cytotoxicity. *In vivo* tracking methods, including two-photon microscopy, bioluminescence imaging, and positron emission tomography scanning, have monitored CAR T-cell biodistribution across blood, tissue, and tumor. In this section, we review the plethora of CAR detection methods, which can operate at the genomic, transcriptomic, proteomic, and organismal levels. For each method, we discuss: (1) what it measures; (2) how it works; (3) its scientific and clinical importance; (4) relevant examples of its use; (5) specific protocols for CAR detection; and (6) its strengths and weaknesses. Finally, we consider current scientific and clinical needs in order to provide future perspectives for improved CAR detection. By facilitating experimental design and planning, this review aims to catalyze basic, immunoengineering, and clinical research.

---

[1] This chapter is based on a published paper:
Hu, Y., & Huang, J. (2020). The Chimeric Antigen Receptor Detection Toolkit. *Frontiers in Immunology*, *11*, 1–16. https://doi.org/10.3389/fimmu.2020.01770

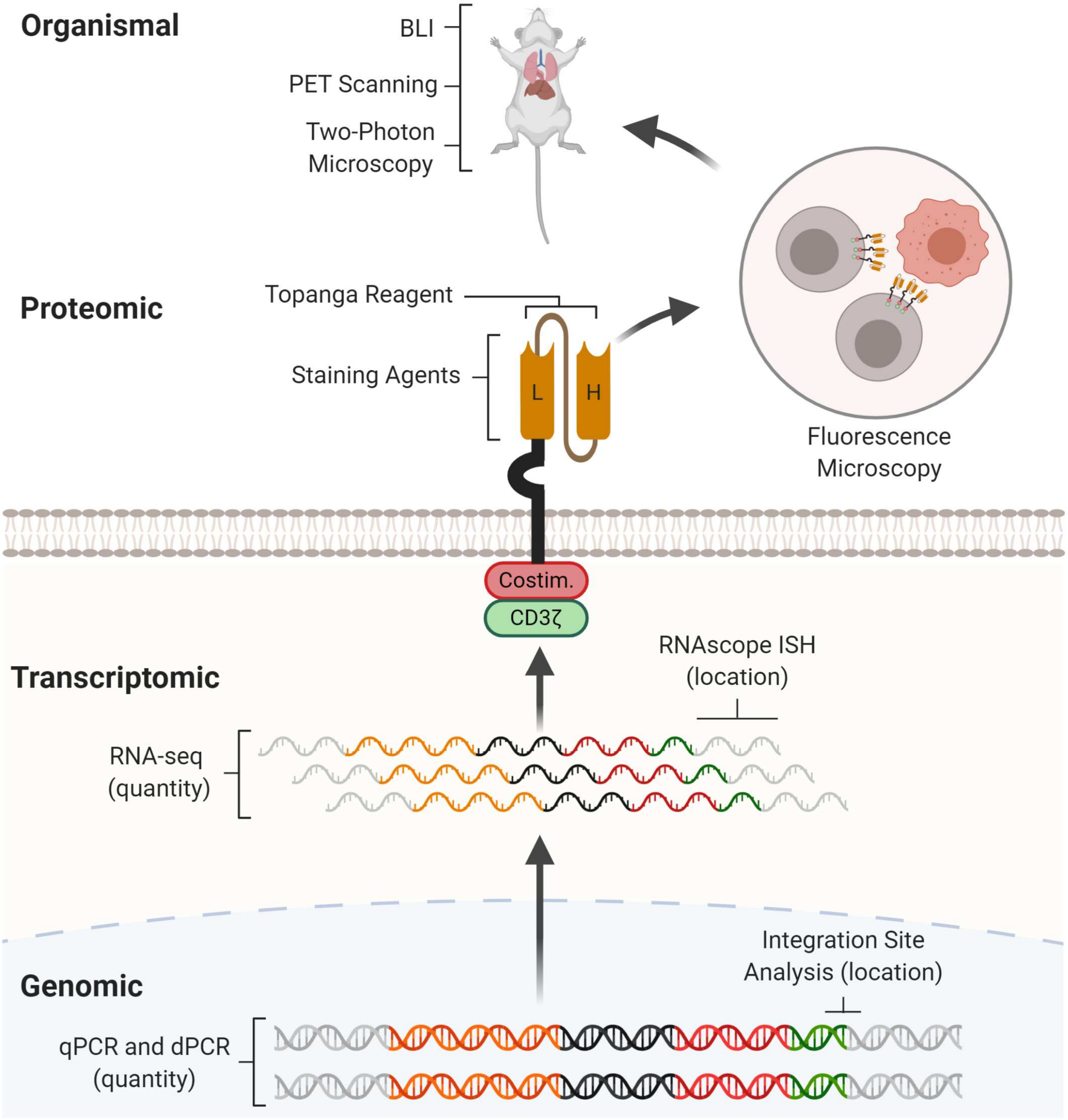

Figure II-1. CAR detection methods across multiple levels. CARs can be detected at the genomic, transcriptomic, proteomic, and organismal levels. At the genomic level, quantitative PCR (qPCR) and digital PCR (dPCR) measure CAR vector copy number while integration site analysis profiles sites of insertional mutagenesis of the CAR vector. At the transcriptomic level, RNA-seq and RNAscope *in situ* hybridization (RNAscope ISH) measure abundance and subcellular localization of CAR mRNA molecules respectively. At the proteomic level, staining reagents facilitate flow cytometry and western blotting for quantification of the CAR protein, while the Topanga reagent detects the CAR via luminescence. The CAR can also be fused with fluorescent proteins for fluorescence microscopy. At the organismal level, bioluminescence imaging (BLI) and positron emission tomography (PET) scanning determines the distribution of CAR T cells between organs, while two-photon microscopy tracks single CAR T cells in tissue.

I: Introduction

Accurate and reproducible CAR detection methods are required to address major engineering and clinical challenges in the CAR T-cell field. For instance, developing CAR T-cell therapy for solid tumors and elucidating clinical nonresponse/relapse mechanisms in B-cell cancers require methods to stain and sort CAR T cells from clinical samples for downstream applications, such as multiparameter flow cytometry and next-generation sequencing. Investigating *in vivo* CAR T-cell biology requires methods to track and assess *in vivo* CAR T-cell expansion kinetics, persistence, biodistribution, and effector functions in patients and animal models. Optimizing CAR molecular designs requires methods to characterize CAR signaling and visualize CAR immunological synapse formation at the molecular and cellular levels.

Here, we review current CAR detection methods. After describing the target and importance of each CAR detection method, we will discuss experimental protocols, examples of its application, as well as its strengths and weaknesses. Wherever possible, we will provide perspectives for method improvements. We will introduce CAR detection methods in the order of the level at which they operate: genomic, transcriptomic, proteomic, and organismal (**Figure II-1**). By facilitating experimental design and planning, this review aims to catalyze basic, immunoengineering, and clinical research.

II: CAR Detection at the Genomic Level

During the CAR manufacturing process, T cells are virally transduced with a CAR vector, which semi-randomly integrates into the T cell's genome. There are three main methods for detecting the integrated CAR vector: quantitative polymerase chain reaction (qPCR, **Figure II-2A**), digital polymerase chain reaction (dPCR, **Figure II-2B**), and integration site analysis (**Figure II-2C**). Using genomic DNA (gDNA) extracted from the cell analyte, qPCR and dPCR determine the frequency while integration site analysis determines the genomic locations of the integrated CAR vector. Since gDNA is more stable than mRNA, proteins, or cryopreserved cells, experiments involving qPCR, dPCR, and integration site analysis can be easier to coordinate. Importantly, these methods can help evaluate and optimize the safety profiles of alternative non-viral techniques for CAR vector delivery, including CRISPR/Cas9 and transposon-mediated insertion.[36,37]

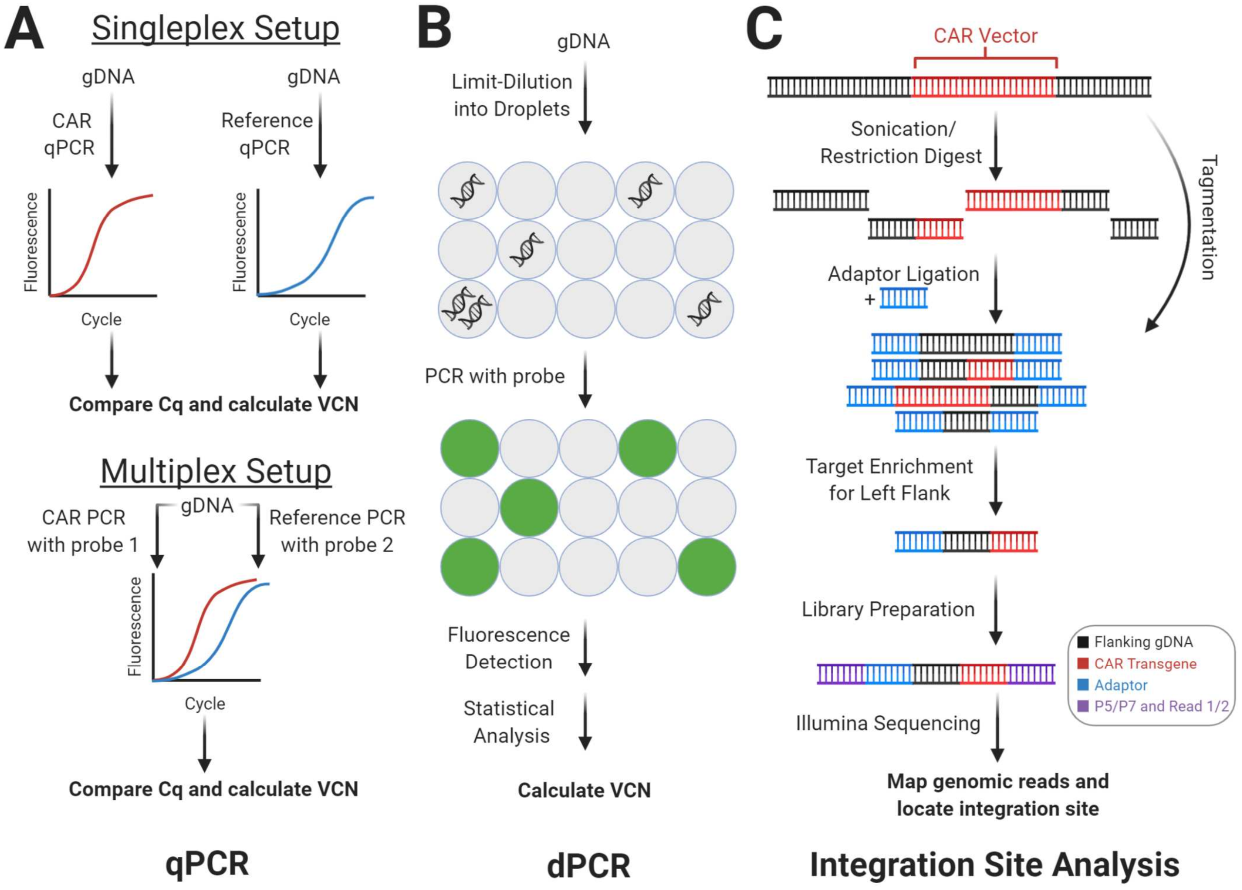

Figure II-2. Genomic CAR detection. Real-time quantitative PCR (qPCR) and digital PCR (dPCR) measure CAR vector copy number (VCN) while integration site analysis determines sites of insertional mutagenesis. (A) With qPCR, target amplicons are amplified from genomic DNA (gDNA) with fluorescent probes. C_q is calculated from fluorescence tracked over PCR cycles, which measures copy number. In the singleplex setup, vector and reference gene are amplified separately. In the multiplex setup vector and reference are amplified concurrently using two independent probes. (B) With dPCR, gDNA is partitioned into tiny droplets. Most droplets contain zero or one template copies. Target amplicons are amplified from each droplet separately, and the proportion of fluorescent droplets measures copy number. (C) With integration site analysis, gDNA is fragmented and ligated with adaptors in two steps with sonication or restriction enzymes, or in one step with tagmentation. Fragments containing either of the CAR vector flanks (left flank shown here) can be enriched and prepped for sequencing with multiple rounds of PCR. Mapping the reads to the genome determines sites of insertional mutagenesis.

Quantitative Polymerase Chain Reaction

qPCR measures the frequency of integrated CAR vector in the genome (**Figure II-2A**). Using target-specific primers and fluorescent probes, qPCR fluorescently quantifies an amplicon's accumulation over PCR cycles, resulting in a sigmoidal curve. The quantitation cycle (C_q), when fluorescence exceeds background levels, measures an amplicon's relative (compared to another amplicon) or absolute (compared to a standard curve) copy number. With CAR T-cell gDNA and CAR-specific primers and probes, qPCR can measure vector copy number (VCN)—the average vector copies per genome. VCN estimates CAR vector delivery efficiency and CAR T-cell representation in a cell pool. Hence, VCN is an important quality metric for clinical-grade CAR T-cell infusions and a technical benchmark that non-viral forms of CAR vector delivery, such as transposon-mediated delivery, must improve upon.[37] In both research and clinical settings, qPCR helps monitor VCN from patient blood gDNA over the course of treatment. These results have broadly shown strong correlations between CAR T-cell expansion, persistence, clinical response, and grade of side effects across multiple types of B cell cancers.[4,38,39]

Optimized CAR qPCR protocols have been developed to detect the anti-CD19 (clone FMC63) scFv. Wang et al. developed and validated TaqMan qPCR primers and probes for a ~130 bp amplicon from the FMC63 nucleotide sequence. In their assay, qPCR was performed side-by-side against FMC63 and *GAPDH t*o measure CAR copy number and genome copies respectively. These two measured values were used to calculate VCN. In addition to robustness across replicates, their qPCR assay achieved a minimum detection limit of 10 CAR copies per µL of blood and linear signal between 10^1-10^7 copies/µL.[40] However, a singleplex design increases sample and reagent use, decreases throughput, and introduces pipetting noise. Multiplexed qPCR can address these issues. Kunz et al. developed a single copy gene-based duplex qPCR assay (SCG-DP-PCR) to measure VCN. In their assay, the FMC63 scFv and *RPPH1* (RNaseP) were simultaneously PCR-amplified from the same gDNA sample using two independent fluorescent probes. Using *RPPH1* as an internal control, their duplex setup achieved similar efficiency as the corresponding singleplex setup. As proof-of-principle, they used SCG-DP-PCR to measure longitudinal VCN from three sets of CAR T-cell therapy patient blood gDNA samples.[41]

Overall, qPCR is a common and robust assay for monitoring CAR VCN. With well-designed primers and probes, qPCR is rapid, easily performed, and trustworthy for clinical use. qPCR can measure CAR vector delivery efficiency, on-treatment expansion kinetics, and persistence to predict clinical response.[4,38,39] As such, qPCR machines optimized and certified for CAR VCN measurements are now available commercially. However, qPCR has notable weaknesses. While robust at the population level, qPCR cannot differentiate subtle copy number differences. Hence, qPCR for VCN at the single-cell level is expected to be noisy and has never been implemented.[42] Other than VCN, qPCR cannot determine the CAR T cells' phenotype or whether the CAR is actually expressed. CAR expression depends on the chosen viral promoter, local chromatin architecture, regulatory elements (i.e., promoters, enhancers, insulator sequences), DNA methylation, and biological noise. Hence, qPCR overestimates the number of functional CAR T cells in a given population. Furthermore, the reliability of qPCR results depends on the target specificity of the primers and probes. In conclusion, qPCR is a clinically useful assay for monitoring VCN, but RNA-seq and flow cytometry may be more useful methods for determining CAR T-cell functionality in research settings.

Digital Polymerase Chain Reaction

Like qPCR, dPCR also measures VCN (**Figure II-2B**). However, dPCR measurements are more sensitive and precise. In brief, the gDNA template is partitioned into miniscule droplets, such that most droplets contain zero or one template molecule. PCR amplification of the target amplicon with a fluorescent probe occurs separately within each droplet. Subsequently, the droplets are flowed through an excitation source and detector, which measures each droplet's fluorescence. With Poisson statistics, the proportion of fluorescent droplets is used to calculate copy number.[43] While qPCR relies on continuous intermediate fluorescence measurements from PCR cycles, dPCR relies only on end-point fluorescence. Therefore, dPCR is robust to amplification kinetics and suppresses noise. Like with qPCR, dPCR can be multiplexed to decrease sample and reagent use, increase throughput, and decrease pipetting noise.

Fehse et al. developed a duplex dPCR assay to concomitantly probe the anti-CD19 CAR and a reference gene. Their duplex dPCR assay achieved a minimum detection limit of 0.01% CAR-transduced cells from 100 ng of gDNA. As proof-of-principle, they applied their assay on five sets of axicabtagene ciloleucel patient blood gDNA samples.[44] The enhanced sensitivity from dPCR also enables single-cell VCN measurements. Santeramo et al. developed dPCR to measure VCN in single lentivirally transduced T cells. In their assay, target amplicons were first pre-amplified to generate sufficient template material, prior to dPCR for vector and reference amplicons. Their single-cell assay generated results that were consistent with bulk measurements.[45] However, their method has yet to be applied for CAR VCN measurements.

As a more sensitive assay for monitoring VCN, dPCR shares strengths and weaknesses with qPCR. Unlike qPCR, the increased sensitivity allows dPCR to measure VCN in single cells. Single-cell VCN measurements can capture heterogeneity in transduction efficiency within a CAR T-cell infusion, which may impact clinical efficacy. However, compared to with qPCR, dPCR-compatible machines are rarer and dPCR reactions are more costly. Hence, widespread adoption of dPCR will require time.

Integration Site Analysis

The genomic locations of the integrated CAR vector can be profiled via integration site analysis (**Figure II-2C**). During CAR transduction, the CAR vector is randomly inserted into the genome (i.e. insertional mutagenesis), which can disrupt genes, trigger premalignant T cell proliferation, promote CAR T-cell efficacy, and influence clinical response.[46–48] Integration site analysis maps sites of insertional mutagenesis using next-generation sequencing. Importantly, integration site analysis can characterize the integration loci biases of different CAR vector delivery techniques.

In brief, integration site analysis involves fragmentation, PCR, and analysis steps. First, gDNA from the CAR T-cell sample is fragmented via restriction enzymes, transposases, or sonication. If necessary, adaptors are ligated onto the resulting DNA fragments. Then, fragments containing the CAR vector and flanking genome are enriched by PCR amplification, using a primer that anneals on the adaptor paired with a primer that anneals on the CAR vector. When this amplicon is sequenced, reads from the vector can extend into flanking human DNA, which can be aligned onto the human genome to reveal the integration loci.

Historically, integration site analysis employed restriction enzymes to fragment gDNA.[49] However, restriction enzymes generated inconsistent results that depended on which restriction enzyme was used.[50] The more up-to-date integration site pipeline for paired-end reads (INSPIIRED) eliminates restriction enzyme bias by using sonication for fragmentation. INSPIIRED includes well-documented steps for sonication, library preparation, Illumina paired-end sequencing, and bioinformatic site-calling.[51,52] INSPIIRED has been employed on anti-CD19 CAR T-cell therapy infusion samples, which showed that insertional mutagenesis near genes in cell-signaling and chromatin modification pathways predicted clinical response.[46] The final and more elegant method for integration site mapping uses transposases to combine the fragmentation and ligation steps (i.e. tagmentation). In one step, the transposase agnostically fragments gDNA and inserts an adaptor for PCR amplification and Illumina sequencing. The tagmented gDNA can simultaneously be used for integration site analysis and chromatin accessibility profiling (via ATAC-seq) via the recently developed vector integration analysis with epigenomic assay (EpiVIA), which can be applied at both the bulk and single-cell level.[53] In a clinical case study, Mu transposase-enabled integration site analysis characterized how lentiviral insertion of the CAR vector disrupted *TET2* and led to massive (94% of blood CD8$^+$ T cells) CAR T-cell expansion.[47,50] In addition, Tn5 transposase-enabled integration site analysis was employed to compare integration sites between γ-retrovirus, lentivirus, and *piggyBac* transposon-mediated gene transfer. Compared to viral transduction, the *piggyBac* transposon integrated less often near transcriptional start sites and more often into genomic safe harbors[37].

Overall, integration site analysis is a clinically relevant CAR detection method for locating sites of insertional mutagenesis. Newer integration site analysis pipelines involving transposases significantly streamline benchwork and enable EpiVIA, which combines integration site analysis and ATAC-seq at the bulk and single-cell levels.[53] Furthermore, the abundance of each CAR T-cell clone (each of which can be assumed to harbor unique integration sites) can be bioinformatically inferred from integration site sequencing data.[54] However, capture efficiencies for most CAR integration site analysis methods are unavailable. Where available, capture efficiencies are notably poor. For instance, at least three Mu transposase-enabled integration site analysis replicates were required to capture all six integration sites in a cell line.[50] Since polyclonal CAR T-cell populations contain far more than six integration sites, integration site analysis is unlikely to capture all integration sites, especially those from rare clones. With single-cell EpiVIA, only ~200 integration sites were detected from 700 M read pairs in ~5000 CAR-transduced T cells, which was notably far from saturation.[53] Hence, capture efficiencies should be better characterized, and protocol improvements are needed to assay rarer clones.

III: CAR Detection at the Transcriptomic Level

After genomic integration, the CAR vector is transcribed into mRNA. There are two main methods for detecting CAR mRNA: RNA-sequencing (**Figure II-3A**) and RNAscope *in situ* hybridization (**Figure II-3B**). These methods determine the abundance and subcellular location of the CAR mRNA respectively. Detection of CAR mRNA can be more functionally relevant than detection of the CAR vector, since CAR mRNA is closer to CAR protein, which exerts biological functions.

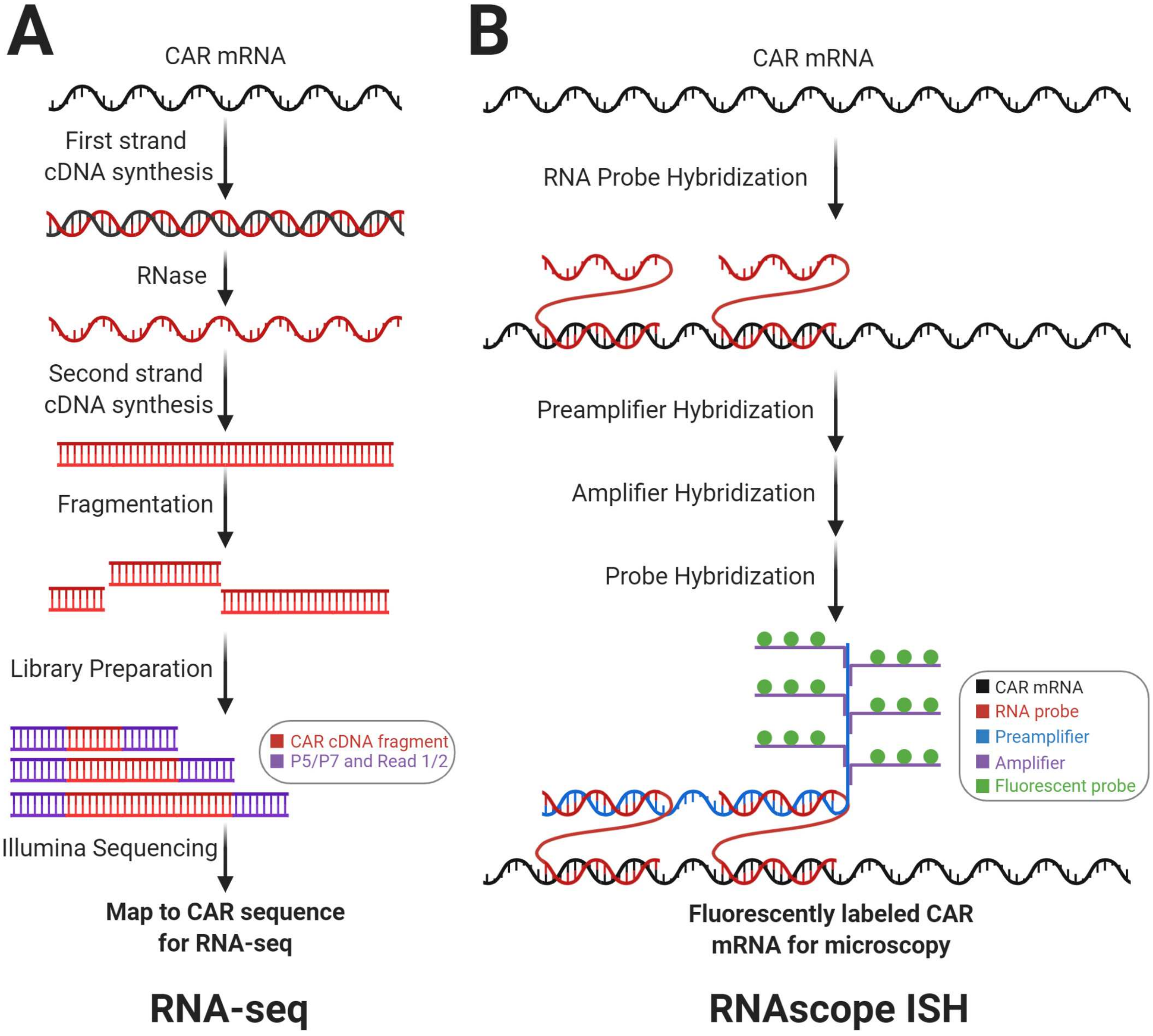

Figure II-3. Transcriptomic CAR Detection. RNA-sequencing (RNA-seq) and RNAscope *in situ* hybridization (RNAscope ISH) measure CAR mRNA abundance and subcellular localization respectively. (A) With RNA-seq, CAR mRNA is first converted to cDNA, which is then fragmented and prepped for sequencing. Counting the number of sequencing reads that map to the CAR transgene sequence measures CAR mRNA abundance. (B) With RNAscope ISH, the CAR mRNA is first hybridized with target-specific RNA probes. Subsequently, this complex is hybridized with the preamplifier, amplifier, and fluorescent probes to form a fluorescently labeled CAR mRNA complex for fluorescence microscopy.

RNA-sequencing

CAR mRNA abundance can be quantified by RNA-sequencing (RNA-seq, **Figure II-3A**). CAR mRNA quantity depends upon genomic factors: VCN, promoter strength, local chromatin architecture, regulatory elements, and DNA methylation. Importantly, CAR mRNA quantity drives antigen-independent tonic signaling[55] and amount of translated CARs on the cell surface influences antigen-sensitivity, NFAT signaling, and cytokine production.[56] In general, RNA-seq quantifies mRNA by converting mRNA to cDNA via reverse transcription. The cDNA can subsequently be fragmented, sequenced, and aligned to gene sequences to measure mRNA abundance. RNA-seq can correlate CAR mRNA abundance with transcriptional profiles. For instance, Zhang et al. utilized RNA-seq on anti-CD19 CAR T-cell therapy patient samples to measure correlation between CAR and *CD19* expression.[57] These analyses also apply at the single-cell level. Sheih et al. utilized single-cell RNA-seq to quantify CAR mRNAs and interrogate transcriptional profiles in $CD8^+$ T cells from CAR T-cell infusion products. CAR mRNA quantification helped to distinguish between CAR-transduced versus non-transduced cells in their single-cell dataset.[58] Prospectively, RNA-seq may also help characterize how viral promoters influence CAR transcription and *in vivo* differentiation. For example, with anti-CD19 CAR-T cell therapy, tisagenlecleucel employs the elongation factor 1-α promoter while axicabtagene ciloleucel employs the murine stem cell virus promoter. Although the EF-1α promoter drives higher and more consistent murine *in vivo* transcription than the MSCV promoter[59], no studies have determined whether this difference influences CAR T-cell functionality or clinical outcomes.

RNA-seq is now a routinely employed biological assay with many published protocols, commercial kits, and analysis pipelines. By integrating the genomic factors that influence CAR expression into a single readout, RNA-seq provides more clinically and biologically relevant data than qPCR for the CAR vector. Furthermore, in single-cell RNA-seq datasets, CAR mRNA quantification can help differentiate CAR T cells from non-CAR T cells during analysis.[58] However, mRNA-seq notably cannot capture factors that influence CAR translation, such as ribosome, initiation factors, and amino acid availability. Therefore, flow cytometry or western blotting for the CAR protein may be superior methods for determining CAR functionality in certain scenarios.

RNAscope* in situ *Hybridization

Both the quantity and subcellular localization of the CAR mRNA can be determined by RNAscope *in situ* hybridization (RNAscope ISH, **Figure II-3B**). RNAscope ISH utilizes RNA-specific oligonucleotide probes that anneal with a targeted RNA molecule in fixed and permeabilized cells, to generate fluorescence signals for microscopy. Dual target probes (for specificity) and additional adaptor probes (for signal amplification) enable detection, localization, and visualization at the single-molecule level. Using orthogonal sets of probes, RNAscope ISH can be multiplexed—CAR mRNA can be simultaneously detected along with other targets on the same slide.[60] Furthermore, RNAscope ISH can correlate CAR mRNA quantity with the CAR T cell's relative location within a tissue sample. For instance, RNAscope ISH (to detect the CAR mRNA's 3'-untranslated region) was employed to visualize anti-EGFRvIII CAR T-cell infiltration into glioblastoma after intravenous infusion. This study showed active trafficking of anti-EGFRvIII CAR T cells into tumor regions, which correlated with EGFRvIII downmodulation on tumor cells.[61] Furthermore, RNAscope ISH was employed to show anti-ROR1 and anti-BCMA CAR T-cell biodistribution and tissue trafficking in xenograft tumor models.[62]

RNAscope ISH is a specialized tool with many strengths: (1) spatial resolution spanning the single-molecule and subcellular levels; (2) capability for multiplex detection; (3) compatibility with microscopy. However, RNAscope ISH requires fixed and permeabilized cells, hence it cannot be used for live-cell RNA imaging. Studies have yet to take advantage of this method's unique strengths. For example, current studies use RNAscope ISH to distinguish CAR T cells from non-CAR T cells in tissue sections, with only limited use of its multiplexing capabilities. Furthermore, no studies have yet analyzed how CAR mRNA subcellular localization (e.g., near cell membrane) may influence CAR mRNA stability, degradation, or translation.

IV: CAR Detection at the Proteomic Level

After translation from CAR mRNA, the CAR protein drives antigen-dependent signaling. Unlike detection at the genomic or transcriptomic levels, detection at the proteomic level can directly evaluate CAR functionality. The CAR protein can be detected by flow cytometry (with staining reagents), luminescence (with Topanga reagent), immunoprecipitation (with staining reagents), and microscopy (with fluorescent protein fusions). **Figure II-4A** depicts where each detection reagent acts.

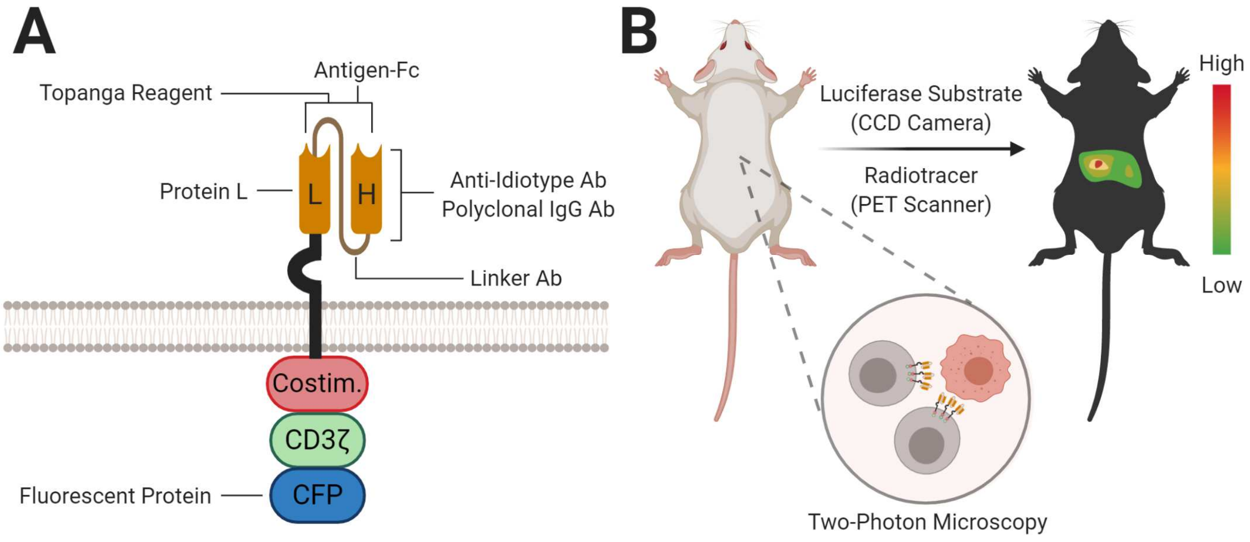

Figure II-4. Proteomic and Organismal CAR Detection. (A) At the proteomic level, the CAR protein can be detected with staining agents (for flow cytometry and immunoprecipitation), Topanga reagent (for luminescence), or fused fluorescent proteins (for microscopy and flow cytometry; cyan fluorescent protein (CFP) is shown as an example). The approximate location or binding site for each method is depicted on the cartoon. (B) At the organismal level, the biodistribution of CAR T cells between organ compartments can be measured by bioluminescence imaging (BLI) or positron emission tomography (PET) scanning using a luciferase substrate or radiotracer respective. Furthermore, single CAR T cells can be tracked in tissue with two-photon microscopy.

Staining Reagents for Flow Cytometry

Table II-1. CAR-Staining Reagents

Property	Anti-IgG Antibodies	Protein L	Antigen -Fc	Anti-Idiotype Antibody	Anti-Linker Antibody
One-step staining	Yes	No	No	Yes	Yes
Compatibility w/antibody panels	Inconsistent	No	Yes	Yes	Yes
Compatibility w/FcX reagents	Inconsistent	No	Some	Yes	Yes
Reagent stability	High	High	Often low	High	High
Specificity for CAR	Low	Low	High	High	High
Access to academic labs	Easy	Easy	Easy	Hard	Hard

The presence and quantity of the CAR protein on the cell surface can be assayed via fluorescent CAR-staining reagents and flow cytometry. In addition to CAR protein quantitation, these staining reagents also enable multicolor flow cytometry-based profiling and fluorescence-activated cell sorting. CAR-staining reagents were instrumental in illuminating factors that impact CAR T-cell clinical efficacy, including T-cell subset composition, CAR downmodulation after antigen engagement[56,63], and CAR T-cell trogocytosis[64]. Although many CAR-staining reagents exist, a comparison of sensitivity and specificity metrics between these staining agents has yet to be performed. Each staining reagent's target site and general properties are summarized in **Figure II-4A** and **Table II-1** respectively.

Two CAR-staining reagents target IgG-like fragments: polyclonal anti-IgG antibodies and Protein L. Polyclonal anti-IgG (often of goat origin) are commonly used as secondary antibodies to stain IgG-like fragments. As polyclonal reagents, they have significant batch-to-batch variation. Although they are provided by a variety of vendors, the polyclonal goat anti-mouse $F(ab)_2$ from Jackson ImmunoResearch Laboratories is the most widely used, and was historically used to characterize the anti-CD19 CAR in axicabtagene ciloleucel.[65] Protein L is a *Peptostreptococcus magnus* bacterial surface protein that binds to many immunoglobulin kappa (κ) light chains, including human $V_{K}I$, $V_{K}III$, $V_{K}IV$ and murine $V_{K}I$, without interfering with the immunoglobulin's antigen-binding site. In addition to whole antibodies, Protein L can also bind light chains on scFv.[66] Zheng et al. optimized Protein L as a CAR-staining reagent for flow cytometric detection, and demonstrated successful staining with a variety of CARs, including CARs containing human scFv (anti-EGFRvIII, anti-VEGFR2), murine scFv (anti-CD19, anti-CSPG4), and humanized scFv (anti-HER2, anti-PSCA). However, their method requires multiple cell washes before Protein L staining since carry-over immunoglobulin in serum or culture media must be strictly removed. Furthermore, their own results suggest their method may have worse stain index compared to polyclonal anti-IgG antibodies.[67] Protein L has been used to characterize masked CARs with tumor-specific activation[68], CAR downmodulation[56], tonic signaling[27], and to activate CAR T cells via Protein L that is bound on plates[56].

Although both polyclonal anti-IgG antibodies and Protein L are relatively cheap and accessible CAR-staining reagents, they share significant shortcomings: (1) cross-reactivity with non-CAR IgG-like proteins on the cell surface, requiring stringent washing before and after staining; (2) incompatibility with other antibodies in antibody panels and many FcX blocking reagents during multicolor flow cytometry, requiring multiple staining and washing steps; (3) cannot independently stain different CARs on a dual-CAR expressing T cell; and (4) cannot stain CARs with synthetic scFv. While the former two shortcomings are inconvenient, the latter two shortcomings significantly limit their applications in newer CAR systems.

Antigen-Fc is a CAR-staining reagent that utilizes the CAR’s binding affinity for its target antigen. Antigen-Fc are chimeric proteins with an N-terminal target antigen fused to a C-terminal Fc fragment (often from human IgG1). Due to the Fc fragment, antigen-Fc dimerizes under non-reducing conditions in solution and can be purified via Protein A beads. To stain CAR-T cells, antigen-Fc is applied, followed by a secondary staining step with fluorophore-labeled anti-Fc or anti-biotin/streptavidin (if the antigen-Fc was biotinylated). Alternatively, the antigen-Fc is directly conjugated with a fluorescent dye, which eliminates the secondary staining step. Biochemically, antigen-Fc binds with antibody-like specificity and affinity. Antigen-Fc has been used to evaluate novel CAR constructs[69], to independently measure expression of each CAR in dual CAR-T cells[70], and to activate CAR T cells via antigen-Fc that is bound on plates[69]. Antigen-Fc, including CD19-Fc, HER2-Fc, and PSCA-Fc, are commercially available from many vendors.

CD19-Fc is of special interest, due to the success of anti-CD19 CAR T-cell therapy and availability of patient samples for research. De Oliveira et al. expressed CD19-Fc for CAR T-cell staining and found that exon 4 of the CD19 ectodomain (CD19ecto) is required for binding to the anti-CD19 (clone FMC63) CAR used in Yescarta and Kymriah. However, their staining results show inferior stain index than either polyclonal anti-IgG antibodies or Protein L, hinting at issues with protein quality.[71] Indeed, CD19ecto aggregates in higher-order disulfide-bonded oligomers and is notorious for being a difficult-to-express protein.[72] The crystal structure of CD19ecto bound to a B43-Fab shows that CD19ecto can form a unique elongated β-sandwich, which may be difficult to fold properly within overexpression systems.[73] In response to technical challenges with CD19ecto production, Lobner et al. expressed a novel chimera consisting of an N-terminal CD19ecto with a C-terminal human serum albumin domain 2 (AD2). Compared to CD19ecto, the CD19-AD2 chimera is easier to produce, monomeric, and effectively binds and stains the FMC63-based anti-CD19 CAR.[74]

In conclusion, although antigen-Fc are more CAR-specific than polyclonal anti-IgG antibodies and Protein L, antigen-Fc also have notable limitations: (1) more expensive; (2) possible decreased stability in solution compared to traditional antibodies; (3) may be incompatible with FcX blocking reagents; and (4) the Fc fragment may non-specifically bind Fc receptors. Future iterations of antigen-Fc may involve engineered Fc regions that enable compatibility with FcX blocking reagents and disable non-specific binding of Fc receptors. Furthermore, future iterations of antigen-Fc may also take advantage of higher valency binding. Antigen-Fc are analogous to MHC-multimers, which stain antigen-specific T cells by binding to the TCR with high avidity.[75,76] Research on MHC-multimers have shown that higher valency staining reagents improve sensitivity via higher avidity binding. For example, MHC-dodecamers

(12-valency) and MHC-dextramers (>>4-valency) are more sensitive than MHC-tetramers (4-valency).[77,78] CAR-staining reagents with higher binding valency than antigen-Fc (2-valency) should be constructed, and the potential sensitivity enhancement from higher avidity binding should be determined. Higher sensitivity antigen-Fc variants may facilitate staining and analysis of CAR T cells with low CAR expression due to genome position effects on the CAR vector or CAR downmodulation. These studies will be summarized in Chapter III of this dissertation.

Another CAR-staining reagent is anti-idiotype antibodies. Anti-idiotype antibodies specifically bind the variable regions of a particular scFv. Furthermore, anti-idiotype antibodies enable immunohistochemical staining and can potentially block CAR ligation in an *in vivo* setting. Jena et al. developed and characterized a novel monoclonal anti-idiotype antibody (clone 136.20.1) against the FMC63-based anti-CD19 scFv from immunized mice. Their results show 136.20.1 has a lower detection limit of 0.1%, is compatible with microscopy and immunohistochemistry, and inhibits the effector functions of anti-CD19 CAR T cells.[79] This antibody has since been used to characterize CAR T cells in preclinical studies [47,55] and clinical trials.[80] Interestingly, 136.20.1 was also used to create a novel anti-idiotype CAR as a cellular antidote and kill switch during therapy.[81] Other anti-idiotype antibodies include clone 1A7, which can detect the anti-GD2 (14g2a) CAR.[82] Notable advantages of anti-idiotype antibodies include high reagent stability, low background staining, compatibility with antibody panels in multicolor flow cytometry, and the ability to discriminate between different types of CARs. However, anti-idiotype antibodies are expensive in cost and time, and most are commercially unavailable. Development of an anti-idiotype antibodies for every new CAR is infeasible.

Finally, Kite Pharma developed rabbit monoclonal antibodies against two commonly used linkers in the CAR scFv: clone KIP-1 against the Whitlow linker and clone KIP-4 against the G_4S linker. These linkers connect the heavy and light chains in the scFv. KIP-1 can detect (via flow cytometry) and activate CAR-T cells with the Whitlow linker.[83] KIP-1 was subsequently used in

Kite Pharma and Gilead-sponsored studies.[84] However, these linker antibodies are unlikely to be accessible to most academic labs without industry sponsorship.

Biochemical Assays

The CAR's presence and binding competence can be assayed by luminescence (in the absence of a flow cytometer) using the Topanga reagent. Gopalakrishnan et al. developed the Topanga reagent, a chimeric protein consisting of the N-terminal CAR-antigen fused to a C-terminal marine luciferase, NLuc. Incubation of the Topanga reagent with CAR T-cell mixtures facilitated luminescent detection. The Topanga reagent's exceptional sensitivity allows it to detect CAR-binding in a mixture of 0.001% CAR-T cells out of 1 million PBMCs.[85] Although the Topanga reagent cannot determine percentage of CAR-expressing cells, it might be useful for quick quality control during manufacturing and testing the binding functionality of the CAR.

CAR signaling can be assayed by immunoprecipitation (IP) or co-immunoprecipitation (co-IP) using Protein L-conjugated beads for analysis of CAR post-translational modifications and interaction partners.[67] Protein L-conjugated beads bind to the light chain of the CAR scFv, and can pull down CAR interaction partners for western blotting or mass spectrometry. Ramello et al. utilized this approach to pull down CAR immune complexes. Complexes were analyzed by tandem liquid chromatography-mass spectrometry, to identify 253 CAR interaction partners enriched within 15 canonical pathways.[86] In addition to Protein L beads, CAR IP can be performed on epitope-tagged CAR receptors. Salter et al. used the 9-amino acid Strep-tag II to tag the CAR between the scFv and the hinge, demonstrating that endogenous Lck and CD28 differentially associate with CD28-based and 4-1BB-based CARs in the absence of signaling.[87] IP with epitope tags is more target-specific than IP with Protein L since Protein L is known to interact with IgG-like molecules. However, these epitope tags must not interfere with CAR function. Furthermore, current FDA-approved anti-CD19 CAR designs do not have a convenient epitope tag for IP.

Microscopy

CAR trafficking and immunological synapse (IS) formation can be visualized by microscopy. Importantly, confocal and total internal reflection fluorescence (TIRF) microscopy can probe CAR signaling and inform CAR engineering. Confocal microscopy visualizes the CAR with high spatial resolution. Effector and target cells can be adhered to glass slides, allowed to interact, and fixed prior to imaging. Using this approach, Davenport et al. found that CAR T cells form non-classical IS with multifocal Lck microclusters that may facilitate serial killing.[88] In addition, Long et al. utilized confocal microscopy with Cerulean-tagged CAR to show aggregation of the anti-GD2 CAR on the cell surface, which may contribute to antigen-independent tonic signaling.[27] However, this setup limits spatial resolution because the CAR IS lies on a vertical imaging plane formed through horizontal cell-cell interactions.[89] Xiong et al. circumvented this limitation using confocal microscopy with a vertical cell-pairing system, which flips the CAR IS onto a horizontal imaging plane. Their setup revealed that characteristics of the IS, including antigen clustering, lytic granule polarization, and distribution of key signaling molecules, predict CAR T-cell efficacy *in vivo*.[90]

In live cells, the CAR can be visualized at the molecular level via lipid bilayer experiments in conjunction with TIRF microscopy. TIRF microscopy excites fluorophores by inducing an evanescent field near the interface between two media with different refractive indices. In this setup, the CAR T cell interacts with antigen on glass-supported lipid bilayers to form an IS on the horizontal plane. The evanescent field selectively excites fluorophores near this plane. CAR proteins at this interface can be directly or indirectly detected, via fluorescently labeled CAR or CAR antigen.[91] Using TIRF, Xiaolei et al. characterized recruitment of CAR microclusters to the CAR IS, and found that the CAR IS disassembles quicker than the classical TCR IS.[92]

With either TIRF or confocal microscopy, fluorescently labeling the CAR for direct detection is preferred over labeling the CAR antigen. Labeling the CAR allows CAR tracking outside of the IS and in resting CAR T cells. One common method is to chimerically tag fluorescent proteins, such as green fluorescence protein derivatives, to the CAR C-terminus. In addition to enabling direct CAR visualization, this method also facilitates CAR quantification via flow cytometry. Walker et al. utilized cyan fluorescence protein-labeled CAR to measure anti-CD19 CAR downmodulation after antigen engagement. However, this tagging was not possible with all CAR constructs. They reported that an anti-ALK CAR tagged with cyan fluorescence protein failed to express [56]. Similarly, Morrissey et al. engineered enhanced green fluorescence protein-labeled CARs for phagocytosis that direct macrophages to engulf target cells. Trafficking of these CARs was studied via live-cell imaging.[93] For CARs that are not amenable to fluorescent protein fusion, an alternative method is staining the extracellular regions of the CAR with fluorescent Fabs or scFvs immediately before microscopy. These Fabs should neither block the CAR antigen binding site nor influence CAR trafficking or mechanotransduction. Sasmal et al. utilized this method to label the TCR with an anti-TCRβ scFv for FRET studies.[94] However, this method has yet to be applied onto CARs.

Finally, CARs have yet to be visualized with super-resolution microscopy or lattice light-sheet microscopy (LLSM). These emerging technologies can significantly improve spatial and temporal resolution. Rosenberg et al. utilized LLSM to visualize TCR dynamics, which were correlated with T-cell signaling states.[95,96] However, similar experiments to characterize CAR dynamics have not yet been performed. Nerreter et al. utilized stochastic optical reconstruction microscopy (a form of super-resolution microscopy) to image CD19 expression on multiple myeloma patient cancer cells to establish a sensitivity threshold for CAR T-cell efficacy.[97] However, similar studies to visualize the CAR itself have not been conducted.

V: CAR Detection at the Organismal Level

After CAR T cells are manufactured and intravenously infused, CAR T cells proliferate and traffic between blood, lymph nodes, bone marrow, peripheral tissue, and tumor. *In vivo* detection and tracking of CAR T cells can probe location-dependent phenotypes and elucidate models for therapy failure. There are three main methods for tracking CAR T cells at the organismal level:

Table II-2. Representative BLI and PET Scanning Applications

Method Type	Reporter	Probe	Validation System	Notes
BLI	Firefly luciferase (FLuc)	D-luciferin	Anti-PSCA CAR-T cells in xenograft mouse model	-
BLI	Firefly luciferase (FLuc)	D-luciferin	anti-HLA-A*02:01 CAR-Tregs in human allograft mouse model	-
Duplex BLI	Renilla luciferase (RLuc) Click beetle luciferase (CBRLuc)	Coelenterazine and D-luciferin	anti-PSMA CAR-T cells in xenograft mouse model	Signal diminished by poor substrate availability
Duplex BLI	FLuc mutants	Infraluciferin	anti-CD19 CAR-T cells in xenograft mouse model	Used spectral unmixing
PET Scanning	Herpes simplex virus type 1 thymidine kinase (HSV1-TK)	^{18}F-FHBG	IL-13 zetakine CAR-T cells in clinical trial	Clinical study
PET Scanning	DOTA antibody reporter 1 (DAbR1)	^{86}Y-AABD for imaging ^{177}Lu-AABD for suicide	anti-CD19 CAR-T cells in xenograft mouse model	Forms covalent bond between reporter and probe
PET Scanning	*E. coli* dihydrofolate reductase (eDHFR)	^{18}F-labeled trimethoprim (^{18}F-TMP)	anti-GD2 CAR-T cells in xenograft mouse model	Sensitivity of ~11,000 CD8^{+} CAR-T cells per mm^{3}
PET Scanning	Human somatostatin receptor 2 (SSTR2)	^{18}F-NOTA-Octreotide (NOTAOCT)	ICAM-1-directed CAR-T cells in xenograft mouse model	Background expression of SSTR2 in healthy human tissue
PET Scanning	Human sodium iodide symporter (hNIS)	^{99m}TcO$_4^-$	anti-PSMA CAR-T cells in xenograft mouse model	Cheap and widely used radiotracer
PET Scanning	Prostate-specific membrane antigen	^{18}F-DCFPyL	anti-CD19 CAR-T cells in xenograft mouse model	Reporter/probe used extensively in tracking prostate cancer
PET Scanning	None	^{89}Zr-*p*-isothiocyanatobenzyl-desferrioxamine (^{89}Zr-DFO)	anti-CD19 CAR-T cells in xenograft mouse model	Physical labeling bypasses need for reporter; long half-life

bioluminescence imaging (BLI), positron emission tomography (PET) scanning, and two-photon microscopy (**Figure II-4B**). All three methods can monitor CAR T cells in organs. BLI and PET scanning utilize reporters and probes for visualization. A representative, but not exhaustive, list of applications of BLI and PET scanning is provided in **Table II-2**. Two-photon microscopy utilizes fluorescence for visualization with single-cell resolution. Unlike CAR detection in the previous levels, CAR detection at the organismal level most directly studies CAR T cells *in vivo*.

Bioluminescence Imaging

In vivo bioluminescence imaging (BLI) captures CAR T-cell biodistribution throughout an organism. BLI can probe for trafficking into solid tumors without needing to isolate the tumor for manual processing. To enable BLI, CAR T cells must be co-transduced with luciferase. During imaging, luciferase substrate is injected, circulate and diffuse to CAR T cells, and get processed by luciferase to emit light. The emitted light is captured using charge-coupled device (CCD) cameras, which convert light into electronic currents that localizes the light source. Conventional luciferases come from terrestrial (i.e., North American firefly luciferase, FLuc) or marine (i.e., Renilla luciferase, RLuc) animals, which use D-luciferin or coelenterazine respectively, along with O_2 and sometimes ATP. Newer luciferases are smaller and more sensitive.[98]

BLI can track *in vivo* CAR T-cell expansion. Chavez et al. utilized BLI to compare expansion kinetics of anti-CD19 CAR T cells cultured with different sera during *ex vivo* transduction. BLI showed that human platelet lysate led to memory-like CAR T cells, which exhibited superior *in vivo* expansion upon tumor re-challenge.[99] Furthermore, BLI can track *in vivo* CAR T-cell trafficking. Dawson et al. utilized BLI to show trafficking of anti-HLA-A*02:01 CAR-Tregs, which migrated into transplanted human allograft skin tissue and associated draining lymph nodes. These migratory behaviors correlated with CAR-Tregs preventing allograft rejection in NSG mice.[100]

Importantly, luciferase/substrate pairs can be multiplexed. For example, FLuc and RLuc can tag different cell populations in the same animal for imaging using different substrates. Serganova et al. used multiplex BLI to simultaneously track anti-PSMA CAR-T and PSMA$^+$ tumor cells with RLuc and click beetle luciferase respectively in a mouse model. Multiplex BLI revealed initial CAR T-cell sequestration in the lungs.[101] However, this method requires sequential injection of luciferase substrates. The signal from the first injection must entirely disappear before the second injection, which requires careful optimization. Hence, Stowe et al. developed a different approach to BLI multiplexing: spectral unmixing. In their system, two cell populations are tagged with two distinct luciferases that share a common substrate: infraluciferin. These distinct luciferases generate light with dissimilar emission wavelengths. After infraluciferin injection, total BLI signal is captured, which is spectrally unmixed into two bioluminescence channels. Their method captured anti-CD19 CAR-T cells homing to and expanding within the lymphoma tumor in a mouse model.[102] Spectral unmixing eliminates the requirement for sequential substrate injection.

Strengths of BLI include accessibility of CCD cameras among core facilities, standardized and high-throughput protocols, affordability, and multiplexed live-cell imaging. Furthermore, engineered FLuc derivatives, such as AkaLumine-HCl can emit near-infrared light, for superior deep-tissue penetration.[103] Hence, BLI is the method of choice for preclinical CAR T-cell experiments. However, it comes with notable weaknesses. BLI is not used in clinical trials because humans are too large for the emitted light to penetrate tissue efficiently. Furthermore, the luciferase reporter may be immunogenic. In mice, unlike intravital two-photon microscopy, BLI cannot track CAR T cells at the single-cell level. Finally, the location and metabolism of the CAR-T cells may decrease ATP and O_2 availability, leading to diminished BLI signal. Substrate availability is even more limited in the tumor microenvironment.[101] Development of engineered luciferases with superior enzymatic activity and tissue penetration only partially addresses these issues.

Positron Emission Tomography

Positron emission tomography (PET) scanning also captures CAR-T cell biodistribution throughout an organism. To enable PET, the CAR is co-transduced with a PET reporter, which can capture and accumulate a positron-emitting small molecule probe. For imaging, a probe is intravenously injected, which preferentially accumulates in CAR T cells due to the co-expressed PET reporter. Emitted positrons colocalize with CAR T cells, lose kinetic energy, combine with a nearby electron, gets annihilated, and emits high-energy photons. The high energy photons are captured with a PET scanner.[104]

Although many PET reporter/probe pairs have been developed to track CAR T cells, only one pair has been tried on patients in a CAR T-cell clinical study (NCT00730613 and NCT01082926): herpes simplex virus type 1 thymidine kinase (HSV1-TK) paired with 9-[4-[^{18}F]fluoro-3-(hydroxymethyl)butyl]guanine (^{18}F-FHBG). HSV1-TK is a cytosolic viral kinase that selectively phosphorylates nucleoside analogs such as ^{18}F-FHBG. Phosphorylated ^{18}F-FHBG then accumulates intracellularly. The pharmacology and safety profile of ^{18}F-FHBG in humans are well-documented, and ^{18}F-FHBG is FDA-approved as an investigational new drug. In this clinical study, Keu et al. co-expressed HSV1-TK with an interleukin-13 (IL-13) zetakine CAR in CD8$^+$ T cells to treat recurrent high-grade glioma in seven patients. The glioma disrupts the blood-brain barrier, allowing ^{18}F-FHBG to diffuse into the tumor. PET scans show increased signal around the tumor after CAR T-cell infusion, which suggests active trafficking of CAR T cells into the tumor. However, increased PET signal can also feasibly be due to increased nonspecific vascular leakage or glioma progression, which this pilot study cannot address.[105] Importantly, the HSV1-TK reporter may also function as a suicide switch by accumulating ganciclovir, a separate nucleoside analog which can induce apoptosis.[106] This can be a critical safety mechanism for patients experiencing adverse CAR T-cell-related side effects, including cytokine release syndrome and pneumonia. The kinetics and utility of HSV1-TK as a suicide switch for CAR T cells have yet to be clinically tested.

Other PET reporter/probe pairs have been developed in preclinical mouse models and are summarized in **Table II-2**. Krebs et al. used DOTA antibody reporter 1 (DAbR1), which binds irreversibly on the cell surface with ^{86}Y-labeled (*S*)-2-(4-acrylamidobenzyl)-DOTA (^{86}Y-AABD). DAbR1 does not inhibit *in vitro* cytotoxicity, and PET scans show homing of CAR T cells to the tumor. Furthermore, they predicted DAbR1 can be a suicide switch with ^{177}Lu-AABD, a heavier and more radioactive nuclide.[107] Sellmyer et al. used *Escherichia coli* dihydrofolate reductase enzyme (eDHFR), which binds to ^{18}F-labeled trimethoprim (^{18}F-TMP), to image anti-GD2 CAR T cells in mouse xenograft models. PET scans show colocalization between anti-GD2 CAR T cells and GD2^{+} tumor, which was confirmed with bioluminescence. Finally, they calculated that their method can detect ~11,000 CD8^{+} CAR T cells per mm^{3}.[108] Park et al. used human somatostatin receptor 2 (SSTR2), which ensures intracellular accumulation of ^{18}F-NOTA-Octreotide (NOTAOCT), to track CAR T cells of differing affinities to ICAM-1. PET scans captured CAR T-cell expansion and contraction kinetics.[109] However, background expression of SSTR2 may preclude its use in clinical trials.[110] Emami-Shahri et al. used human sodium iodide symporter (hNIS), which is compatible with $^{99m}TcO_4^-$, a cheap and widely used clinical radiotracer. Their results show trafficking of anti-PSMA CAR T cells into the tumor, which was confirmed by IHC.[111] Finally, Minn et al. co-transduced CAR T cells with PSMA, which interacts with ^{18}F-DCFPyL. Their results show divergence between CAR T-cell occupancy in blood, bone marrow, and tumor.[112] Furthermore, PET scanning can image physically labeled CAR T cells, which bypasses the requirement for a PET reporter. CAR T cells can be radiolabeled after manufacturing and prior to infusion. Lee et al. developed ^{89}Zr-*p*-isothiocyanatobenzyl-desferrioxamine (Df-Bz-NCS, DFO), which covalently labels 70-79% of CAR T cells with negligible impact on cell viability and proliferation. ^{89}Zr's long half-life (78.4 hours) makes this nuclide suitable for long-term *in vivo* tracking. PET scanning captured these cells as they migrated between lung, liver and spleen.[113]

Strengths of PET scanning include accessibility of PET scanners in the clinic, penetration of positrons through tissue, and the dual use of PET reporter also as a suicide safety switch.

Unlike BLI, PET scanning is widely used in the clinic. However, PET scanning shares some limitations with BLI, including lack of single-cell resolution and potential immunogenicity of the PET reporter. The latter limitation can be ameliorated with PET reporters that are based on endogenous human proteins (e.g., SSTR2 and NIS). However, background expression of endogenous human proteins may also obscure results. Finally, unlike with multiplexed BLI, PET scanning cannot multiplex different reporters since all reporter/probe pairs emit positrons. Hence, PET scanning cannot simultaneously image both CAR T and tumor cells.

Two-Photon Microscopy

Finally, two-photon microscopy can capture the distribution, motility, and functionality of CAR T cells *in vivo* at the single-cell level. With two-photon microscopy, one fluorophore simultaneously absorbs multiple (usually two) units of near-infrared (NIR) photons and emits a single unit of fluorescence. Since NIR photons minimize scattering and multiphoton absorption occurs rarely in an area of high photon density, two-photon microscopy has deep tissue penetration, superior spatial resolution, and diminished photobleaching. These qualities are ideal for *in vivo* live-imaging mouse experiments to capture single CAR T cells in action.[114] Hence, out of the three CAR detection methods at the organismal level, two-photon microscopy is the most suitable for mechanistic studies at the cellular level.

Cazaux et al. utilized intravital two-photon microscopy to track $GFP^{+}CD8^{+}$ anti-murine CD19 CAR T cells in a syngeneic lymphoma mouse model. In addition to CAR T-cell motility, two-photon microscopy was also used to measure calcium flux and detect apoptosis in CAR T cells and cancer cells respectively via Förster resonance energy transfer sensors. Two-photon microscopy demonstrated that: (1) B cells in circulation hindered CAR T cells from trafficking to the bone marrow; (2) CAR T cells killed both directly (through contact) and indirectly (through epitope spreading or cytokines); and (3) there is less immunosurveillance in lymph nodes than in bone marrow.[115] Furthermore, Mulazzani et al. used intravital two-photon microscopy to compare

GFP^+ anti-CD19 CAR T-cell infiltration into primary central nervous system lymphoma from intravenous and intracerebral CAR T-cell injection. Two-photon microscopy showed that intracerebral injection caused superior CAR T-cell infiltration and persistence, which was associated with long-term survival.[116] In addition to genetically encoded fluorescent proteins, two-photon microscopy can also involve inorganic fluorophores. Ma et al. developed biodegradable polydopamine nanodots with oxidation-induced fluorescence to track CAR T-cell targets *in vivo*. Polydopamine nanodots can be endocytosed by target cells and oxidized intracellularly for imaging. They demonstrated proof-of-principle in dissected mouse tissue.[117]

Two-photon microscopy is a powerful tool to capture *in vivo* CAR T-cell behavior and to generate novel hypotheses for CAR T-cell therapy failure and relapse. Its strengths (single-cell resolution, spatiotemporal resolution, tissue penetration) are ideal for mechanistic studies in mice. In addition, this method naturally links with other fluorescence-based tools, such as FRET sensors. However, unlike PET-based CAR tracking, two-photon microscopy cannot realistically be applied for clinical studies. Furthermore, two-photon microscopy requires equipment that might be inaccessible for many labs.

VI: Discussion

In this review, we summarized CAR detection methods that operate at the genomic, transcriptomic, proteomic, and organismal levels. We also identified key areas where CAR detection methods may be improved.

Based on the studies summarized in this review, we observed that development of new CAR detection methods has often proceeded through three phases. First, the new detection method is tested, validated, and optimized using CAR T cells generated from a healthy donor's T cells after transduction with a known CAR construct. Under this controlled scenario, the method's accuracy (e.g., false negative and false positive incidences) and reproducibility (e.g., error across replicates) can be measured and optimized. Second, the optimized detection method is applied on clinical CAR T-cell samples from patients, in order to demonstrate utility in a real-world scenario. Third, the results from the new detection method are compared with results obtained from existing detection methods. These three phases measure performance metrics and ensure utility for clinical studies. Although no standard guidelines exist for developing new CAR detection methods, we believe the three aforementioned phases can serve as practical guidelines for development of future CAR detection methods. Furthermore, if the detection method is to be used for clinical or diagnostic purposes, it should be accurate, reproducible, readily implemented, and easily interpreted. Results from one clinical laboratory should be replicable in another clinical laboratory. These suggestions complement Good Clinical Laboratory Practices (GCLP).

For CAR basic science studies, we believe that developing single-molecule microscopy-based CAR visualization will become increasingly important. The CAR has existed in its current form for years, but its molecular mechanisms are poorly understood or optimized. Although functionally similar to the TCR, the CAR traffics differently[92], and signaling is less efficient and sensitive[118]. Furthermore, CAR-induced tonic signaling hastens CAR T-cell exhaustion.[27,55] We believe CAR signaling inefficiencies should be understood via microscopy-based CAR immunological synapse visualization. Mechanistic insights from CAR immunological synapse visualization paired with new technologies, such as super-resolution or lattice light-sheet microscopy, may inform engineering endeavors that improve CARs.

For CAR clinical studies, we believe that developing PET-based *in vivo* CAR-tracking methods will become increasingly important. Since multiple clinical trials aim to extend CAR T-cell therapy from hematological cancers to solid tumors, the ability to measure CAR T-cell trafficking into the tumor without the need for a biopsy is essential. This is particularly important for tumors at physically hard-to-access locations. The recent clinical trial that utilizes HSV1-TK as a PET reporter is a promising start, but confounding variables (vascular leakage and glioma progression) obscured conclusions drawn from their data.[105] Newer CAR T-cell clinical studies that involve solid tumors should routinely employ PET scanning as both a research tool and on-treatment indicator of clinical efficacy. Meanwhile, other clinical studies should address the potential use of PET reporters as a CAR suicide safety switch.

VII: Acknowledgements

We thank Phi Beta Psi, the Ullman Fund in Cancer Immunology, the Hoogland Lymphoma Research Pilot Projects, and Chicago Immunoengineering Innovation Center for financial support. Yifei Hu is supported by the University of Chicago Medical Scientist Training Program NIGMS T32. We thank Dr. Nicholas Ankenbruck for helpful suggestions during manuscript preparations. All figures were generated with BioRender.com.

VIII: Contributions

Yifei Hu[1,2], Jun Huang[1]

[1]Pritzker School of Molecular Engineering, University of Chicago, Chicago, IL, United States

[2]Pritzker School of Medicine, University of Chicago, Chicago, IL, United States

J.H. conceived the original concept. Y.H. organized and wrote the manuscript.

SECTION III: ANTIGEN-MULTIMERS FOR CAR DETECTION[2]

Although chimeric antigen receptor (CAR) T-cell therapy has transformed cancer treatment, high-quality and universal CAR-staining reagents are urgently required to manufacture CAR T cells, predict therapy response, decipher CAR biology, and engineer new CARs. Here, we developed tetrameric and dodecameric forms of a multifunctional and extensible category of high-avidity CAR-staining reagents: antigen-multimers. Antigen-multimers detected CARs against CD19, HER2, and Tn-glycoside with significantly higher specificity, sensitivity, and precision than existing reagents. In addition to accurate CAR T-cell detection by flow cytometry, antigen-multimers also enabled ≥100-fold magnetic enrichment of rare CAR T cells, selective CAR T-cell stimulation, and high-dimensional CAR T-cell profiling by single-cell multi-omics analyses. Finally, antigen-multimers accurately captured clinical anti-CD19 CAR T cells from patients' cellular infusion products, post-infusion peripheral blood, and tumor biopsies. Antigen-multimers can be readily extended to other CAR systems by switching its antigen ligand. As such, antigen-multimers have broad clinical and research applications.

---

[2] This chapter is based on a published paper:
Hu, Y., Cao, G., Chen, X., Huang, X., Asby, N., Ankenbruck, N., Rahman, A., Thusu, A., He, Y., Riedell, P. A., Bishop, M. R., Schreiber, H., Kline, J., & Huang, J. (2021). Antigen multimers: Specific, sensitive, precise, and multifunctional high-avidity CAR-staining reagents. *Matter*, *4*, 1–24. https://doi.org/10.1016/j.matt.2021.09.027

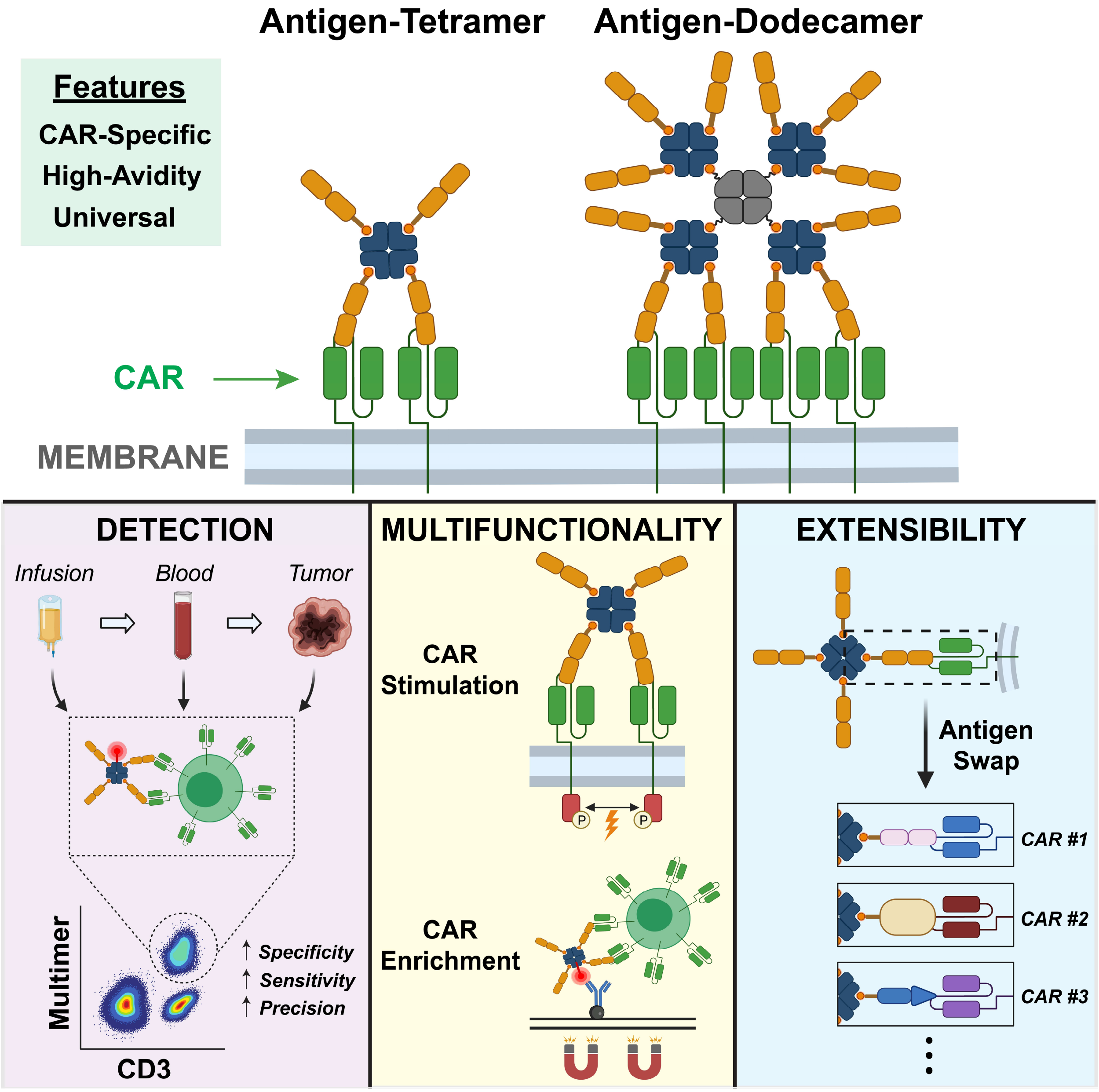

Figure III-1. Antigen-multimers: Specific, Sensitive, Precise, and Multifunctional High-Avidity CAR-Staining Reagents. Graphical abstract showing antigen-tetramers and antigen-dodecamers CAR-staining reagents. Antigen-multimers were designed for high-accuracy CAR-detection, multifunctionality, and extensibility to new CARs.

I: Introduction

Although CAR-staining reagents are essential for understanding and developing better CARs, each existing CAR-staining reagent has important shortcomings.[119] Generic CAR-staining reagents that bind the CAR scFv are limited by non-specific binding, incompatibility with other antibodies, and requirements for multi-step staining procedures.[67] Specific CAR-staining reagents (e.g., target antigen and anti-idiotype antibodies) can be commercially available, but often are limited by protein instability and high developmental cost.[71,74,79,120] Furthermore, all existing CAR-staining reagents are limited by ≤2-valency binding. Although higher avidity CAR-staining reagents may improve CAR-detection performance, such reagents have not been developed.[119]

To address these limitations, here we designed, constructed, tested, and validated tetrameric and dodecameric forms of a new, multifunctional, and extensible category of high-avidity CAR-staining reagents: antigen-multimers. According to results from cell lines and patient biospecimens, antigen-multimers enabled highly specific, sensitive, and precise CAR-detection, magnetic enrichment for sensitive detection of rare CAR T cells, temperature-controlled and specific CAR T-cell stimulation for activation phenotyping, and high-dimensional CAR T-cell profiling via single-cell multi-omics analyses. In addition, antigen-multimers successfully captured clinical anti-CD19 CAR T cells from patients' cellular infusion products, post-infusion peripheral blood, and tumor biopsies, underscoring their broad utility for clinical and translational research. Finally, antigen-multimers can be readily extended to existing and new CAR systems by switching its antigen ligand. We demonstrated this extensibility across three independent CAR systems (anti-CD19, anti-HER2, anti-Tn). Although we only tested antigen-tetramers and antigen-dodecamers in these current studies, antigen-multimers may also be extended to other valencies, such as dimers, pentamers, octamers, and dextramers.[121] Due to their multifunctional and extensible nature, antigen-multimers are a new class of CAR-staining reagents with broad CAR T-cell research and clinical applications.

II: Results

Antigen-multimer design and validation.

To generate high-avidity CAR-staining reagents for CAR T-cell detection, we designed, constructed, and validated two forms of antigen-multimers: antigen-tetramer and antigen-dodecamer. Analogous to MHC-multimers[77,122,123], antigen-multimers are comprised of the CAR antigen ligand multimerized on a streptavidin scaffold (**Figure III-2A**). The antigen ligand moiety is expected to bind the CAR with antibody-like affinity. We designed antigen-tetramers and antigen-dodecamers with 4-valency and 12-valency binding, respectively, in order to leverage higher-avidity binding for enhanced detection.

To construct antigen-tetramers, fluorescent tetrameric streptavidin was associated with four biotinylated antigen ligand molecules. To construct antigen-dodecamers, biotinylated tetrameric dodecamer base protein was associated with four fluorescent tetrameric streptavidin, each of which was further associated with three biotinylated antigen ligand molecules. For all experiments, antigen ligand molecules were site-specifically biotinylated instead of randomly biotinylated, in order to curtail higher-order oligomerization and steric obstruction of the CAR binding site.[124]

Next, we validated antigen-multimers on three 2nd-generation CARs: anti-CD19 CAR (clone FMC63), anti-HER2 CAR (clone 9), and anti-Tn CAR (clone 237) (**Figure III-2B**). From N-terminus to C-terminus, each validation CAR consists of an extracellular scFv, CD8α hinge and transmembrane region, 4-1BB and CD3ζ intracellular domains, and monomeric enhanced green fluorescent protein (meGFP). The C-terminal meGFP was included to track CAR transduction efficiency and expression. The hinge, transmembrane region, and intracellular domains were designed identically to the clinical CAR construct used in tisagenlecleucel. The anti-CD19 and anti-HER2 CARs utilize human domains while the anti-Tn CAR utilizes murine domains. Our three validation CARs can test antigen-multimers for utility: (1) in clinical research, since our anti-CD19

CAR utilizes the same FMC63-based scFv as in clinical CD19-directed CAR therapies; (2) under CAR binding affinities widely ranging from 0.3 nM to 140 nM[125–127]; and (3) under antigen ligand molecular sizes widely ranging from 2.6 kDa to 73 kDa.

Antigen-multimers stain CARs directed against CD19, HER2, and Tn-glycoside.

Staining capabilities of antigen-multimers were first examined on CAR-transduced cell lines, including human Jurkat cells and murine $58^{-/-}$ hybridoma cells. The meGFP-tag on the CAR served as a marker for successful CAR transduction and expression (figure III-S1A-C). Subsequently, CD19-multimers, HER2-multimers, and Tn-podoplanin peptide-multimers (Tn-PDPN-multimers) were titrated to stain CAR-meGFP cell lines. The monomeric antigen ligand was included as a control for avidity. Staining reagent and meGFP fluorescence intensities were simultaneously measured by flow cytometry.

Staining titrations demonstrate that CD19-multimers, HER2-multimers, and Tn-PDPN-multimers stained their matched CAR-transduced cell lines (**Figure III-2C, III-2F, III-2I**). Untransduced cells were negligibly stained. Furthermore, a negative control (BSA-multimers) generated minimal non-specific fluorescence (figure III-S1D-E). Higher antigen-multimer concentrations stained more cells (**Figure III-2D, III-2G, III-2J**). At the highest concentrations, antigen-tetramers and antigen-dodecamers equally captured ≥92% of their matched target cells. Higher antigen-multimer concentrations also stained with greater mean fluorescence intensity (**Figure III-2E, III-2H, III-2K**). These findings indicate that high-avidity antigen-multimers stain matched CARs in a dose-dependent manner, while generating negligible non-specific fluorescence (with both biological and BSA-multimer controls).

At equimolar concentrations, antigen-dodecamers enhanced fluorescence relative to antigen-tetramers. Furthermore, both antigen-multimers enhanced fluorescence relative to the monomeric antigen ligand. The magnitude of these enhancements positively correlated with the dissociation constant of the CAR for its antigen ligand. Fluorescence enhancement by avidity was marginal when staining the anti-CD19 CAR (K_D = 0.3 nM), moderate when staining the anti-HER2 CAR (K_D = 1 nM), and substantial when staining the anti-Tn CAR (K_D = 140 nM). For the Tn-PDPN ligand, Tn-PDPN-dodecamers caused up to 4-fold greater fluorescence than Tn-PDPN-tetramers, while monomeric Tn-PDPN completely failed to stain at similar concentrations (**Figure III-2K** and figure III-S1F). Monomeric Tn-PDPN only stained the anti-Tn CAR at >1000-fold higher concentrations (figure III-S1G). Hence, the binding avidity of an antigen-multimer enhances its staining capability, particularly for lower affinity CARs.

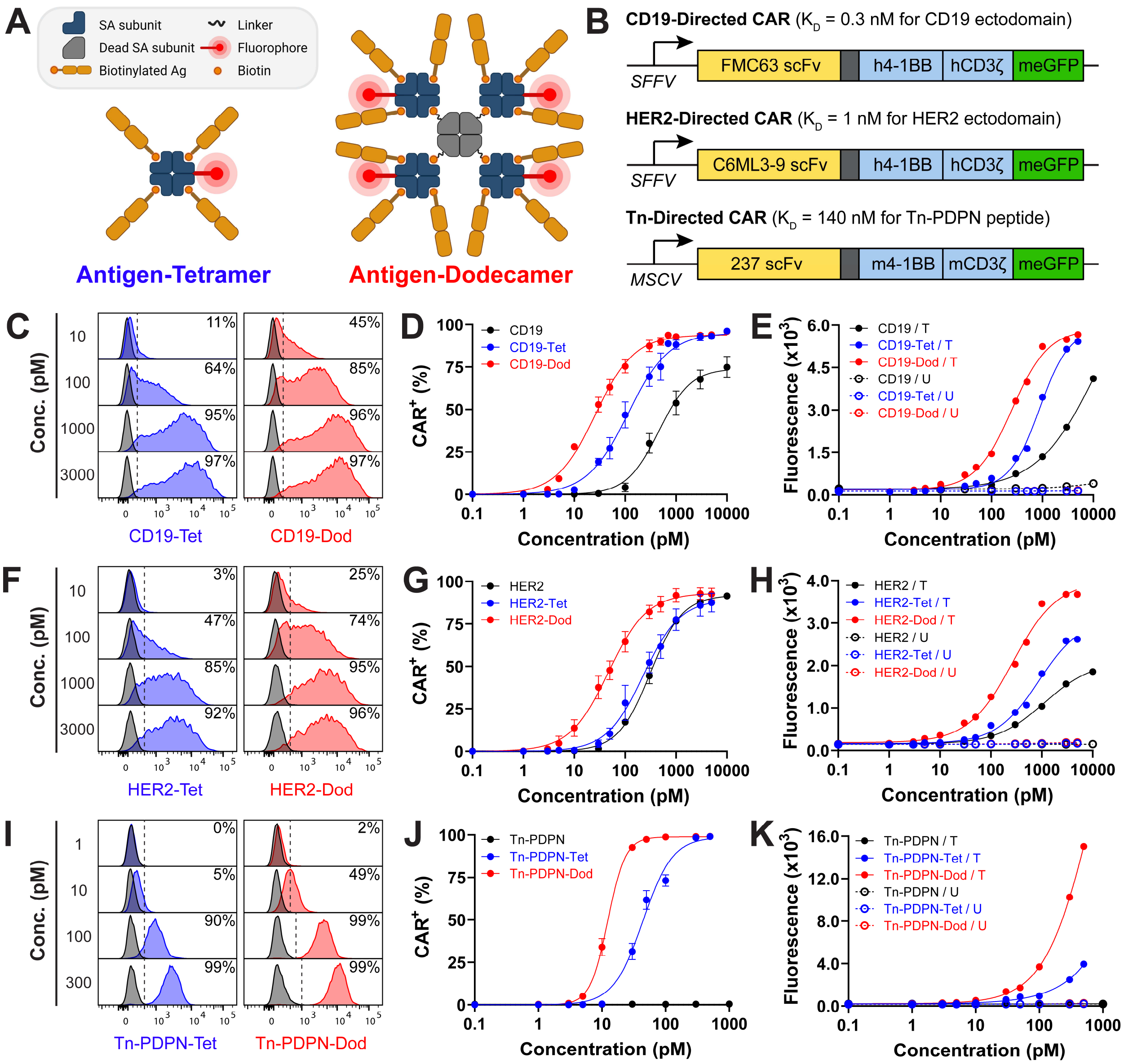

Figure III-2. Antigen-multimer design and validation in CARs directed against CD19, HER2, and Tn-glycoside. (A) Cartoon depicting antigen-tetramer and antigen-dodecamer with each major molecular component. (B) Diagram depicting CD19-, HER2-, and Tn-directed CAR constructs used to validate antigen-multimers. Each CAR contains a C-terminal meGFP to track CAR expression. CAR transcription is directed by either a spleen focus-forming virus (SFFV) or a murine embryonic stem cell virus (MSCV) promoter. (C,F,I) Staining titration of three types of antigen-tetramers (blue) and antigen-dodecamers (red) on their matched CAR-transduced cell lines. Staining of the untransduced cell line is shown in gray and used for gating. Histograms are representative of three independent titrations. (D,G,J) Triplicate staining titration results for antigen-tetramers, antigen-dodecamers, and monomeric antigen controls were fitted to dose-response curves. The mean ± standard error of the mean is depicted for each concentration. (E,H,K) Plots from representative titrations (fitted to dose-response curves) showing the relationship between geometric mean fluorescence intensity and staining reagent concentration on CAR-transduced (T) and untransduced cell lines (U). Associated with Figure III-S1.

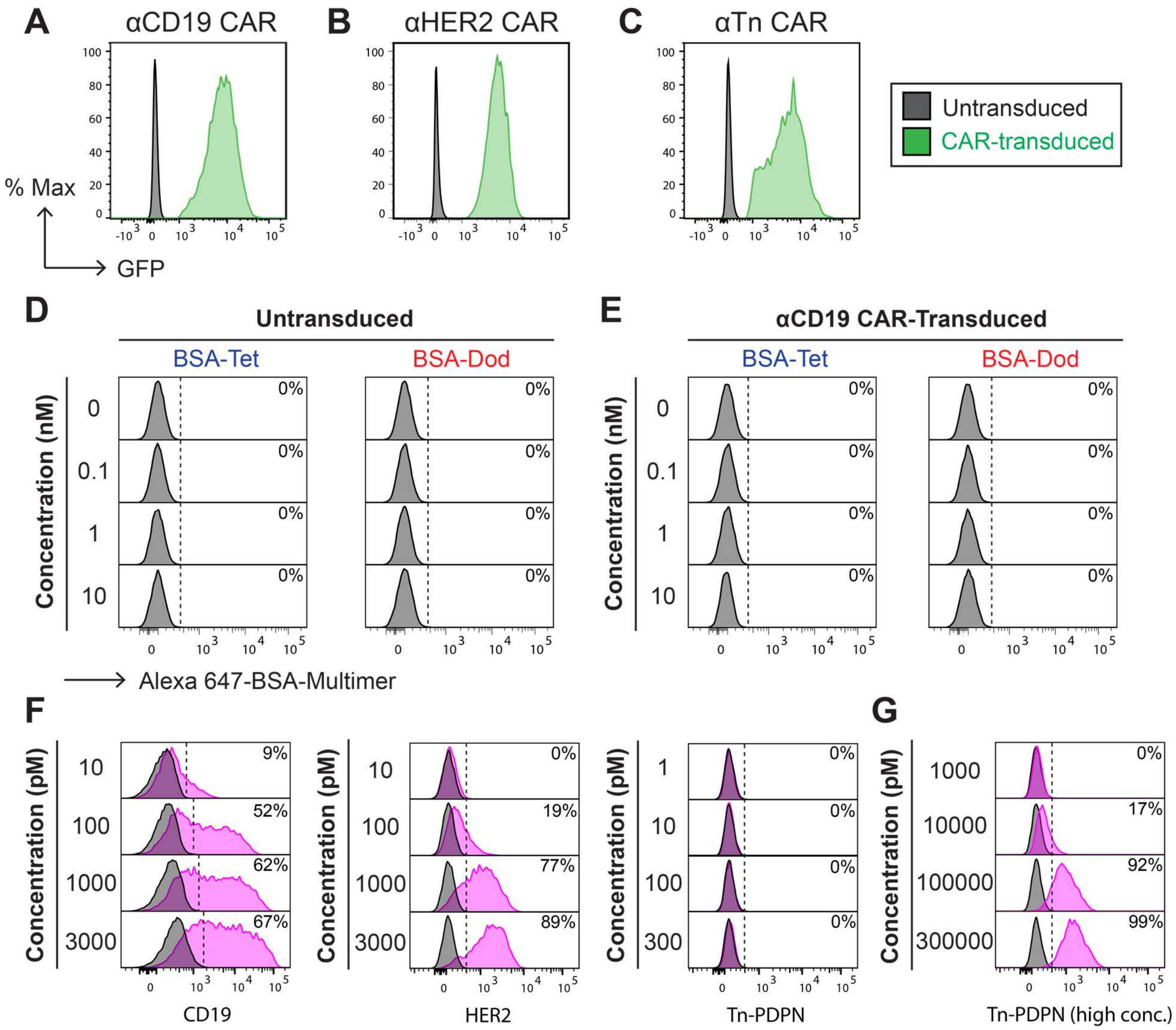

Figure III-S1. CAR transduction, monomeric target antigen controls, and BSA-multimers negative controls. (A-C) Histograms showing transduction of monomeric enhanced GFP-tagged CARs directed against CD19, HER2, and Tn-glycoside into human Jurkat cells (anti-CD19 and anti-HER2 CARs) or murine $58^{-/-}$ hybridoma cells (anti-Tn CAR). Untransduced cells served as negative controls. (D-E) Histograms showing titration (from 0.1 to 10 nM) of Alexa 647-labeled bovine serum albumin-multimers (BSA-multimers) on untransduced and αCD19-CAR-transduced Jurkat cells. Gates to quantify non-specific staining percentage from the isotype control were established based on cells not stained with BSA-multimers (0 nM). (F) Staining titration of monomeric CD19, HER2, or Tn-PDPN on their matched CAR-transduced cell lines. Staining of the untransduced cell line is shown in gray and used for gating. (G) Staining titration of monomeric Tn-PDPN at 1000-fold higher concentrations. Associated with Figure III-2.

Antigen-multimers are highly specific.

Having titrated three types of antigen-tetramers and antigen-dodecamers against their respective matched CARs, we further examined antigen-multimers for staining specificity. One source of non-specificity is staining of cells not expressing CARs. Another source of non-specificity is staining of cells expressing unmatched CARs. For example, CD19-multimers should not stain cells expressing anti-HER2 or anti-Tn CARs. Our staining results demonstrate that antigen-tetramers (**Figure III-3A**) and antigen-dodecamers (**Figure III-3B**) stained ≥90% of their matched CAR-transduced cell lines. On the other hand, staining of untransduced cells and non-matched CAR-transduced cell lines were equally negligible (≤1%). Therefore, antigen-multimers are highly CAR-specific.

Then, we evaluated the staining specificity of existing generic CAR-staining reagents: polyclonal anti-IgG antibodies and Protein L.[67,119] Since both CAR-staining reagents bind to F_{ab}-like molecules on the cell surface, neither can discriminate between different CARs. Relative to antigen-multimers, polyclonal anti-IgG antibodies (**Figure III-3C**, top) provided equivalent staining of anti-HER2 and anti-Tn CARs. However, anti-IgG antibodies were significantly less efficient than CD19-multimers in staining the anti-CD19 CAR, due to substantial non-specific staining of untransduced cells. Protein L (**Figure III-3C**, bottom), which binds to immunoglobulin κ light chains, stained the anti-CD19 CAR, but the anti-HER2 CAR was barely stained, and the anti-Tn CAR was not stained. This inconsistency across different CARs may be due to the differential affinity of Protein L for alternative κ light chains. These observations support the conclusion that antigen-multimers are more specific than existing generic CAR-staining reagents.

Finally, we evaluated the staining specificity of a commercially available anti-FMC63 anti-idiotype antibody, which was specifically designed to detect the FMC63-based anti-CD19 CAR. However, this antibody does not stain all anti-CD19 CARs under clinical or preclinical investigation.[125,128] At the highest concentrations, anti-FMC63 captured 83% of anti-CD19 CAR cells (figure III-S2A-B), which was lower than CD19-tetramers (93%) and CD19-dodecamers

(90%) did at saturation. Non-specific staining of untransduced cells was negligible (figure III-S2C). Based on these findings, while anti-FMC63 are equally as specific as CD19-multimers, they are less efficient staining reagents for generating fluorescence at saturation (figure III-S2D-E). The decreased efficiency can be explained by decreased binding avidity for the anti-CD19 CAR.

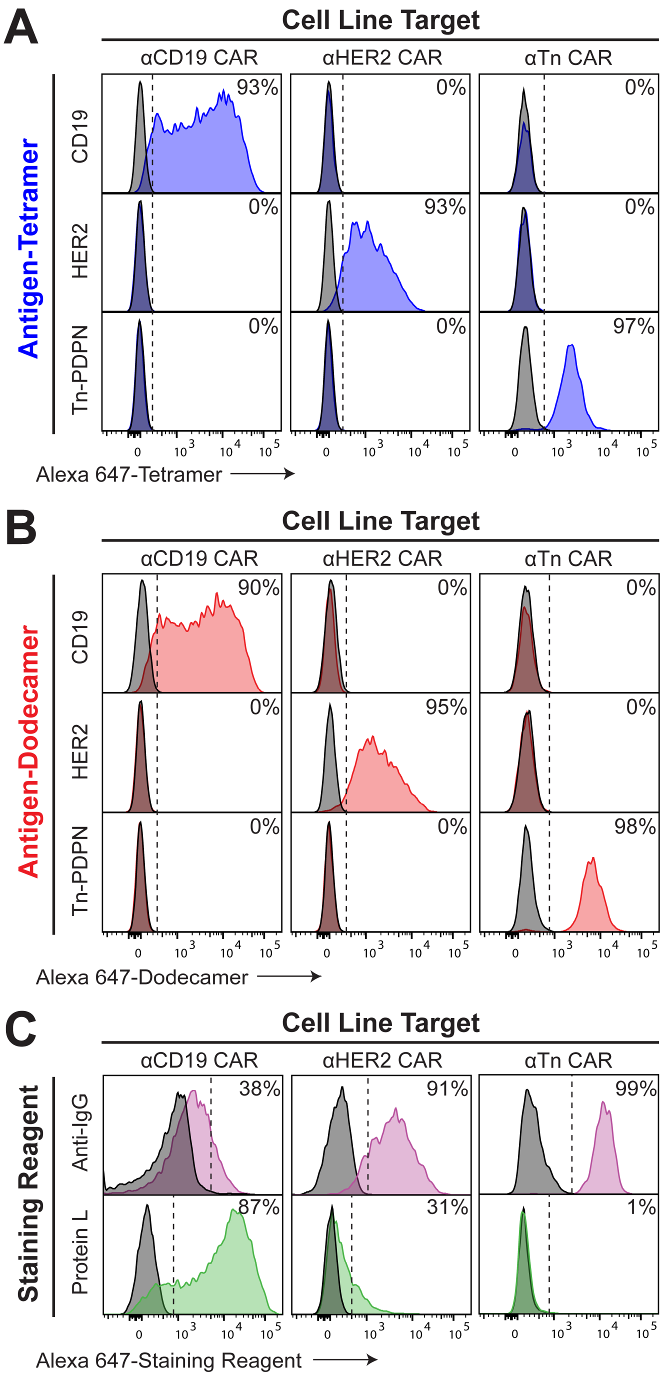

Figure III-3. Antigen-multimers are highly specific. (A-B) Antigen-tetramers (A) and antigen-dodecamers (B) were evaluated for specificity by staining cell lines transduced with CD19-, HER2-, and Tn-directed CARs. Staining of untransduced cell lines is shown in gray and used for gating. (C) Similar staining assays were conducted with existing CAR-staining reagents, which include polyclonal anti-IgG antibodies and Protein L. Staining of untransduced cell lines is shown in gray and used for gating. Histograms are representative of three independent staining experiments. Associated with Figure III-S2.

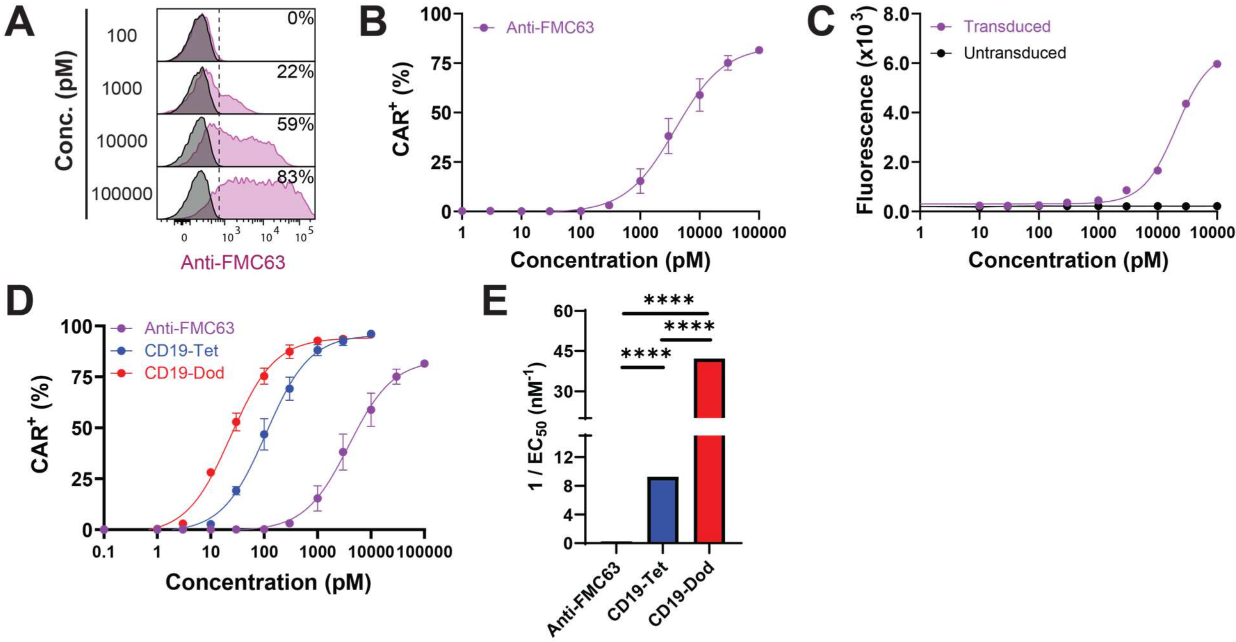

Figure III-S2. Titrations of an anti-FMC63 antibody for anti-CD19 CAR T cells. (A) Histograms showing titration of an anti-idiotype antibody (anti-FMC63) against anti-CD19 CAR-transduced Jurkat cells. Gates were drawn from staining of untransduced Jurkat cells. Histograms are representative of three independent titrations. (B) Triplicate staining titration results were fitted to dose-response curves. The mean ± standard error of the mean is depicted for each concentration. (C) Plots from a representative titration (fitted to dose-response curves) showing the relationship between geometric mean fluorescence intensity and staining reagent concentration on CAR-transduced and untransduced cell lines. (D-E) Comparison between staining titration results from anti-FMC63, CD19-tetramers, and CD19-dodecamers. Staining EC_{50} values were extrapolated from dose-response curves (left). For each staining reagent, $1/EC_{50}$ was plotted on a bar graph (right). Fitted EC_{50} values were compared with a sum-of-squares *F*-test, whereby **** denotes $p<0.0001$. Associated with Figure III-3.

Antigen-multimers are highly sensitive and precise.

After examining detection specificity, we evaluated antigen-multimers for detection sensitivity and precision. These metrics were measured by applying CD19-multimers to detect meGFP-tagged anti-CD19 CAR cells that are spiked into mCherry-tagged non-CAR cells for analysis by flow cytometry (**Figure III-4A**). Sensitivity was measured by monitoring for false negatives. Precision was measured by monitoring for false positives.

Sensitivity and precision are most critical when CAR cells are rare and CAR expression is low. These conditions are biologically relevant since CAR T cells downmodulate CAR expression after antigen-engagement.[28,56,129] To simulate these conditions, spike-in experiments were performed with two monoclonal cell lines with stably low CAR expression: “low clone” and “mid clone” (figure III-S3A-D). The low clone (~150,000 CAR molecules per cell) expresses less CAR than the mid clone (~250,000 CAR molecules per cell). Both clones express less CAR than the pre-sorted polyclonal CAR cells (~330,000 CAR molecules per cell) used for previous staining assays. Finally, non-CAR cells were transduced with mCherry to provide an additional distinction between CAR and non-CAR cells.

In spike-in experiments, we targeted cell mixtures with CAR cell prevalence between 10% and 0.01%. However, the true CAR cell prevalence in each cell mixture was measured by percentage of GFP$^+$ cells. Both CD19-tetramers and CD19-dodecamers specifically stained CAR cells (**Figure III-4B**). As expected, the mid clone was stained more than the low clone (figure III-S3C). For both clones, CD19-multimers accurately captured CAR cell prevalence down to 0.1%. Sensitivity remained ≥90% down to 0.1% (**Figure III-4C-D**). Precision differed between CD19-tetramers and CD19-dodecamers at lower CAR cell prevalence. For the mid clone, CD19-dodecamers captured a purer population than CD19-tetramers did below 1% CAR cell prevalence. For the low clone, CD19-dodecamer captured a purer population than CD19-tetramers did below 10% CAR cell prevalence. Our results demonstrate that CD19-multimers stain with high sensitivity and precision. Importantly, CD19-multimers can sensitively isolate a highly pure (≥90%) CAR cell population from Jurkat cell mixtures, even when CAR cells have low CAR expression and are exceptionally rare (≤1%).

Next, we performed spike-in experiments with existing CAR-staining reagents: monomeric CD19, polyclonal anti-IgG antibodies and Protein L (figure III-S3E-G). Monomeric CD19 staining was comparable to CD19-multimer staining for the mid clone. However, detection sensitivity was reduced for the low clone, which suggests that binding avidity increases detection sensitivity for

CAR T cells with lower CAR expression. Anti-IgG antibodies failed to detect both clones with low CAR expression. Sensitivity and precision were ≤10% at all CAR cell prevalence. Protein L marginally detected some mid clone cells, but failed to detect low clone cells. For detection of the mid clone, precision was ≥90% at 10% CAR cell prevalence, but rapidly dropped at lower CAR cell prevalence. Sensitivity never exceeded 10%. These results suggest that neither polyclonal anti-IgG antibodies nor Protein L can capture CAR T cells from cell mixtures when CAR T cells (at any rarity) express fewer CAR molecules per cell.

Finally, we evaluated the detection sensitivity of monomeric CD19 and CD19-multimers under more physiological cell mixtures. Post-infusion CAR T cell therapy patient biospecimens were modeled by spiking the low clone into human peripheral blood lymphocytes at 1% prevalence (figure III-S4A). Since the CAR contained a GFP label, we checked the accuracy of our spike-in via flow cytometry (figure III-S4B). This mixture captures both CAR downmodulation[28,56,129] and potential low prevalence[4] of post-infusion patient CAR T cells. Subsequently, we performed full-dose titrations to compare the abilities of multimers and monomers to detect low clone cells in this mixture. Multimers outperformed monomers across all concentrations (figure III-S4C). At saturation, monomers missed ~24% of CAR cells that were detectable by multimers (figure III-S4D). Furthermore, compared to monomers, tetramers and dodecamers exhibited 6-fold and 19-fold lower staining EC_{50} respectively (figure III-S4E). These findings are consistent with results from cell line mixtures (**Figure III-4C**), and support our conclusion that binding avidity enhances detection sensitivity.

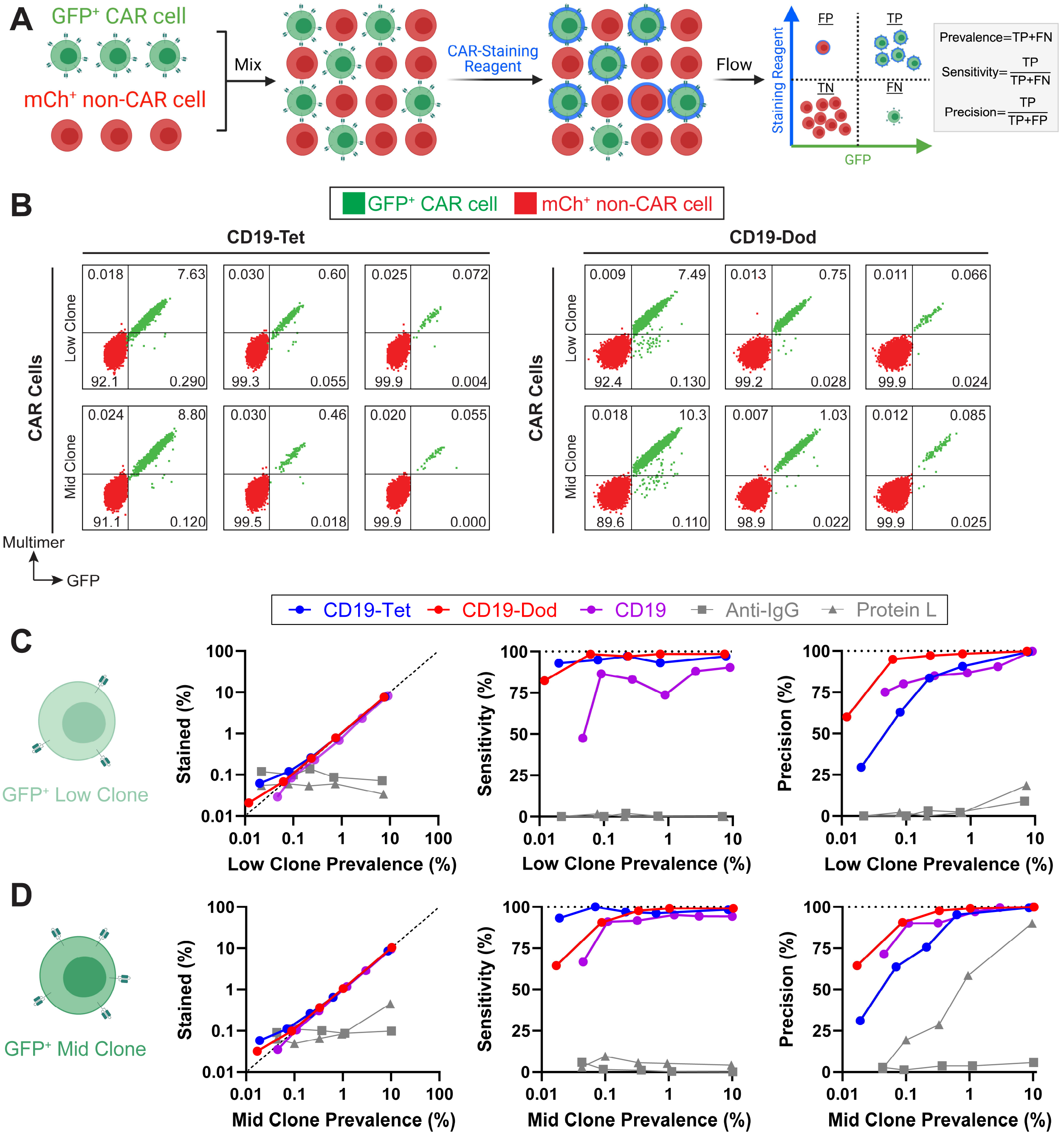

Figure III-4. Antigen-multimers are highly sensitive and precise. (A) Diagram depicting spike-in assays to measure a CAR-staining reagent's sensitivity and precision. Cell mixtures, constructed from CAR-meGFP-expressing cells and mCherry-expressing non-CAR cells, were stained with a CAR-staining reagent. After analysis by flow cytometry, the cells were placed into four categories: true positives (TP), true negatives (TN), false positives (FP), and false negatives (FN). Formulas to calculate prevalence, sensitivity, and precision are depicted. (B) Two anti-CD19 CAR-meGFP-transduced clones ("low clone" on top row and "mid clone" on bottom row) with low CAR expression were spiked into mCherry-expressing non-CAR cells. The prevalence of CAR cells was measured by percentage of meGFP+ cells by flow cytometry. Subsequently, CD19-tetramers (left) or CD19-dodecamers (right) were applied.

Figure III-4, continued. Cells on the flow plots are colored according to fluorescent protein expression. (C-D) The prevalence of CAR cells (meGFP$^+$) in cell mixtures plotted against the percentage of cells stained by CAR-staining reagents (left), sensitivity of detection (middle), and precision of detection (right) from spike-in assays with the low clone (C) and mid clone (D). For the stained percentage plot, if a point lies on the dotted line of unity, then the staining reagent accurately captured CAR cell prevalence. For the sensitivity and precision plots, if a point lies on the dotted line (100%), then the staining reagent was completely accurate in discriminating CAR cells from non-CAR cells. Associated with Figures III-S3 and III-S4.

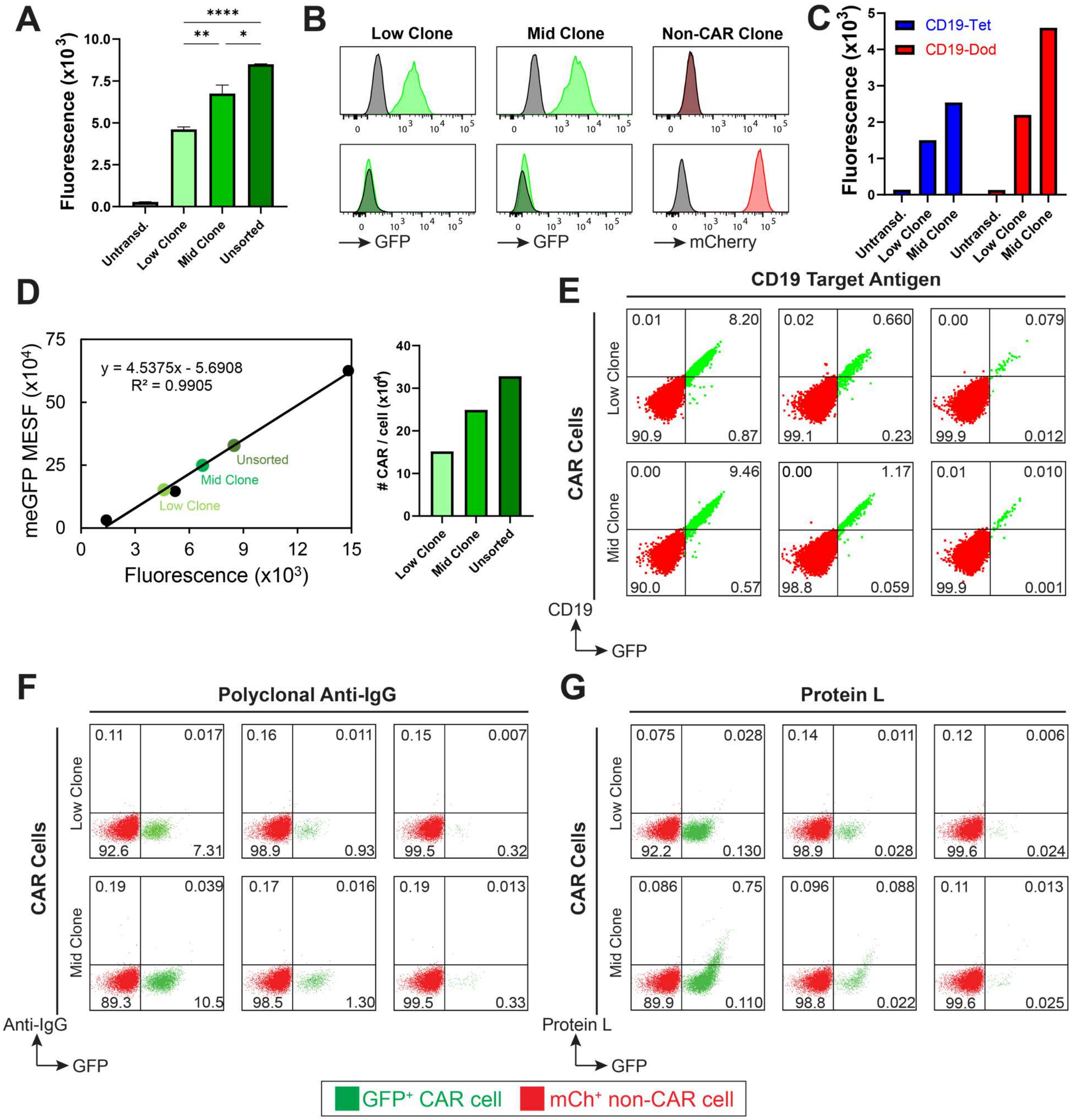

Figure III-S3. Sensitivity and precision of CAR-staining reagents. (A) Bar graph showing CAR expression (through meGFP fluorescence) in two anti-CD19 CAR-transduced Jurkat cell clones (named "low clone" and "mid clone") that were sorted for stably low CAR expression. The untransduced and pre-sort fluorescence are shown for comparison. CAR expression was compared by one-way ANOVA and post-hoc *t*-tests (Sidak multiple comparison correction), whereby * denotes $p<0.05$, ** denotes $p<0.01$, *** denotes $p<0.001$, and **** denotes $p<0.0001$. (B) Histograms showing expression of monomeric enhanced GFP-labeled CARs (top) and mCherry (bottom) on both CAR cell clones and the non-CAR cell clone. These three clones were used to quantify sensitivity and precision in cell mixtures. (C) Bar graph showing geometric mean fluorescence intensity of AF647-labeled antigen-multimer staining (3 nM) on untransduced, low clone, and mid clone cells.

Figure III-S3, continued. (D) Line plot showing three standards (black points) used to correlate meGFP fluorescence with equivalent numbers of meGFP molecules. These points were used to construct a standard curve to measure the average CAR expression of the low clone, mid clone, and the original unsorted polyclonal CAR-transduced population, which is depicted on the bar graph. (E-G) meGFP$^+$ anti-CD19 CAR cells ("low clone" on top row and "mid clone" on bottom row) were spiked into mCherry$^+$ non-CAR cells at various proportions. Subsequently, monomeric CD19 (E), polyclonal anti-IgG (F) or Protein L (G) were applied to detect CAR cells by flow cytometry. CAR and non-CAR cells are colored according to the legend (bottom). Associated with Figure III-4.

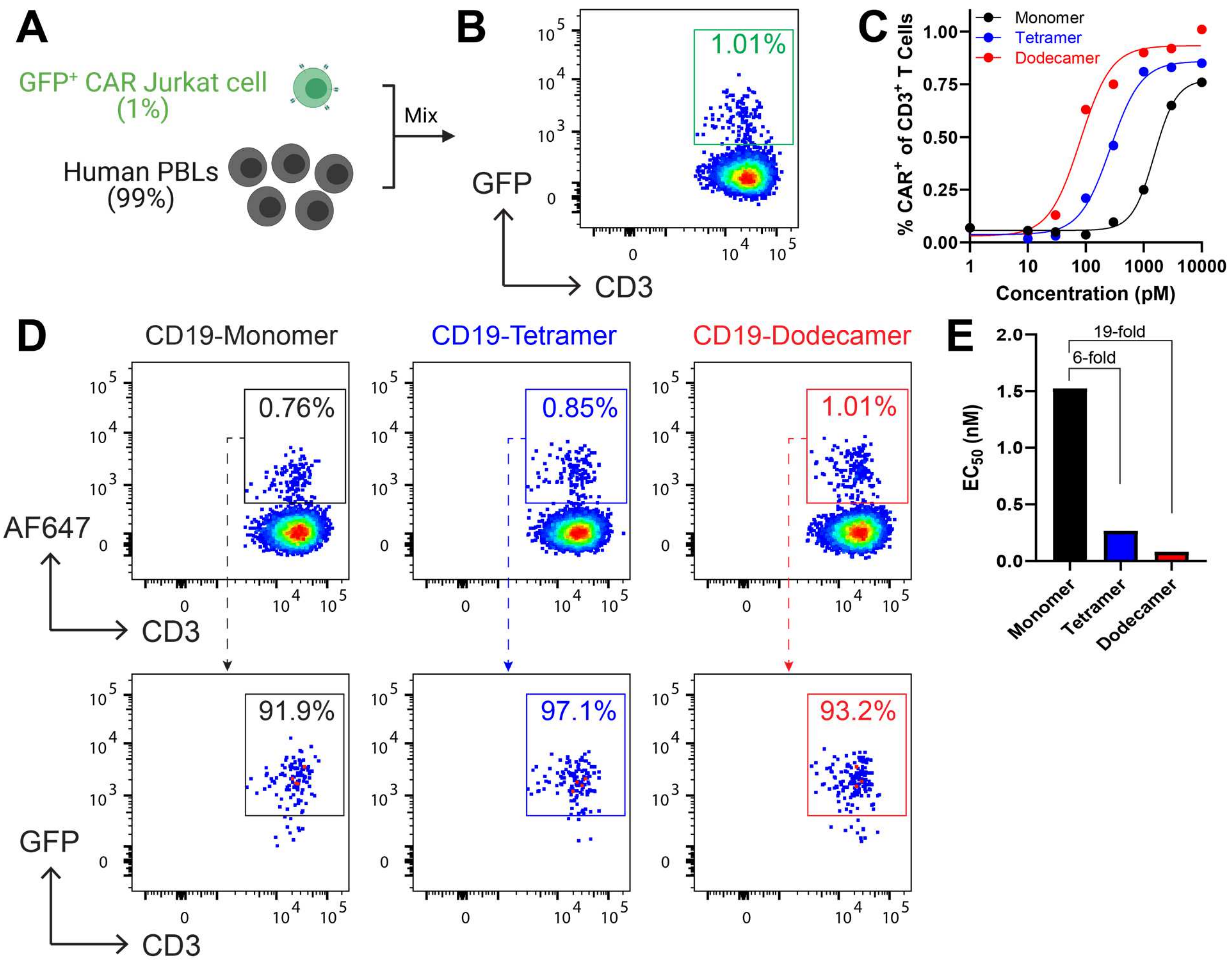

Figure III-S4. Detection sensitivity of CD19-multimers and CD19-monomers in CAR T cell mixtures. (A-B) A mixture consisting of CAR-Jurkat cells with low CAR expression (1%) and human PBLs (99%) was constructed and validated by flow cytometry. (C) Multimeric and monomeric CD19 were titrated, and the detection percentage was fitted to dose-response curves. (D) Flow-plots showing Alexa 647-labeled CD19-multimer and CD19-monomer staining results at saturation (top row). Stained cells were gated and checked for CAR expression by GFP fluorescence (bottom row). (E) Staining EC_{50} was plotted for each staining reagent. Fold-change comparisons between multimeric and monomeric EC_{50} values was denoted. Associated with Figure III-4.

Antigen-multimers magnetically enrich for CAR T cells.

Having established antigen-multimers as highly sensitive CAR-staining reagents even for cells with low CAR expression, we predicted that antigen-multimers can enrich rare CAR T cells from cell mixtures. CAR T-cell enrichment is expected to facilitate the detection and investigation of rare CAR T-cell subsets.[122] Importantly, CAR T cells can be rare *in vivo*, particularly those with a persistent, resting memory phenotype which are correlated with durable responses in patients.[130] Moreover, CAR T-cell enrichment may be useful during CAR T-cell infusion product manufacturing if CAR-transduction efficiency is low.

To perform CAR T-cell enrichment with antigen-multimers, we magnetically selected for CAR cells by adapting a method employed with MHC-tetramers (**Figure III-5A**).[131] Cells were stained, first with allophycocyanin (APC)-labeled CD19-tetramers or dodecamers, and second with anti-APC antibodies conjugated to magnetic particles (anti-APC microbeads). The stained populations were applied to a magnetic column. Non-CAR cells did not bind the column and were removed (negative selection). CAR cells were subsequently eluted under pressure after removal of the magnet (positive selection).

We employed this magnetic selection strategy to enrich for meGFP$^+$ CAR cells spiked into mCherry$^+$ non-CAR cells. To simulate difficult enrichment conditions, we used CAR cells with stably low CAR expression (low clone and mid clone, previously described in figure III-S3A-D). CAR cells in initial stained populations were rare (~0.2%, **Figure III-5B**). Based on CAR cell prevalence in the flow through, ~35% and ~55% of low clone and mid clone CAR cells respectively were retained on the column (**Figure III-5C**). After negative selection, eluted cells exhibited >100-fold higher CAR cell prevalence (**Figure III-5D**). Moreover, APC-fluorescence in eluted cells was substantially higher than in initial stained populations (figure III-S5). Relative to tetramers, dodecamers enriched more efficiently. This observation is expected because dodecamer staining results in higher fluorescence than tetramer staining. These results demonstrate that antigen-multimers can magnetically enrich for rare CAR T cells with low CAR expression.

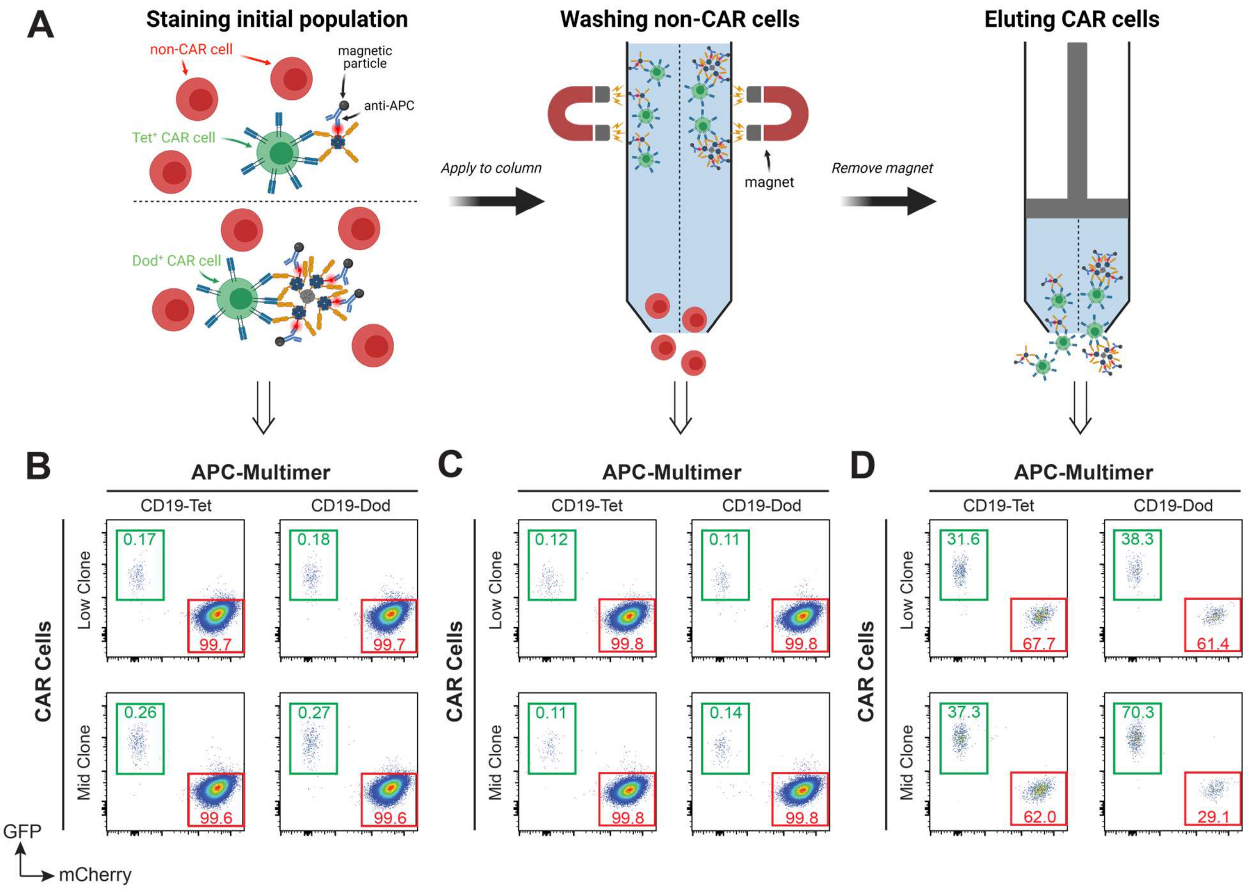

Figure III-5. Antigen-multimers magnetically enrich for CAR T cells. (A) Cartoon depicting magnetic enrichment procedure. Mixtures of meGFP⁺ CAR cells and mCherry⁺ non-CAR cells were stained with either APC-labeled antigen-tetramers or antigen-dodecamers, followed by staining with anti-APC magnetic microbeads. The stained cell mixture (left) is applied to a magnetic column for negative (middle) and positive (right) selection. (B-D) Flow plots showing prevalence of meGFP⁺ CAR cells and mCherry⁺ non-CAR cells ("low clone" on top row and "mid clone" on bottom row) under magnetic enrichment with antigen-tetramers or antigen-dodecamers. The initial stained mixture, column wash, and column elution are shown in B, C, and D respectively. Associated with Figure III-S5.

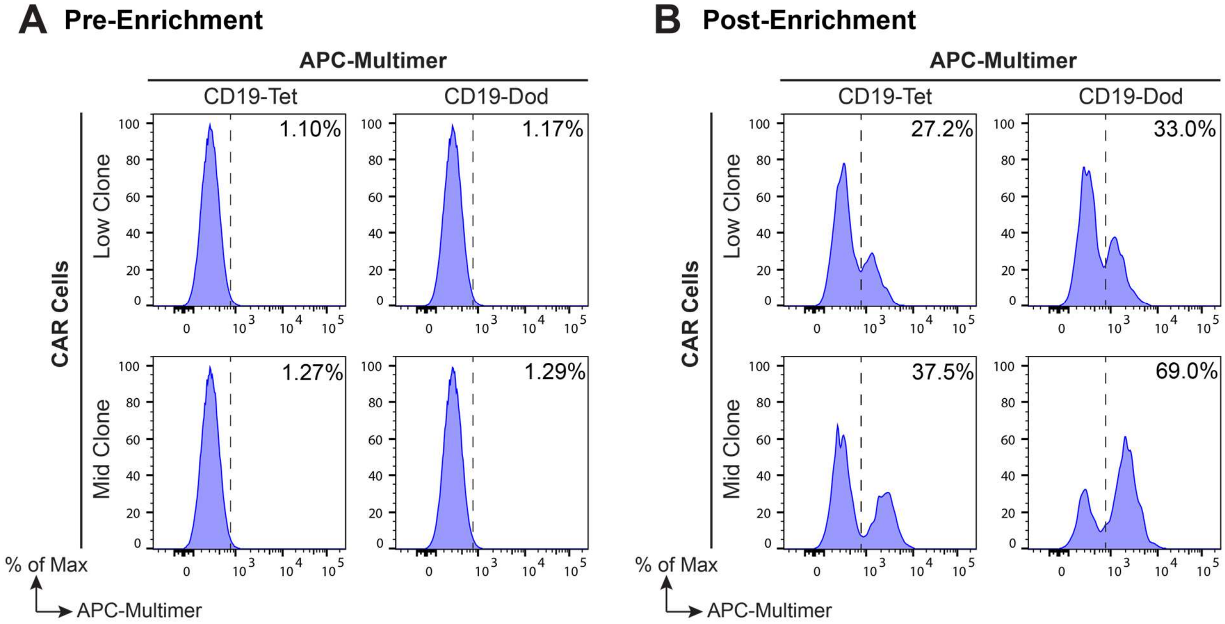

Figure III-S5. APC-labeled CD19-multimer staining of CAR T cells from magnetic enrichment. (A-B) Histograms show APC-multimer staining of the cell mixture ("low clone" on top row and "mid clone" on bottom row) before (A) and after (B) magnetic enrichment with antigen-tetramers or antigen-dodecamers. Gates are established from a fluorescence-minus-one control. Associated with Figure III-5.

Antigen-multimers specifically stimulate CAR T cells in a temperature-controlled manner.

Next, we determined if antigen-multimers can oligomerize CARs and stimulate CAR T cells.[132] CAR-specific stimulation would characterize a CAR T cell's activation phenotype, which can be associated with *in vivo* CAR T-cell efficacy.[23,133] Traditionally, a T cell's activation phenotype can be characterized with T-cell mitogens, such as anti-CD3/CD28 antibodies, phorbol 12-myristate 13-acetate (PMA)/ionomycin treatment, or phytohemagglutinin (PHA) treatment. However, these mitogens are neither CAR-specific nor mimic biologically relevant CAR stimulation. Alternatively, CAR-specific stimulation can be performed by incubating CAR T cells on plates pre-coated with CAR-staining reagents.[56,134,135] The surface enhances the CAR-staining reagent's binding avidity. Since antigen-multimers already bind the CAR with higher avidity, we predicted that they could activate CAR T cells directly as soluble reagents.

Incubation of 2nd-generation anti-CD19 CAR cells with CD19-tetramers or CD19-dodecamers at 37°C upregulated both CD69 (early activation marker, **Figure III-6A**) and CD25 (later activation marker, **Figure III-6B**). Higher multimer concentrations caused greater percentage of $CD69^+$ and $CD25^+$ cells (**Figure III-6C**). On the other hand, although the anti-FMC63 antibody can stain the CAR, it did not stimulate at any concentration in its soluble form. Multimer-stimulated CAR cells also secreted IL-2. IL-2 secretion correlated with CD69 and CD25 upregulation. At 0.3 nM, dodecamers stimulated more effectively than tetramers did. At 3 nM, both multimers stimulated equally well. Similar results were obtained with 1st-generation anti-CD19 CAR cells (figure III-S6A-C). Stimulation with either tetramers or dodecamers did not influence cell viability (figure III-S6D). These results demonstrate that antigen-multimers stimulate CAR T cells as high-avidity, soluble staining reagents at 37°C. On the contrary, the anti-FMC63 antibody did not stimulate CAR T cells, presumably due to lower binding avidity or affinity. Attachment of the anti-FMC63 antibody to solid surfaces will likely increase its CAR stimulation capabilities.

Next, we similarly incubated CAR cells with CD19-multimers at 4°C to simulate staining incubations (**Figure III-6D**). The lower temperature is predicted to slow metabolism and minimize CAR signaling. As predicted, no CD69 or CD25 upregulation was observed with either multimer at any concentration. Similarly, no IL-2 was secreted. Cell viability was not affected (figure III-S6D). Therefore, stimulation by antigen-multimers is abrogated at lower temperatures. These results suggest that when antigen-multimers are used for CAR-detection, the staining incubation can be performed at 4°C to avoid unwanted stimulation, as we did for all staining experiments in this study.

Finally, we probed two possible mechanisms for CAR T-cell activation by antigen-multimers (figure III-S7A). Antigen-multimers can bind CARs in *cis*, causing CAR-crosslinking and oligomerization. Alternatively, antigen-multimers can bind CARs in *trans*, causing cell-cell conjugation and kinetic segregation.[136] After stimulating CAR cells with antigen-multimers at 37°C, we found that antigen-multimers do not cause cell-cell conjugation (figure III-S7B). Therefore, *cis* CAR oligomerization, rather than *trans* cell-cell conjugation, is the likelier mechanism for multimer-induced CAR T-cell stimulation.

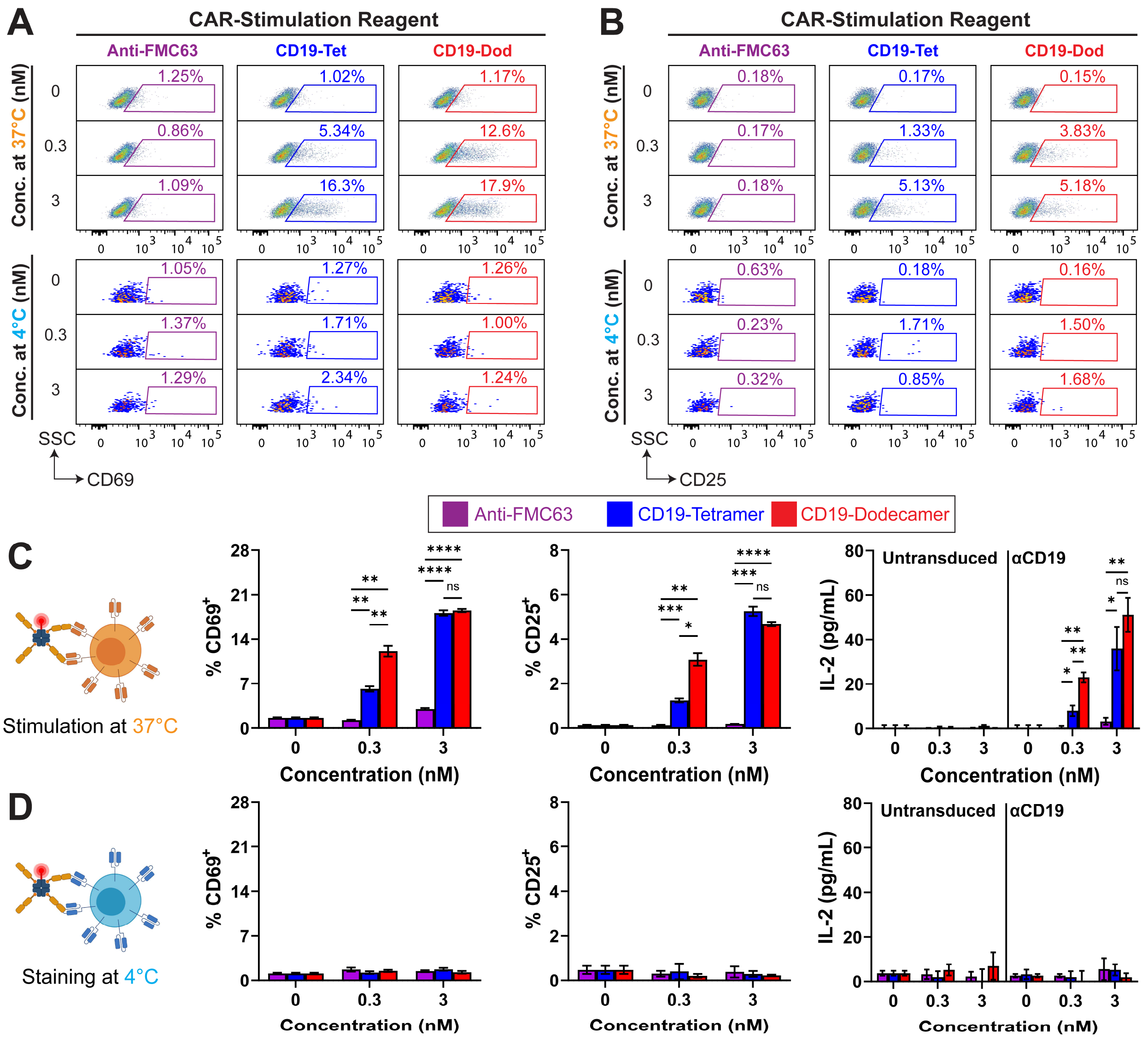

Figure III-6. Antigen-multimers specifically stimulate CAR T cells in a temperature-controlled manner. (A-B) Representative flow plots showing expression of CD69 (left) and CD25 (right) on anti-CD19 CAR-transduced cells after incubation with anti-FMC63, CD19-tetramers, or CD19-dodecamers at various concentrations at 37°C (top row) and 4°C (bottom row). (C-D) Bar graphs depicting CD69 expression (left), CD25 expression (middle), and IL-2 secretion (right) of quadruplicate data from staining of anti-CD19 CAR-transduced cells at 37°C (C) or 4°C (D). The effects of CAR-staining reagents were compared by 2-way ANOVA and post-hoc *t*-tests, whereby ns denotes not significant, * denotes $p<0.05$, ** denotes $p<0.01$, *** denotes $p<0.001$, and **** denotes $p<0.0001$. Associated with Figures III-S6 and III-S7.

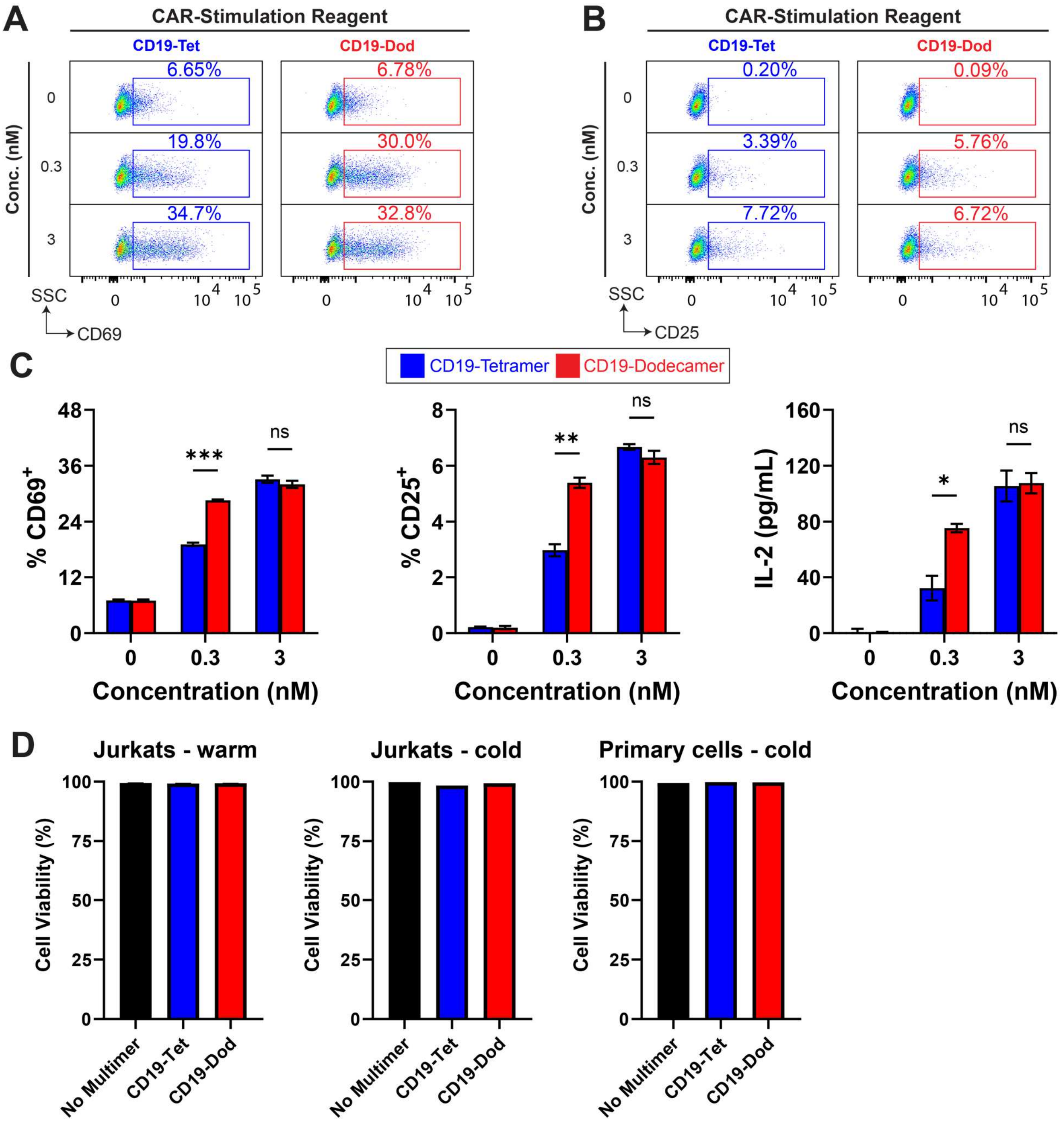

Figure III-S6. Antigen-multimer stimulation of 1st-gen CAR T cells. (A-B) Representative flow plots showing expression of CD69 (A) and CD25 (B) on 1st-generation anti-CD19 CAR cells in response to stimulation from CD19-tetramers or CD19-dodecamers at various concentrations at 37°C. (C) Bar graphs depicting CD69 expression (left), CD25 expression (middle), and IL-2 secretion (right) of triplicate data from stimulation of anti-CD19 CAR cells. For all bar graphs, stimulation of CAR cells was compared by 2-way ANOVA and post-hoc *t*-tests, whereby ns denotes not significant, * denotes $p<0.05$, ** denotes $p<0.01$, *** denotes $p<0.001$, and **** denotes $p<0.0001$. (D) Bar graph depicting influence of antigen-multimer stimulation/staining on cell viability in CAR-transduced Jurkat cells or primary patient CAR T cells. Associated with Figure III-6.

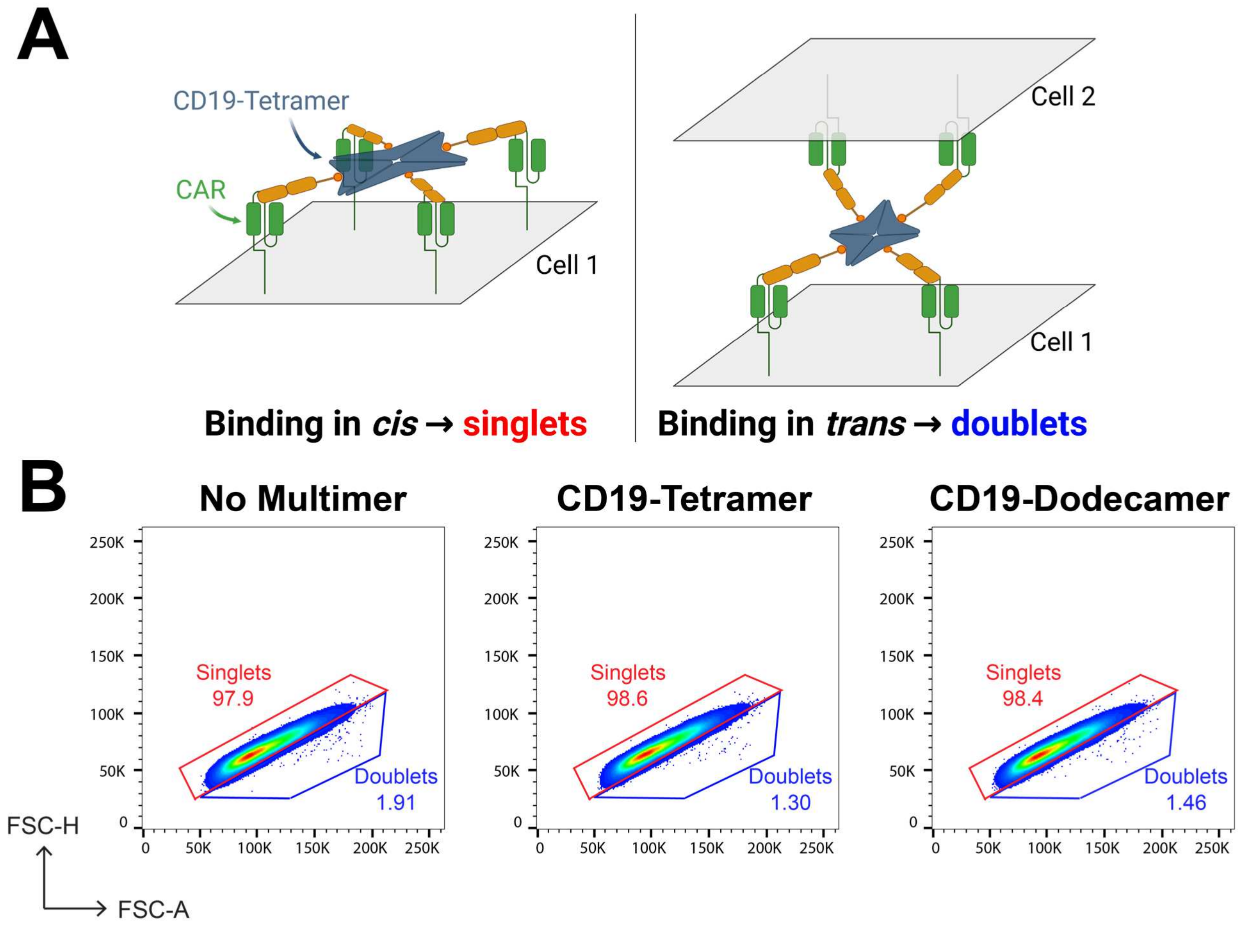

Figure III-S7. Antigen-multimer binding modalities for CAR stimulation. (A) In principle, antigen-multimers can bind CARs on the same cell (left) or bind CARs across different cells (right). The former will result in CAR T-cell singlets while the latter will result in CAR T-cell doublets. (B) CAR-transduced Jurkat T cells were incubated without multimers, with 10 nM CD19-tetramers, or with 10 nM CD19-dodecamers at 37°C. Doublets were quantified via flow cytometry. Associated with Figure III-6.

Antigen-multimers detect CAR T cells from patient biospecimens.

After demonstrating usage of antigen-multimers on CAR-transduced cell lines, we further applied CD19-multimers on clinical biospecimens from patients with diffuse large B-cell lymphoma or B-cell acute lymphoblastic leukemia who were treated with anti-CD19 CAR T-cell therapies. Over the course of therapy, CAR T cells originate from the infusion product, circulate through peripheral blood, and home to the tumor (**Figure III-7A**). Therefore, we tested CD19-multimers on infusion products, peripheral blood, and tumor biopsies.

First, we titrated CD19-multimers on axicabtagene ciloleucel and tisagenlecleucel infusion products. For both $CD4^+$ and $CD8^+$ T cells from either infusion product formulations, higher CD19-multimer concentrations stained more cells. On the other hand, CD19-multimers did not stain T cells from a healthy donor (figure III-S8A-B). At staining saturation, both CD19-tetramers and CD19-dodecamers detected equal percentages of CAR^+ cells across six patients (**Figure III-7B**). Next, we fitted the relative stained percentage of patient cells to dose-response curves to quantify staining EC_{50} values. Staining EC_{50} values for CD19-tetramers were consistently greater than those for CD19-dodecamers (**Figure III-7C**), which was consistent with previous findings on cell lines (**Figure III-2D**). In addition, staining EC_{50} values were equivalent between the two infusion products. Finally, staining EC_{50} values for $CD8^+$ CAR T cells were consistently greater than those for $CD4^+$ CAR T cells. $CD8^+$ CAR T cells may express fewer CAR molecules per cell, making these cells harder to capture at intermediate CD19-multimer concentrations.

Next, we applied CD19-tetramers upon a longitudinal set of post-infusion peripheral blood mononuclear cells from a patient treated with axicabtagene ciloleucel (**Figure III-7D**). Our data showed that CAR T-cell percentages rose and reached peak expansion within 8 days post-infusion. Subsequently, CAR T-cell percentages decreased, and were virtually undetectable at 60 days post-infusion (**Figure III-7E**). Most post-infusion CAR T cells expressed CD8. These observations match expected patterns of CAR T-cell expansion and contraction. As further validation, the anti-FMC63 antibody was used to quantify CAR T-cell percentages in the same biospecimens (figure III-S8C). Percentages from CD19-tetramers and the anti-FMC63 antibody were highly correlated (figure III-S8D). These findings suggest that CD19-tetramers accurately detected CAR T cells from patient biospecimens. Finally, we applied CD19-dodecamers upon a lymphoma tumor cell suspension from a patient treated with axicabtagene ciloleucel 14 days prior (**Figure III-7F**). CAR T cells represented 22% of leukocytes. 88% of CAR T cells were $CD8^+$ T cells, and 7% were $CD4^+$ T cells. A small population (2%) of apparent double positive $CD4^+CD8^+$ CAR T cells was also observed. Collectively, our results demonstrate that CD19-multimers can accurately capture both CD4$^+$ and CD8$^+$ CAR T cells from patient infusion products, post-infusion blood, and tumor biopsies.

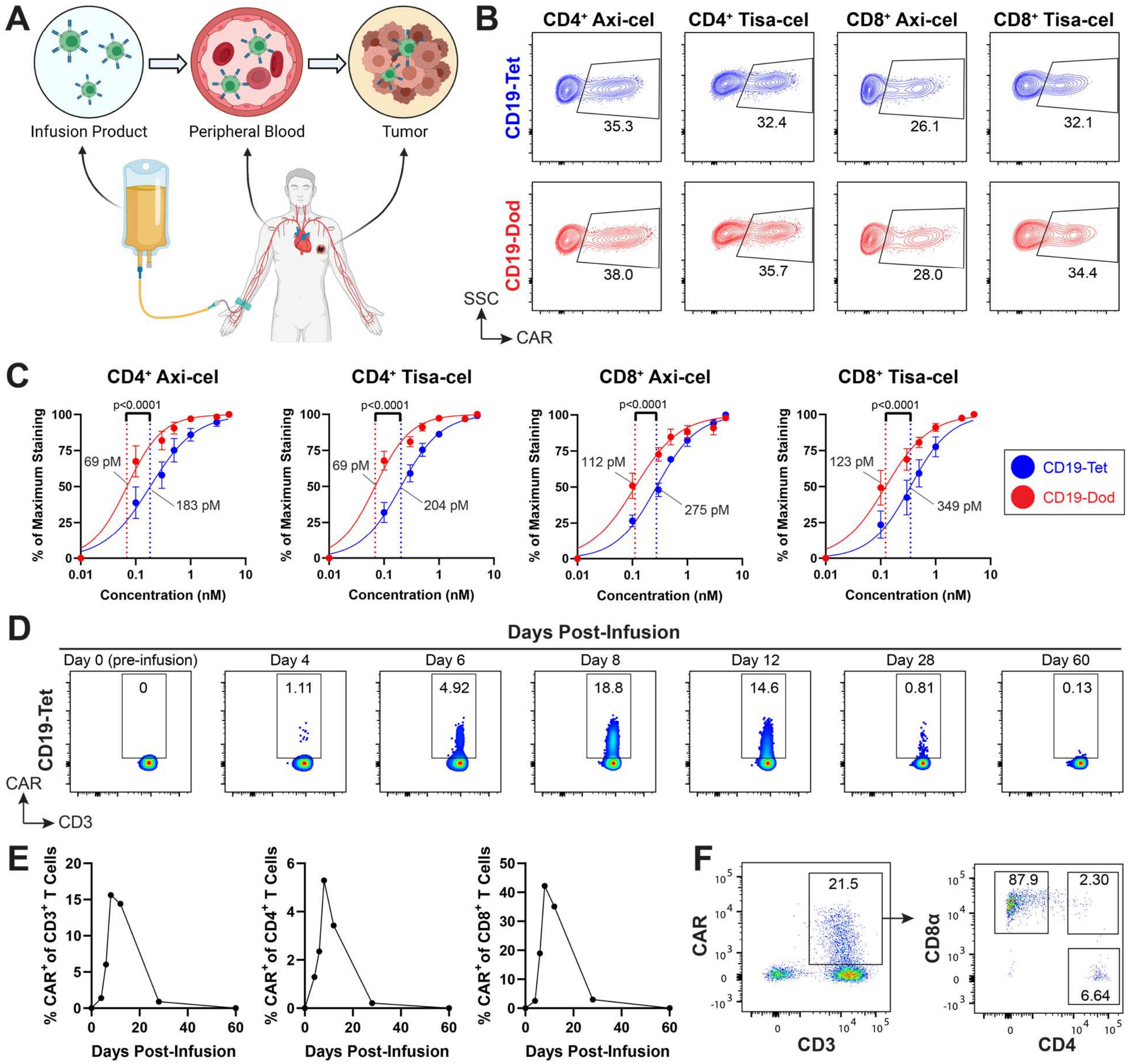

Figure III-7. Antigen-multimers detect CAR T cells from patient infusion product, peripheral blood, and tumor biopsies. (A) Diagram depicting the different patient biospecimens that may contain CAR T cells throughout their *ex vivo* and *in vivo* life cycle. CAR T cells are manufactured in the infusion product, circulate through peripheral blood, and home into the tumor. (B) Representative flow plots showing that CD19-tetramers (5 nM, blue, top row) and CD19-dodecamers (5 nM, red, bottom row) can detect both CD4$^+$ and CD8$^+$ CAR T cells from axicabtagene ciloleucel (axi-cel) and tisagenlecleucel (tisa-cel) infusion products. Flow plots are representative of six independent infusion products (3 axi-cel and 3 tisa-cel). Gates were drawn off CD19-multimer fluorescence-minus-one (FMO) controls.

Figure III-7, continued. (C) Relative percentage of maximum staining from infusion product titrations were fitted to dose-response curves. Since each infusion product contains a different prevalence of CAR T cells, percentage stained was normalized to that of maximum staining for each infusion product. For each concentration, the point displays mean ± standard error of the mean. The fitted staining EC_{50} values were compared with a sum-of-squares *F*-test. (D-E) Flow plots showing CD19-tetramer staining of a longitudinal set of peripheral blood samples from a patient with diffuse large B-cell lymphoma infused with an axi-cel infusion product. CAR T cells were analyzed for CD4 and CD8α expression. Expansion and contraction of CAR T cells are summarized in (E). (F) Staining of a dissociated lymphoma tumor biopsy from a patient treated with an axi-cel infusion product. $CD3^+CAR^+$ cells were analyzed for CD4 and CD8α expression. Associated with Figure III-S8.

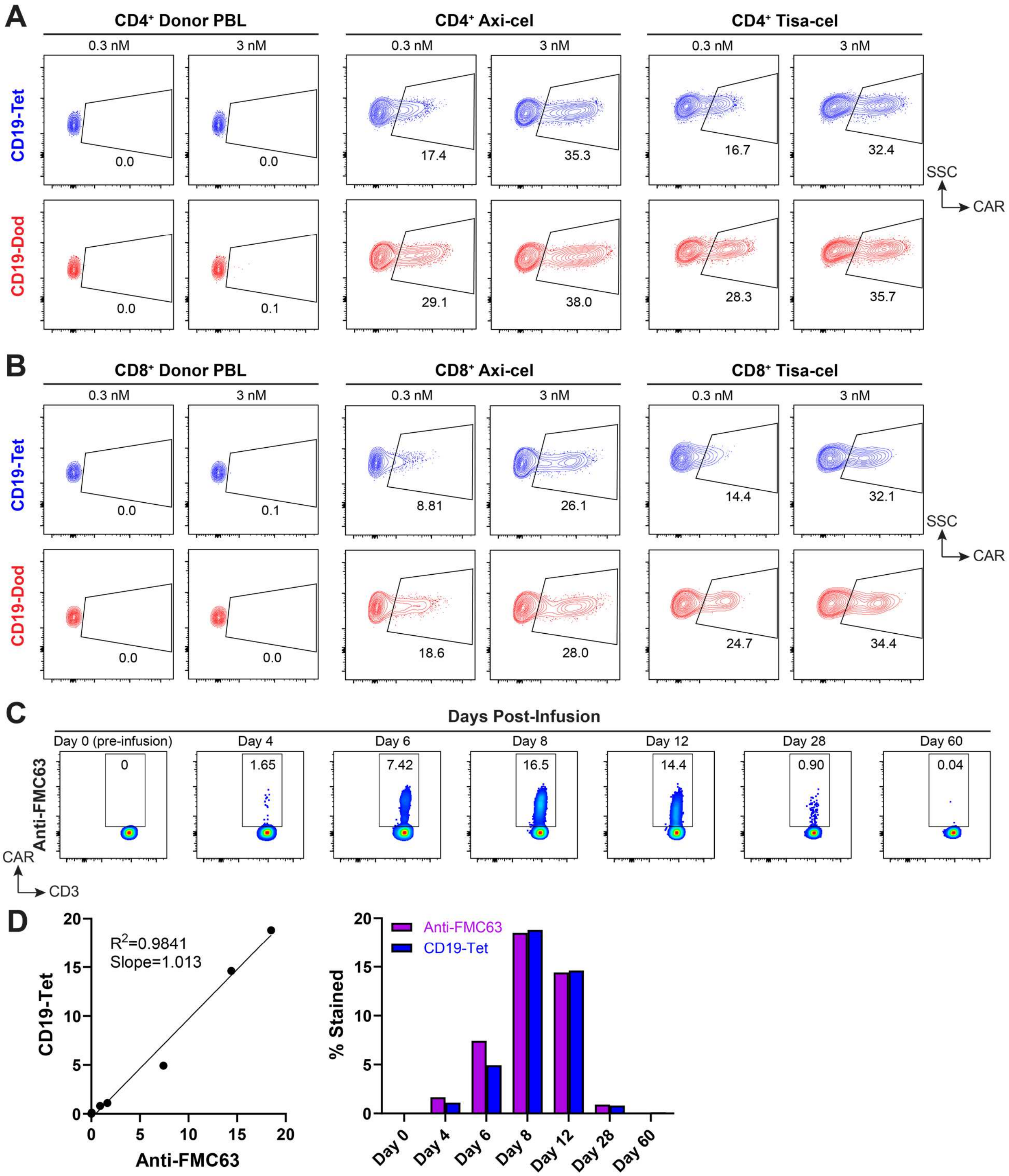

Figure III-S8. CD19-multimers staining of clinical biospecimens. (A-B) Flow plots depicting titrations of CD19-tetramers and CD19-dodecamers against CD4+ and CD8+ T cells from axicabtagene ciloleucel (axi-cel, middle) and tisagenlecleucel (tisa-cel, right) infusion products. Non-specific staining was measured with a biological control (donor PBL, left). All gates were set by a fluorescence-minus-one control.

Figure III-S8, continued. (C) Flow plots showing anti-idiotype antibody staining of a longitudinal set of peripheral blood samples from a patient infused with an axicabtagene ciloleucel infusion product. (D) Dot plot (left) and bar graph (right) comparing percentage of CD3$^+$ T cells that are CAR$^+$ as measured by CD19-tetramers or anti-idiotype antibody. Associated with Figure III-7.

Antigen-multimers isolate CAR T cells from a patient biospecimen for single-cell omics analyses.

Having established the utility of CD19-multimers for identifying CAR T cells from patient biospecimens, we subsequently applied CD19-tetramers for the isolation of anti-CD19 CAR T cells from a patient's post-infusion peripheral blood biospecimen for single-cell omics assays. The chosen sample was derived from a patient with diffuse large B-cell lymphoma who was treated with axicabtagene ciloleucel. The patient achieved clinical criteria for a complete response by day 30. The blood sample was taken at 21 days post-infusion.

At day 21, 10.7% of CD3$^+$ T cells were also CAR$^+$ by CD19-tetramer staining (**Figure III-8A**). Using CD19-tetramers, CAR$^+$ T cells ("CAR-T") and endogenous CAR$^-$ T cells ("Endo-T") were isolated by FACS for analysis by paired single-cell RNA- and TCR-sequencing. Single-cell RNA-sequencing demonstrated that expression of the axicabtagene ciloleucel CAR transgene was highly specific to CAR-T cells (**Figure III-8B** and figure III-S9A-B). This observation was consistent with the high specificity, sensitivity, and precision of the CD19-tetramer, and suggested that antigen-multimers can sort a highly pure and true CAR T-cell population from patient biospecimens. Moreover, although multiple diverse T-cell receptor (TCR) clonotypes were discovered in both CAR-T and Endo-T cells, there was minimal TCR clonotype overlap (≤1%) between the populations (**Figure III-8C** and figure III-S9H). Altogether, our results show that CD19-tetramers captured a clonally distinct population of CAR transgene-expressing T cells from the patient biospecimen.

Through uniform manifold approximation and projection (UMAP) and unsupervised Louvain clustering, we identified twelve T-cell clusters based on known markers (including *FOXP3*, *CCR7*, *TCF7*, *GZMB*, *KLRB1*, and *TRDC*), including proliferating, effector CD8$^+$, cytotoxic CD4$^+$, central memory, effector memory, γδ, and regulatory T cells, after filtering out 3 non-T-cell clusters (**Figure III-8D** and figure III-S9C-F). Relative to Endo-T cells, CAR-T cells were enriched for CD8$^+$ T cells (figure III-S9G). Furthermore, CAR-T cells were enriched in proliferating and effector T-cell clusters, while Endo-T cells were enriched in memory and regulatory T-cell clusters (**Figure III-8E**). Notably, CAR-T cells were discovered within both the γδ and regulatory T-cell clusters. Differential gene analysis revealed that CAR-T cells have higher expression of activation genes (*CXCR3*, *LAG3*, *HAVCR2*), cytotoxicity-associated genes (*GNLY*, *KLRD1*, *GZMB*, *PRF1*, *GZMA*), and a T cell senescence-associated gene (*KLRG1*) (**Figure III-8F**). These signatures are consistent with CAR-specific T-cell activation, cytotoxicity, and differentiation. Altogether, these observations are consistent with CD19-tetramers capturing a distinct and clinically active T-cell population from the patient biospecimen. These experiments demonstrate that antigen-multimers can be reliably used for CAR T-cell isolation and profiling.

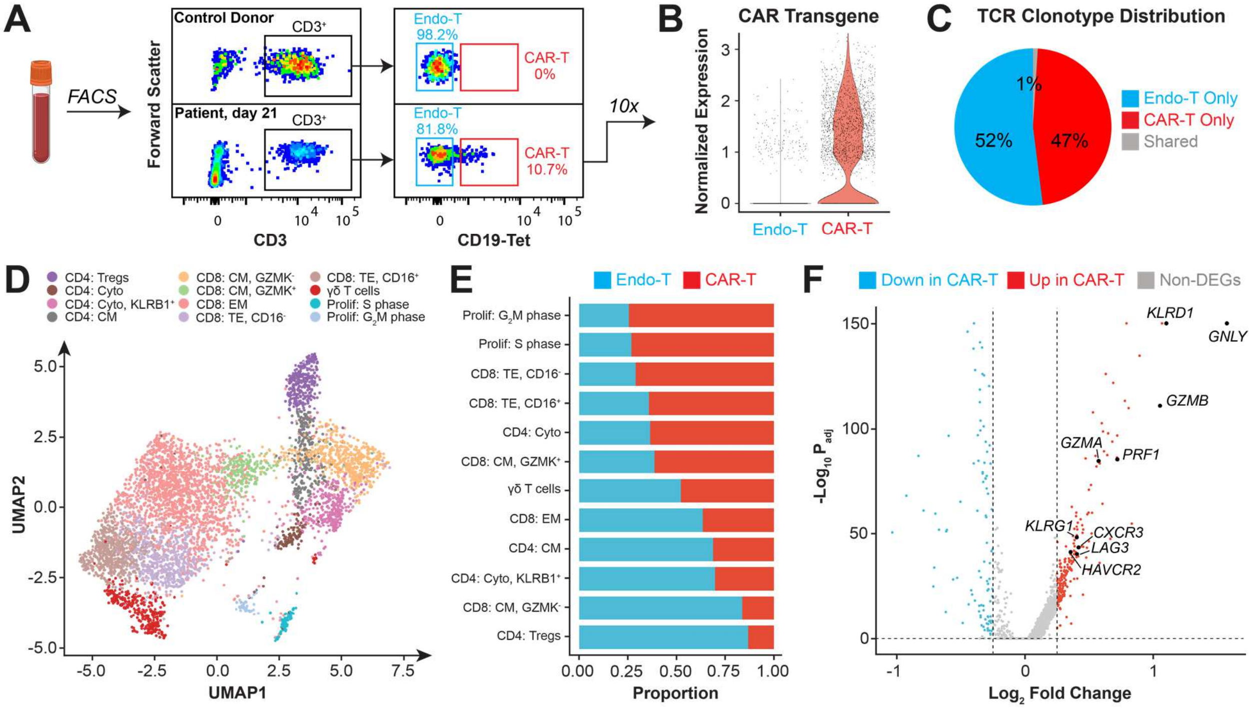

Figure III-8. Antigen-multimers isolate CAR T cells from a patient biospecimen for single-cell omics analyses.

Figure III-8, continued. (A) Flow plots demonstrating use of CD19-tetramers (3 nM) for CAR T-cell sorting and single-cell, omics assays. After gating for CD3$^+$ T cells, PBMCs from a healthy donor (biological control) were used to draw CAR$^-$ and CAR$^+$ gates. Gates were used to sort for endogenous CAR$^-$ T cells (Endo-T) and therapeutic CAR$^+$ T cells (CAR-T) from a patient biospecimen. Sorted Endo-T and CAR-T cells were used for single-cell omics (RNA-seq and TCR-seq). (B) Violin plot depicting normalized CAR transgene mRNA expression in Endo-T and CAR-T samples. (C) Pie chart depicting distribution of TCR clonotypes between Endo-T and CAR-T cells. (D) Single-cell data from Endo-T and CAR-T were combined and visualized by UMAP and unsupervised Louvain clustering. Twelve T-cell clusters were annotated based on known markers. (E) Stacked bar graph depicting proportions of Endo-T and CAR-T cells represented in each T-cell cluster. (F) Volcano plot depicting differentially expressed genes (DEGs) between Endo-T and CAR-T cells, with a cut-off based on $\log_2$ fold-change. DEGs of interest are labeled. Abbreviations: cyto, cytotoxic; CM, central memory; EM, effector memory; TE, terminal effector. Associated with Figure III-S9.

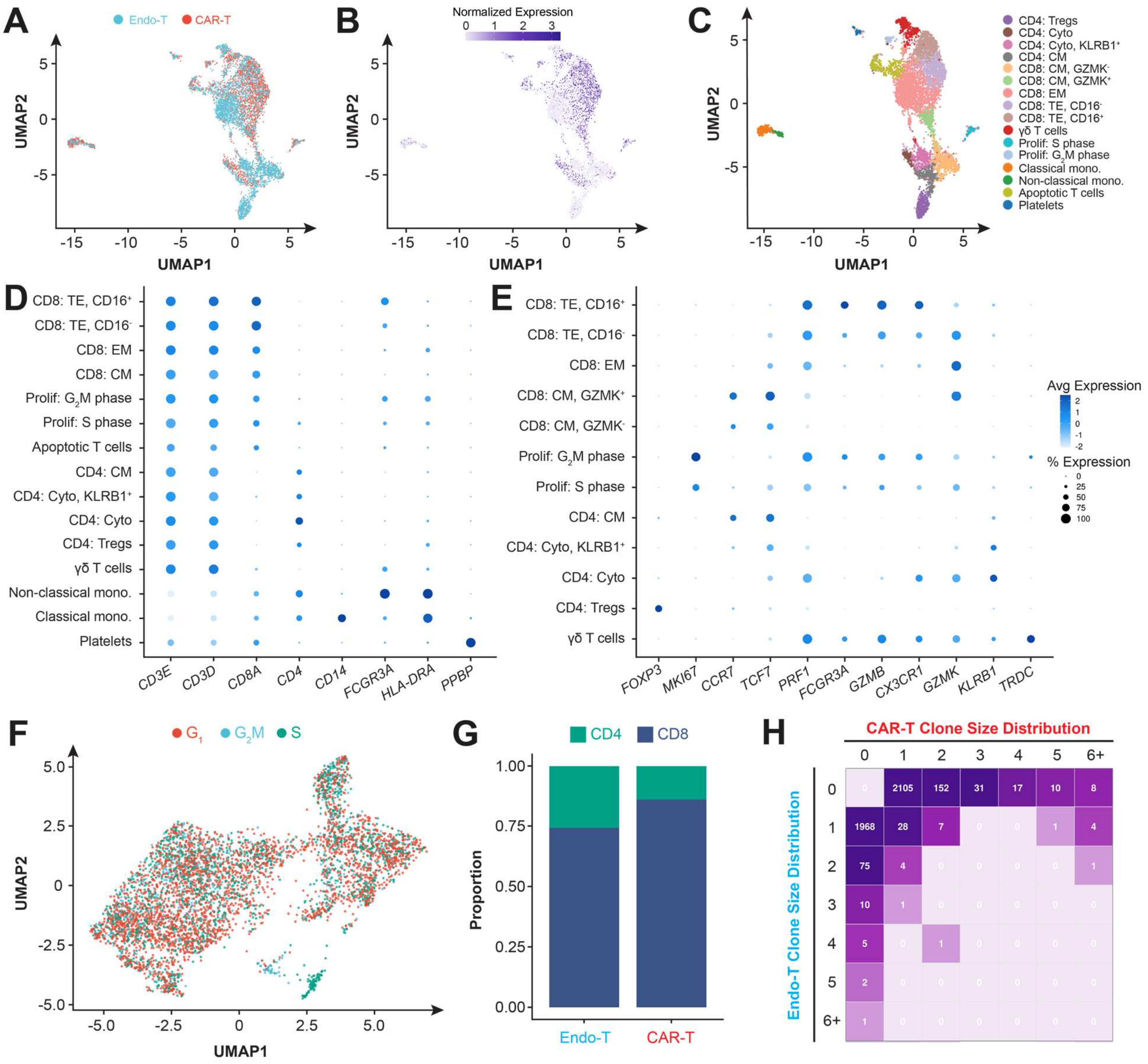

Figure III-S9. CAR transgene distribution, cell cluster annotation, and TCR clone size distribution of single-cell omics data. (A) UMAP depicting the sample origin of each cell in the single-cell dataset. (B) UMAP depicting normalized expression of the CAR transgene in each cell. (C) UMAP depicting all sixteen T cell and non-T cell clusters. (D) Dot plot depicting expression of key genes used to annotate T cell and non-T cell clusters. (E) Dot plot depicting expression of key genes used to annotate T-cell subsets. (F) UMAP depicting computational cell cycle analysis of cells. (G) Stacked bar graph depicting CD4$^+$ versus CD8$^+$ T-cell distribution within Endo-T and CAR-T samples. (H) Heatmap showing TCR clone size distributions in Endo-T and CAR-T samples. Most TCR clones are specific to CAR-T (top row) or Endo-T (left column) samples. Remaining TCR clones were discovered in both samples, and are plotted according to their clone sizes in CAR-T and Endo-T samples. Associated with Figure III-8.

III: Discussion

With our goal of generating an extensible and universal high-avidity CAR-staining reagent, we have designed, constructed, tested, and validated antigen-multimers. Through staining titrations and spike-in experiments, we showed that antigen-multimers detect CARs with high specificity, sensitivity, and precision, even when target cells had low CAR expression. In addition to CAR detection, we demonstrated that antigen-multimers enable magnetic enrichment of CAR T cells for rare populations, temperature-controlled CAR T-cell stimulation for activation phenotyping, and high-purity CAR T-cell sorting for high-dimensional CAR T-cell profiling by single-cell multi-omics analyses. For clinical and translational applications, we demonstrated that CD19-multimers can identify CAR T cells in infusion products, peripheral blood samples, and tumor biopsies from patients undergoing CD19-directed CAR T-cell therapy. Finally, through staining titrations from three independent CAR systems (anti-CD19, anti-HER2, and anti-Tn), we demonstrated that antigen-multimers are readily extensible to existing and new CAR systems.

Antigen-multimers offer critical advantages over existing CAR-staining reagents.[119] Relative to monomeric antigen ligand, polyclonal anti-IgG antibodies, and Protein L, antigen-multimers exhibited greater specificity, sensitivity, and precision during CAR-detection. In particular, antigen-multimers demonstrated consistent performance between different CARs, as well as high sensitivity and precision for detecting low-frequency CAR T cells with low CAR expression. This is a critical advantage since CAR T cells downmodulate CAR expression *in vivo* after antigen-engagement.[28,56,129] In contrast, anti-IgG antibodies and Protein L showed inconsistent performance between different CARs and may not even detect CAR T cells with low CAR expression. Furthermore, unlike with antigen-multimers, neither anti-IgG antibodies nor Protein L can stain CAR T cells concurrently with exogenous antibodies, which significantly restricts their utility for multiparameter flow cytometry. Compared to monomeric antigen ligand, antigen-multimers stained with more fluorescence at saturation. Notably, only antigen-multimers, but not monomers, can stain the low-affinity anti-Tn CAR at reasonable concentrations. Finally, for the detection of CAR T cells with low CAR expression, CD19-multimers exhibited greater sensitivity than monomeric CD19 while simultaneously reducing the number of staining steps. These observations regarding antigen-multimers' critical advantages can be explained by multivalent interactions between antigen-multimers and CARs. Multivalent interactions can significantly decrease the multimer dissociation rate and increase the multimer residence time on the CARs. Therefore, in addition to increasing staining fluorescence, multivalent interactions are expected to increase the stability of the fluorescence signal over time, leading to more reproducible CAR-detection.

Importantly, CD19-multimers caused greater fluorescence at saturation than an anti-FMC63 anti-idiotype antibody, which is considered the gold standard for CAR-detection. Furthermore, unlike with antigen-multimers, anti-idiotype antibodies are fundamentally restricted to particular antibody clones. For instance, the anti-FMC63 anti-idiotype antibody can stain FMC63-based CARs, but not newer anti-CD19 CARs, including the Hu19-CAR engineered with fully human scFv domains, and the CAT-CAR engineered for lowered binding affinity.[125,128] Moreover, since monoclonal antibodies can be time-consuming or expensive to develop, anti-idiotype antibodies may not be scalable or sustainable to keep pace with the fast research progress in the CAR field. On the other hand, antigen-multimers are not restricted to particular clones, and can be readily generalized for use in existing and new CAR systems.

In addition to CAR-detection, antigen-multimers enable magnetic enrichment of CAR T cells, which is expected to facilitate the detection and investigation of rare CAR T-cell subsets. Historically, magnetic enrichment made it possible to investigate rare naïve T cells of a given antigen-specificity by achieving 50-100-fold enrichment.[121] In our study, CAR T cells were enriched by >100-fold with either antigen-tetramers or antigen-dodecamers. Since our enrichments were performed on CAR T cells with low CAR expression, the potential benefits of antigen-multimers for magnetic enrichment may be even higher in real-world scenarios. This increase in sensitivity through enrichment may facilitate studies on rarer CAR T-cell subsets, such as persistent memory CAR T cells which are correlated with durable responses in patients.[130] In addition, CAR T-cell enrichment can be critical for manufacturing CAR T-cell infusion products. During infusion product manufacturing, if CAR transgene delivery efficiency is low, there may be relatively fewer CAR T cells available for therapy. This may be a particular problem with non-viral transgene delivery methods (e.g. through transposons or CRISPR-Cas9), which are less efficient than retroviral methods.[37,137] Even if adequate CAR T cell numbers are reached through longer *ex vivo* expansion, the resulting cells may have progressed towards a terminally differentiated effector phenotype, which reduces therapy efficacy.[138] CAR T-cell enrichment may potentially salvage inefficient CAR transgene delivery.

In addition to serving as CAR-staining reagents at 4°C, antigen-multimers can also specifically stimulate CAR T cells at 37°C. This helps to characterize a CAR T cell's activation phenotype, which is associated with *in vivo* CAR T-cell efficacy.[23,133] Unlike generic T-cell mitogens (neither CAR-specific nor mimic biologically relevant CAR stimulation) or plates pre-coated with CAR-stimulating reagents[56,134,135], antigen-multimers directly stimulate CAR T cells through its antigen ligand in soluble form. Our data suggests that stimulation through antigen-multimers likely occurs through CAR oligomerization. We further anticipate that antigen-multimers may be useful in stimulating CAR T cells during *ex vivo* production and expansion. *Ex vivo* CAR stimulation would also enrich lymphocytes for CAR T cells in lieu of positive selection for CAR$^+$ cells. Currently, this process is performed by adding irradiated antigen-positive feeder cells.[139] However, antigen-positive feeder cells may adversely influence CAR T-cell phenotype. Feeder cells may also risk introducing unwanted ligands or proliferation-competent cells through incomplete irradiation. Controlled, chemically-defined antigen-multimers may circumvent these limitations.

Finally, for clinical and translational applications, we demonstrated that CD19-multimers can identify CAR T cells from multiple patient biospecimen sources, including infusion products, peripheral blood samples, and tumor biopsies. We then employed single-cell omics to highdimensionally profile CD19-tetramer-sorted adoptively transferred CAR^+ T cells and endogenous CAR^- T cells from a CAR T-cell therapy patient's post-infusion blood sample. Analysis of CAR transgene expression, TCR clonotype usage, and transcriptomic patterns between CAR^- and CAR^+ cells revealed that CD19-tetramers captured a pure, distinct, and clinically-active CAR T-cell population. Since multi-omics profiling has become increasingly utilized on CAR T-cell patient biospecimens to interrogate clinically-relevant CAR T-cell phenotypes[22,39,140], we expect antigen-multimers to be broadly applicable for translational researchers and cell therapists involved in CAR research.

Two types of antigen-multimers were engineered in our study: tetramers and dodecamers. Our staining titrations showed that dodecamers required lower concentrations to saturate CAR staining than the corresponding tetramers did. These findings indicate that target antigen avidity influences the interaction of a given antigen-multimer for its matched CAR. In general, dodecamers stained with greater fluorescence than tetramers. However, in our titrations, the two multimers were equally proficient at capturing almost all CAR-expressing cell lines at saturating concentrations. Since antigen-multimers would be expected to be used at saturating concentrations in real-world scenarios, the benefits of using dodecamers over tetramers are modest. Since streptavidin is commercially available, tetramers are also easier to construct. On the other hand, dodecamers may be ideal for use when the staining reagent is paired with a dim fluorophore or when the CAR's affinity for target antigen is low. Although we specifically tested tetramers and dodecamers, antigen-multimers of additional valencies (such as dimers, pentamers, octamers, or dextramers) could be generated.[121] These alternative binding valencies may offer differential advantages for CAR-detection by modulating binding avidity.

Despite their numerous advantages, antigen-multimers are associated with three important limitations. Firstly, antigen-multimers are dependent on the accessibility and stability of the biotinylated antigen ligand. Eukaryotic proteins can sometimes be difficult to express or site-specifically biotinylate. Secondly, antigen-multimers should not be used with an antibody that also binds to the antigen ligand at an overlapped epitope. Thirdly, it is possible that preparation of the streptavidin-based scaffold for antigen-dodecamers results in spurious heterogeneous and higher-order oligomeric forms. To reduce these side reactions, the concentrations of the biotinylated dodecamer scaffold protein and streptavidin during the incubation can be modified to control the frequency of molecular collisions and decrease higher-order oligomerization.

In conclusion, we have developed antigen-multimers as extensible and multifunctional high-avidity CAR T-cell detection, enrichment, and stimulation reagents. We anticipate that antigen-multimers will be a versatile tool to probe CAR T cells for clinical and research applications.

IV: Methods

Lentiviral production and transduction.

Plasmids carrying a human CAR or mCherry were cloned onto the pHR vector backbone.[93] Plasmids carrying a mouse CAR were cloned onto the pMP71 vector backbone. Transfer plasmids were transfected into the Lenti-X 293T packaging cell line (Takara, 632180) or Platinum-E retroviral packaging cell line (Cell Biolabs, RV-101) for lentiviral or ecotropic retroviral production. Both packaging cell lines were routinely cultured in DMEM and 10% fetal bovine serum (X&Y Cell Culture, FBS-500).

In brief, packaging cells were grown overnight and transfected the following day via Lipofectamine 3000 (Invitrogen, L3000001). For lentiviral production, transfer plasmids (0.95 µg, containing the CAR on the pHR vector backbone), packaging plasmids (0.72 µg, psPAX2), and envelope plasmids (0.22 µg, pMD2.G) were co-transfected into Lenti-X 293T cells. For ecotropic retroviral production, transfer plasmid (0.95 µg, containing the CAR on the pMP71 vector backbone) was transfected into Platinum-E cells. After 72 hours, the viral supernatant was concentrated by ultracentrifugation and stored at -80°C until transduction.

Concentrated lentiviruses were used to transduce E6-1 Jurkat cells and $58^{-/-}$ mouse hybridoma cells. E6-1 Jurkat cells and $58^{-/-}$ mouse hybridoma cells were routinely cultured in RPMI-1640 (Gibco, 11875093) or DMEM media respectively, supplemented with 10% fetal bovine serum (X&Y Cell Culture, FBS-500). During transduction, lentiviruses or ecotropic retroviruses were added to cells along with protamine sulfate (Millipore Sigma, P3369-10G) to a final concentration of 10 µg/mL. Cells were spinoculated at 800 x *g* for 60 minutes at room temperature. Then, cells were grown for 72 hours before analysis of transduction efficiency by flow cytometry. Untransduced cells were used for gating.

Preparation of anti-CD19 CAR-transduced Jurkat clones.

$meGFP^+$ Jurkat cell clones with stably low anti-CD19 CAR expression and $mCherry^+$ Jurkat cell clones with no CAR expression were used for (1) spike-in experiments to assay CAR-staining reagents for sensitivity and precision, and (2) magnetic enrichment experiments. To prepare these clones, a polyclonal lentivirally-transduced Jurkat cell population was single-cell sorted into 96-well plates. For preparation of $meGFP^+$ Jurkat cell clones, cells with lower meGFP fluorescence were chosen for the sort. For preparation of the $mCherry^+$ Jurkat cell clone, cells with median mCherry fluorescence were chosen for the sort. After culturing for 1 month, ~10% of sorted single cells grew to high cell density. Cells were successively transferred to larger media volumes.

meGFP or mCherry expression in each clone was analyzed by flow cytometry, and compared to that of the pre-sorted polyclonal population. To quantify the average number of CAR molecules per cell in the anti-CD19 CAR-transduced Jurkat clones, we used GFP flow cytometer calibration beads (Takara, 632594), because GFP is fused to the C-terminus of the CAR. Two $meGFP^+$ clones (named “low clone” and “mid clone”) were found to have lower CAR expression than the pre-sorted polyclonal population. One $mCherry^+$ clone was chosen for having median-level mCherry expression as the pre-sorted polyclonal population. In both CAR-expressing clones, CAR expression was stable and remained similarly low after extensive culturing (>1 month).

Before each experiment, CAR expression in these clones was checked to confirm the clones' integrity.

Purification of dodecamer base protein.

The dodecamer base protein is a tetramer of an inactive streptavidin subunit mutagenized with an added C-terminal cysteine. The protein was expressed in BL21 *Escherichia coli* and refolded to form a tetramer with four cysteines. This tetramer was first purified by fast protein liquid chromatography using a Superdex 75x10/300 GL column (GE Healthcare, 17517401). Then, the four cysteines on the purified tetramer were reduced with tris(2-carboxyethyl)phosphine, and biotinylated overnight at room temperature using maleimide chemistry with an extended linker by EZ-Link BMCC Biotin (Thermo Scientific, 21900) at ≥50:1 molar ratio. Subsequently, the reaction mixture containing biotinylated base protein was desalted twice into HBSS buffer using 7K MWCO Zeba Spin Desalting Columns (Thermo Scientific, 89882). The biotinylation efficiency and concentration of the final base protein were assayed by the Pierce Fluorescence Biotin Quantitation Kit (Thermo Scientific, S20033) and the Qubit Protein Assay Kit (Invitrogen, Q33211) respectively.

Generation of antigen-multimers.

Multimers were constructed from AviTag-biotinylated human His-tagged CD19 (Acro Biosystems, CD9-H82E9), AviTag-biotinylated human His-tagged HER2 (Acro Biosystems, HE2-H82E2), site-specifically biotinylated Tn-glycosylated podoplanin G(T*)KPPLEE peptide (glycosylation marked with *)[141], and biotinylated bovine serum albumin (BioVision, 7097-5). Biotinylated dodecamer base protein and either Alexa Fluor 647-labeled streptavidin (BioLegend, 405237) or allophycocyanin-labeled streptavidin (BioLegend, 405207) were used for the multimer scaffold.

To generate antigen-tetramers, biotinylated antigen ligand was added to fluorescently-labeled tetrameric streptavidin at a 4:1 molar ratio for 30 minutes at 4°C in the dark. This mixture was diluted with PBS to convenient concentrations for staining.

To generate antigen-dodecamers, biotinylated tetrameric dodecamer base protein was incubated with fluorescently-labeled tetrameric streptavidin at a 1:4 molar ratio for 30 minutes at 4°C in the dark. Subsequently, biotinylated antigen ligand was added at a 12:1 molar ratio for an additional 30 minutes at 4°C in the dark. This mixture was diluted with PBS to convenient concentrations for staining.

CAR-staining assays for cell lines.

For staining assays with cell lines, 50000 live cells were employed for all conditions. Cells were first washed with cold FACS buffer (PBS, 2% BSA, 0.05% sodium azide). Then, cells were incubated with CAR-staining reagents as follows:

For staining with antigen-multimers, cells were incubated for 30 minutes at 4°C in the dark with a staining solution containing AF647-labeled antigen-tetramers or antigen-dodecamers at chosen concentrations.

For staining with polyclonal anti-IgG, cells were incubated for 30 minutes at 4°C in the dark with a staining solution containing AF647-labeled anti-mouse IgG (H+L) cross-adsorbed F(ab')2-Goat (Fisher Scientific, A21237) at 5 µg per 100 µL staining volume (optimal concentration determined by pre-titrating cell lines).

For staining with Protein L, cells were incubated for 30 minutes at 4°C in the dark with a staining solution containing biotinylated Protein L (Thermo Fisher Scientific, 29997) at 1 µg per 100 µL volume according to specifications from the literature.[67] Cells were subsequently incubated with 1 ng/µL AF647-streptavidin (BioLegend, 405237) in FACS buffer for 20 minutes.

For staining with anti-FMC63, cells were incubated for 30 minutes at 4°C in the dark with a staining solution containing biotinylated anti-FMC63 (clone Y45, Acro Biosystems, FM3-BY45) at chosen concentrations. Cells were subsequently incubated with 1 ng/µL AF647-streptavidin (BioLegend, 405237) in FACS buffer for 20 minutes.

For staining with monomeric target antigen, cells were incubated for 30 minutes at 4°C in the dark with a staining solution containing biotinylated target antigen at chosen concentrations. Cells were subsequently incubated with 1 ng/µL AF647-streptavidin (BioLegend, 405237) in FACS buffer for 20 minutes.

For all CAR-staining assays, after staining with CAR-staining reagents, cells were incubated with LIVE/DEAD Fixable Near-IR viability dye (Invitrogen, L34975) diluted 1:1000 in PBS for 5 minutes at room temperature. Finally, cells were washed three times in FACS buffer at 4°C before analysis by flow cytometry.

CAR-staining assays for patient biospecimens.

Cryopreserved patient biospecimens were thawed in warm RPMI+10% FBS. Cells were first washed with cold FACS buffer (PBS, 2% BSA, 0.05% sodium azide). Next, Fc receptors were blocked by incubation with Human TruStain FcX (BioLegend, 422301) at 1:50 dilution for 5 minutes at 4°C. Then, cells were incubated for 30 minutes at 4°C in the dark with a staining solution containing BV421-anti-CD3ε (clone SK7, BioLegend, 344833), PE-anti-CD4 (clone SK3, BioLegend, 344605), AF488-anti-CD8α (clone Hit8a, BioLegend, 300916), and either antigen-multimers or biotinylated anti-FMC63 (clone Y45, Acro Biosystems, FM3-BY45). For staining with biotinylated anti-FMC63, cells were subsequently incubated with 1 ng/µL AF647-streptavidin (BioLegend, 405237) in FACS buffer for 20 minutes. Monoclonal antibodies were generally used according to manufacturer recommendations.

After staining, cells were incubated briefly with LIVE/DEAD Fixable Near-IR viability dye (Invitrogen, L34975) diluted 1:1000 in PBS for 5 minutes at room temperature. Then, cells were three times in FACS buffer at 4°C before analysis by flow cytometry.

Antigen-multimers for magnetic enrichment.

CAR-meGFP-transduced Jurkat cell clones with stably low CAR expression (“low clone” and “mid clone”) were spiked into mCherry-transduced non-CAR Jurkat cell at ~0.2% prevalence. Subsequently, cells were stained with 3 nM of allophycocyanin (APC)-labeled CD19-tetramers or CD19-dodecamers for 1 hour at 4°C in FACS buffer (PBS, 2% BSA, 0.05% sodium azide). Stained cells were washed three times and then incubated with anti-APC microbeads (Miltenyi Biotec, 130-090-855) at 1:5 dilution for 15 minutes at 4°C. Cells were then washed once with FACS buffer and applied onto magnetic columns (Miltenyi Biotec, 130-042-201). Columns were washed with three column volumes of FACS buffer. Then, the column was removed from the magnet, and cells were eluted under pressure from a plunger. Subsequently, cells were centrifuged and incubated briefly with LIVE/DEAD Fixable Near-IR viability dye (Invitrogen, L34975) diluted 1:1000 in PBS for 5 minutes at room temperature. Finally, cells were washed once in FACS buffer at 4°C before analysis by flow cytometry.

CAR T-cell stimulation assays.

CAR-transduced Jurkat cells were incubated in T-cell media (RPMI supplemented with 10% FBS, 1% Pen/Strep, 2 mM L-glutamine, 50 mM 2-mercaptoethanol) with antigen-multimers or anti-idiotype antibodies. After 24 hours at 37°C or 4°C, cells and supernatants were collected for the analyses of activation markers and cytokine production respectively.

To measure T-cell activation markers, the cells were washed with FACS buffer (PBS, 2% BSA, 0.05% sodium azide) and incubated for 30 minutes at 4°C in the dark with a staining solution containing APC-anti-CD25 (clone M-A251, BioLegend, 356110) and BV510-anti-CD69 (clone FN90, BioLegend, 310936). Subsequently, cells were incubated with LIVE/DEAD Fixable Near-IR viability dye (Invitrogen, L34975) diluted 1:1000 in PBS for 5 minutes at room temperature. Finally, cells were washed three times in cold FACS buffer before analysis by flow cytometry.

The supernatant was diluted 1:2 in PBS and analyzed for IL-2 secretion by an enzyme-linked immunosorbent assay (IL-2 Quantikine ELISA Kit, R&D Systems, D2050). For each ELISA, an 8-point standard curve was generated ($R^2 > 99\%$).

Single-cell omics assays.

Patient peripheral blood mononuclear cells were collected from blood biospecimens by Ficoll-Paque PLUS (Cytiva, 95021-205), and cryopreserved (RPMI supplemented with 10% FBS and 10% DMSO) in liquid nitrogen until analyses.

Cryopreserved patient biospecimens were thawed in warm RPMI+10% FBS. Cells were first washed with cold FACS buffer (PBS, 2% BSA, 0.05% sodium azide). Next, Fc receptors were blocked by incubation with Human TruStain FcX (BioLegend, 422301) at 1:50 dilution for 5 minutes at 4°C. Then, cells were incubated for 30 minutes at 4°C in the dark with a staining solution containing BV421-anti-CD3ε (clone SK7) and Alexa Fluor 647-labeled antigen-tetramers at 3 nM final concentration for CAR-detection. Subsequently, cells were incubated with LIVE/DEAD Fixable Near-IR viability dye (Invitrogen, L34975) diluted 1:1000 in PBS for 5 minutes at room temperature. Finally, cells were washed three times in cold cell media before fluorescence-activated cell sorting. To draw sorting gates based on a biological control, cells from a healthy donor were similar stained and analyzed

12000 sorted endogenous CAR^- T cells and 7853 sorted CAR^+ T cells were separately partitioned into droplets for single-cell omics assays via Chromium Next GEM Single-Cell 5'Kit v2 (10x Genomics, 1000263). From the resulting barcoded nucleic acids, TCR-seq libraries were prepared via the Chromium Single-Cell Human TCR Amplification Kit (10x Genomics, 1000252). Sequencing libraries were quantified via the Qubit dsDNA HS Assay Kit (Invitrogen, Q32851), quality-checked for fragment sizes via a high-sensitivity D5000 screentape (Agilent, 5067-5592), pooled, and sequenced (Illumina, NovaSeq-6000).

UMAP analysis and clustering on single-cell RNA-seq data.

UMAP analysis and clustering were performed using the Seurat package (Version 4.0.0).[142] Raw count matrices from $CD3^+CAR^+$ T cells ("CAR-T") and $CD3^+CAR^-$ endogenous T cells ("Endo-T") were first converted to Seurat objects before being further merged into one Seurat object. Following that, cells with less than 200 genes detected or greater than 25% mitochondrial RNA content were excluded from further analysis, with 5,875 retained after filtering. Since 19,853 cells were used to generate the data, our cell capture efficiency was 30%.

Then, the raw count was log-normalized using the NormalizeData function with default options. Top 5,000 variable features were then identified using the FindVariableFeatures function with the default "vst" method. The data were then centered and scaled using the ScaleData function, with additional regression against the percent of mitochondrial RNA content. Scaled data were then used as input for principal component analysis (PCA) based on variable genes using the RunPCA function. Data harmonization was then performed on the principal components using the Harmony package[143] through the RunHarmony function. UMAP was then constructed based on the first 50 harmony components, with "n.neighbors=30" and "min.dist=0.3". The same harmony components were then used to construct the shared nearest neighbor (SNN) graph using the FindNeighbors function, which was then partitioned to identify clusters using the FindClusters function with default Louvain algorithm and "resolution =0.8". These clusters were then manually aggregated and classified as T cell subsets based on known markers. The non-T clusters (626 cells) were then removed from following analyses, and the T cells (5,249 cells) were then re-analyzed separately with the same steps as above starting from renormalization.

Differential gene expression (DEG) analysis on single-cell RNA-seq data.

DEG analyses were all performed using the FindMarkers function in Seurat (Version 4.0.0) package, with default parameters and the appropriate 'ident.1" and "ident.2" set as contrast.

Unless otherwise stated, the results were then filtered with p_val_adj < 0.05 and abs(avg_logFC) > 0.25.

Single-cell TCR-seq data processing and analysis.

The scTCR-seq reads were aligned to the 10x curated GRCh38 vdj reference genome and quantified using the cellranger vdj (10x Genomics, version 6.0.0). The resultant clonotype and filtered contig annotation data were used for downstream analyses. The clonotype and contig data were then added to the scRNA data by matching the cell barcodes. The frequency of each clonotype in each sample was recalculated based on those successfully matched to the corresponding scRNA data. Each unique clonotype is defined by the nucleotide sequence of CDR3 regions for a productive TCRα chain paired with a productive TCRβ chain.

CAR transgene mapping.

The axicabtagene ciloleucel CAR design is documented.[65] Its sequence was confirmed by Sanger sequencing of genomic DNA extracted from axicabtagene ciloleucel infusion products. The CAR sequence was then added to the GRCh38 FASTA and GTF files accordingly, and a custom reference for cellranger was built from these annotation files using cellranger mkref (10x Genomics, version 6.0.0). The resultant custom reference was used for the CAR transgene mapping through cellranger count.

Plotting.

Unless otherwise stated, all plots for multi-omics data analysis were constructed in R (version 4.0.0) using ggplot2 (version 3.3.1).

V: Acknowledgements

We thank Phi Beta Psi, the Ullman Fund in Cancer Immunology, the Hoogland Lymphoma Research Pilot Projects, and Chicago Immunoengineering Innovation Center for financial support. Y.Hu was supported by the University of Chicago MSTP Training Grant (T32GM007281). N.As. was supported by the University of Chicago MTCR Training Grant (T32CA009594). H.S. was supported by R01CA022677. This project was supported by the National Center for Advancing Translational Sciences of the National Institutes of Health through Grant Number 5UL1TR002389-02 that funds the Institute for Translational Medicine. We thank Laura Pulido for expressing and purifying the dodecamer base protein. We thank the UChicago Flow Cytometry Facility for flow cytometer instrument use and assisted cell sorting, the UChicago Genomics Facility for use of their Novaseq-6000 sequencer, the Pritzker School of Molecular Engineering Next-Generation Sequencing core for use of their 10x Chromium Controller, and the UChicago Human Immunologic Monitoring Facility for patient biospecimen collection and cryopreservation. pHR CD19-empty CAR was a gift from Ron Vale (Addgene plasmid #113015).

VI: Contributions

Yifei Hu[1,2], Guoshuai Cao[1], Xiufen Chen[5], Xiaodan Huang[1], Nicholas Asby[1], Nicholas Ankenbruck[1], Ali Rahman[1], Ashima Thusu[1], Yanran He[4], Peter A. Riedell[4,5,6], Michael R. Bishop[5,6], Hans Schreiber[3,4,6,7], Justin P. Kline[3,4,5,6], Jun Huang[1,3,4]

[1]Pritzker School of Molecular Engineering, University of Chicago, Chicago, IL 60637, USA

[2]Pritzker School of Medicine, University of Chicago, Chicago, IL 60637, USA

[3]Committee on Immunology, University of Chicago, Chicago, IL 60637, USA

[4]Committee on Cancer Biology, University of Chicago, Chicago, IL 60637, USA

[5]Department of Medicine, University of Chicago, Chicago, IL 60637, USA

[6]The David and Etta Jonas Center for Cellular Therapy, University of Chicago, Chicago, IL 60637, USA

[7]Department of Pathology, University of Chicago, Chicago, IL 60637, USA

J.H. conceived the original concept for antigen-multimers. Y.Hu, J.K., and J.H. designed all experiments. Y.Hu, X.C., and N.As. conducted flow cytometry experiments. Y.Hu performed stimulation and magnetic selection experiments. X.H. performed ELISA. G.C. performed single-cell omics analysis. Y.Hu and A.R. analyzed staining titration data. A.T., A.R., N.An., Y.He, and Y.Hu cloned and transduced the CARs. J.K., P.R, and M.B. coordinated patient biospecimens for these studies. J.K., P.R., M.B., and H.S. reviewed the manuscript. Y.Hu wrote while J.H. and J.K. edited the manuscript.

SECTION IV: TWO-STAGE CAR T-CELL DIFFERENTIATION[3]

Chimeric antigen receptor (CAR) T-cell therapy has expanded therapeutic options for patients with diffuse large B-cell lymphoma (DLBCL). However, progress in improving clinical outcomes is limited by a poor understanding of CAR T-cell differentiation *in vivo.* To investigate the phenotypes and clonal dynamics of CAR T cells *in vivo*, we performed single-cell, multi-omics, and longitudinal analyses of CD28-costimulated CAR T cells from infusion product and peripheral blood of patients with DLBCL who were successfully treated with axicabtagene ciloleucel. Here, we show that CAR T cells undergo two distinct stages of post-infusion clonal expansion. Stage 1 (peak expansion, before day 14) is dominated by precursor exhausted-like $CD8^+$ and effector-T_h1-like $CD4^+$ CAR T cells. Stage 2 (post-peak contraction, after day 14) is dominated by effector/memory-like $CD8^+$ and memory-like $CD4^+$ CAR T cells. Importantly, clonal tracing and T-cell phenotypes both suggest that CAR T cells from peak expansion and post-peak contraction are biologically uncoupled. Moreover, trajectory analysis indicates that $CD8^+$ CAR T cells from Stage 1 and Stage 2 originate from proliferative and effector/memory-like precursors, respectively, in the infusion product, suggesting that baseline heterogeneity underlies two-stage differentiation. In addition to elucidating characteristics associated with complete responders, our findings inform endeavors to improve CAR T-cell expansion and persistence.

---

[3] This chapter is based on a submitted paper that is under review:
Cao, G.*, **Hu, Y.***, Althaus, T., Riedell, P. A., Bishop, M. R., Kline, J., & Huang, J. (2022). Two-Stage CAR T-Cell Differentiation in Patients with Large B-Cell Lymphoma. Submitted on 6/13/2022. ***Equal Contributions**

I: Introduction

Research efforts to improve the efficacy of CAR T cells hinge upon a biologically accurate and comprehensive picture of how CAR T cells differentiate in patients with r/r DLBCL. Early clinical studies to interrogate CAR T cells *in vivo* characterized CAR T-cell expansion and persistence in peripheral blood. For instance, during treatment with axicabtagene ciloleucel, an autologous formulation of CD28-costimulated CAR T-cell therapy, CAR T cells in peripheral blood expand, reach peak expansion, contract, and sometimes persist.[4,144] Expansion predicts complete response to therapy as well as grade of cytokine release syndrome (CRS) and immune effector cell-associated neurotoxicity syndrome (ICANS).[4,23] Persistence predicts durable remission and long-term immunosurveillance, though its relevance for preventing DLBCL relapse is obscure.[144–146] Although many factors correlate with expansion and persistence (including CAR design[87,147] and CAR T-cell phenotypes[22,23,39,148,149], among others[47,150,151]), how and why CAR T cells differentiate into more expansive or persistent phenotypes *in vivo* remains an open question. Existing studies focus mainly on 4-1BB-costimulated CAR T cells in a pediatric cancer setting with greater potential for long-term remission, hence the relevance of their insights to CD28-costimulated CAR T cells in the treatment of adult lymphoma is unknown. Furthermore, studies have focused on either CAR T-cell phenotypes[148,152,153] or clonal kinetics[140], but not on the integration of both data modalities to reach a comprehensive model. Dissecting CAR T-cell differentiation *in vivo* requires a single-cell approach that pairs CAR T-cell phenotypic profiles with clonal kinetics.

To elucidate CD28-costimulated CAR T-cell differentiation *in vivo*, we performed single-cell, multi-omics (paired RNA-seq/CITE-seq/TCR-seq), and longitudinal analyses of CD28-costimulated CAR T cells from infusion product and peripheral blood of patients with r/r DLBCL who were successfully treated with axicabtagene ciloleucel. CAR T cells from peripheral blood were stained and sorted using our recently developed CD19-tetramer.[154] Interestingly, we discovered that CAR T cells undergo two distinct clonal expansion stages in complete responders, each dominated by unique CAR T-cell phenotypes. Clonal tracing and T-cell phenotypes suggest that the earlier CAR T cells observed during peak expansion (Stage 1) are a distinct lineage from the later CAR T cells observed during post-peak contraction (Stage 2). Moreover, trajectory analysis demonstrates that post-infusion CD8$^+$ CAR T cells from each stage originate from unique precursors in the infusion product, suggesting that baseline heterogeneity underlies the two stages of clonal expansion. In addition to elucidating *in vivo* CAR T-cell biology, our findings may be fundamentally important for future endeavors to develop CAR T cells with superior expansion and persistence.

II: Results

Study design and clinical findings.

To interrogate CD28-costimulated CAR T-cell differentiation *in vivo*, we studied the phenotype and clonal dynamics of CAR T cells over the course of therapy from three patients who achieved complete responses (CR1, CR2, CR3) to axicabtagene ciloleucel (**Figure IV-1A**). Patients were diagnosed with r/r DLBCL and treated at the University of Chicago Medicine in 2019. All patients presented with grade ≥2 CRS or ICANS during therapy (**Table IV-1**). Complete response (i.e., no detectable lymphoma) was determined by positron emission tomography/computed tomography imaging 30 days after infusion product administration (figure IV-S1). To capture phenotypic heterogeneity and clonal dynamics throughout the course of therapy, we employed single-cell multi-omics analyses (paired RNA-seq/CITE-seq/TCR-seq via the 10x Genomics platform) on infusion product and longitudinal peripheral blood biospecimens. CAR T-cell clones were tracked across timepoints using their clonotypes as unique indices. CAR T cells were sorted from peripheral blood using our recently developed CD19-tetramer (representative staining in **Figure IV-1B**, figure IV-S2).[154] As expected, sorted cells specifically expressed the CAR transgene (**Figure IV-1C**). Peripheral blood CAR T cells were analyzed at multiple timepoints within 90 days following infusion product administration, in order to capture the CAR T-cell expansion, peak, and contraction phases.[4] While the three patients demonstrated the expected phases in peripheral blood CAR T-cell abundance, only CR2 yielded sufficient CAR T cells at day 90 for single-cell multi-omics analyses (**Figure IV-1D**).

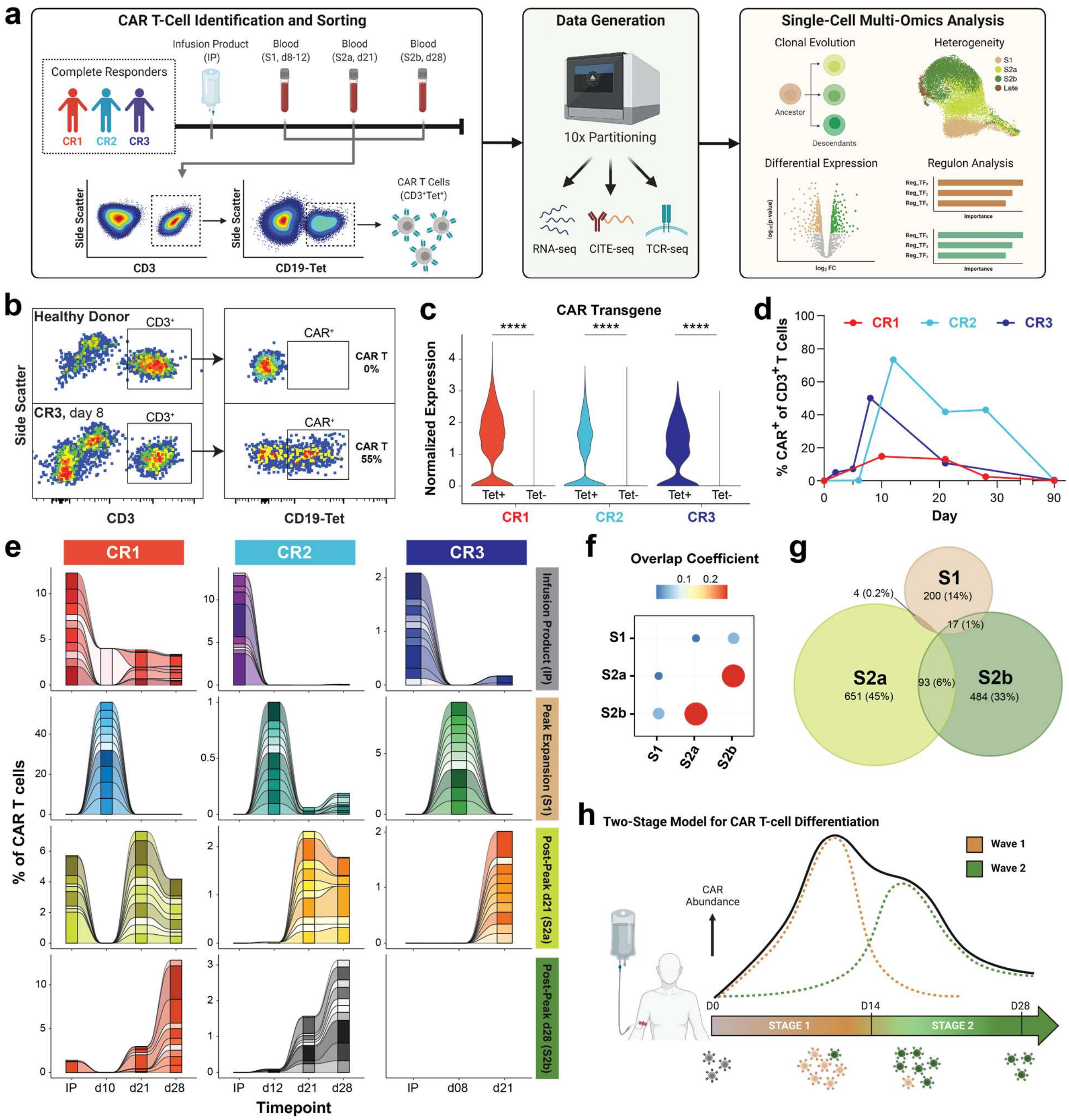

Figure IV-1. CAR T cells from complete responders undergo two waves of clonal expansion *in vivo*. (a) Schematic depicting sorting strategy, data generation, and single-cell multi-omics analysis of CAR T cells in peripheral blood from three CAR T-cell therapy patients (CR1, CR2, CR3) who exhibited complete responses to axicabtagene ciloleucel.

Figure IV-1, continued. (b) Representative flowplots depicting CD3 and CD19-tetramer staining of peripheral blood mononuclear cells from CR3 versus a healthy donor. (c) Violin plots depicting normalized CAR transgene mRNA expression of sorted CAR$^+$ and CAR$^-$ T cells (by CD19-tetramer staining) from CR patients. Expression levels were compared by Wilcoxon Rank-Sum test, whereby **** indicates p<0.0001. (d) Line plots depicting expansion and contraction of CAR abundance over the course of therapy. (e) Clonal tracing maps depicting representation of the top ten most abundant clones from infusion product, S1, S2a, and S2b (labeled by rows) at each timepoint (labeled on plots) for each CR patient (labeled by columns). (f) Dot plot depicting overlap coefficients between clonal repertoires of CAR T cells aggregated from CR patients at different stages of therapy. (g) Venn diagrams depicting number and proportions (in parenthesis) of shared TCR clonotypes of CAR T cells aggregated from CR patients at different stages of therapy. (h) Two-stage model according to clonotype repertoire and clonal tracing data. Bulk CAR T-cell expansion and contraction (black line) masks two distinct waves of clonal expansion (brown and green). Timepoints for the two waves are designated “Stage 1 (S1)” and “Stage 2 (S2)”. Associated with Figures IV-S1 through IV-S4.

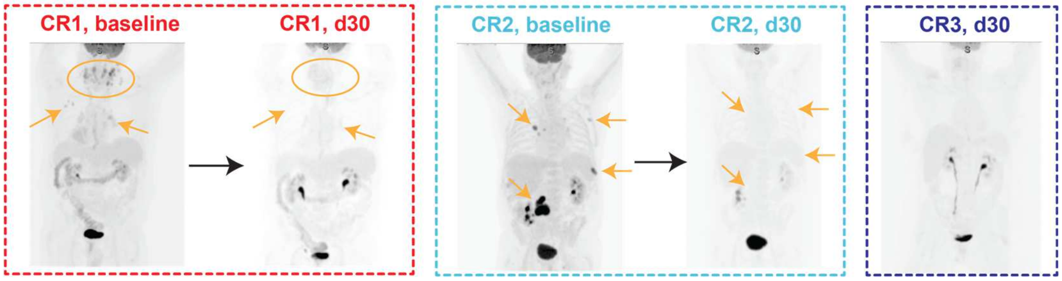

Figure IV-S1. PET/CT imaging for therapy response. Baseline and 30-day response assessment per PET/CT scan for select patients with complete response. In all images, lymphoma locations are denoted by orange arrows or circles. Associated with Figure IV-1.

Table IV-1. Patients' Clinical Characteristics

Characteristics	CR1	CR2	CR3
Age, y	74	69	55
Sex	Male	Male	Female
Disease stage	II	IV	II
No. of prior therapies	2	5	2
Prior lines of therapy	1. R-CHOP 2. R-ICE	1. R-CHOP 2. Benda-obinutuzumab 3. R-ICE 4. Hu5F9-G4 + rituximab (on clinical protocol) 5. R GemOx	1. DA-EPOCH w/ IT MTX 2. ICE
Disease status	Relapsed	Refractory (*e.g.*, relapsed then refractory)	Primary refractory
Baseline (Ref. range)			
LDH, U/L (116-245)	165	311	312
CRP, mg/dL (<0.5)	0	Not determined	3.5
Ferritin, ng/mL (20-300)	110	Not determined	576
ECOG PS	1	1	2
Bridging therapy	No	No	Yes
Product	Axicabtagene ciloleucel	Axicabtagene ciloleucel	Axicabtagene ciloleucel
Maximum Grade CRS	2	1	2
Maximum Grade ICANS	2	3	3
Tocilizumab or steroids	Tocilizumab & steroids	Tocilizumab & steroids	Tocilizumab & steroids
30-Day Response	Complete Response	Complete Response	Complete Response
Survival status	Deceased	Alive	Deceased
Cause of Death	Second Malignancy	---	Progressive lymphoma

Two stages of post-infusion CAR T-cell clonal expansion.

To analyze CAR T-cell population dynamics, we tracked CAR T-cell abundance in peripheral blood throughout the course of therapy via CD19-tetramer staining during sorting. CAR T-cell abundance at peak expansion ranged from 15% (CR1) to 73% (CR2) (**Figure IV-1D**). Peak expansion occurred between day 8-12, which is consistent with prior clinical findings.[4] Although the post-peak contraction rate varied between patients, CAR T-cell abundance was <1% in all CR patients by day 90 (figure IV-S2). For each timepoint, we quantified proportions of γδ, $CD8^+$, and $CD4^+$ T cells within the total CAR T-cell population by single-cell RNA-seq and CITE-seq. $CD8^+$ CAR T cells were the predominant population across all patients/timepoints, with the exception of early timepoints from CR1 and CR3, in which $CD4^+$ CAR T cells were more prevalent (figure IV-S2A). The remaining γδ T cells represented ≤8% of CAR T cells at all timepoints (figure IV-S3B).

Next, we used single-cell TCR-seq to define TCRα/β clonotypes and trace the top ten most abundant CAR T-cell clones from each timepoint across other timepoints (**Figure IV-1E**). No clone represented >8% of total CAR T cells at any timepoint. The most abundant infusion product clones were typically observed at only very low levels post-infusion, which is consistent with a prior study showing a decrease in diversity post-infusion.[58] Interestingly, clonal tracing analyses pointed towards two distinct waves of CAR T-cell clonal expansion: an earlier wave during peak expansion and a later wave during post-peak contraction. The most abundant clones at peak expansion (day 10 in CR1, day 12 in CR2, day 8 in CR3) were rarely observed (<0.2% in total) at post-peak timepoints (day 21 and 28). Conversely, the most abundant clones at post-peak timepoints were rarely observed (<0.1% in total) at peak expansion. However, the most abundant day 21 clones were present at day 28 and vice versa. Endogenous T cells from matched timepoints did not show the same exclusive patterns of clonal expansion, indicating that the two waves were CAR-specific (figure IV-S4). For instance, the most abundant endogenous clones at peak expansion were significantly observed (>2.9% in total) at post-peak timepoints and vice versa (>2.8% in total). Timeframes for the two waves of CAR T-cell clonal expansion were designated “Stage 1” (S1, peak expansion) and “Stage 2” (S2, post-peak). CR1 and CR2 had two S2 timepoints designated S2a (day 21) and S2b (day 28). CR3 only had the S2a timepoint due to sample availability. In agreement with clonal tracing findings, repertoire overlap analysis of CAR T cells also revealed that while S1 and S2 clones were distinct, S2a and S2b clones were similar (**Figure IV-1F-G**). Given that S1, S2a, and S2b were mutually spaced by ~1 week, the mere passage of time cannot explain our observations regarding the transition from S1 clones to S2 clones.

In conclusion, clonal tracing and repertoire overlap analyses suggest a two-stage CAR T-cell differentiation model, whereby S1 and S2 are timeframes for two distinct waves of CAR T-cell clonal expansion (**Figure IV-1H**). The two-stage differentiation model uncouples CAR T cells from peak expansion and post-peak contraction by designating them as separate lineages. Hence, the earlier CAR T cells observed during peak expansion are a distinct lineage from the later and more persistent CAR T cells. Moreover, these findings provide evidence against the intuitive idea that post-peak contraction in CAR T-cell abundance is due solely to apoptosis of short-lived CAR T cells from peak expansion. Rather, even as total CAR T-cell abundance was contracting in S2, a distinct subset of CAR T-cell clones was actually expanding and replacing the S1 clonal repertoire.

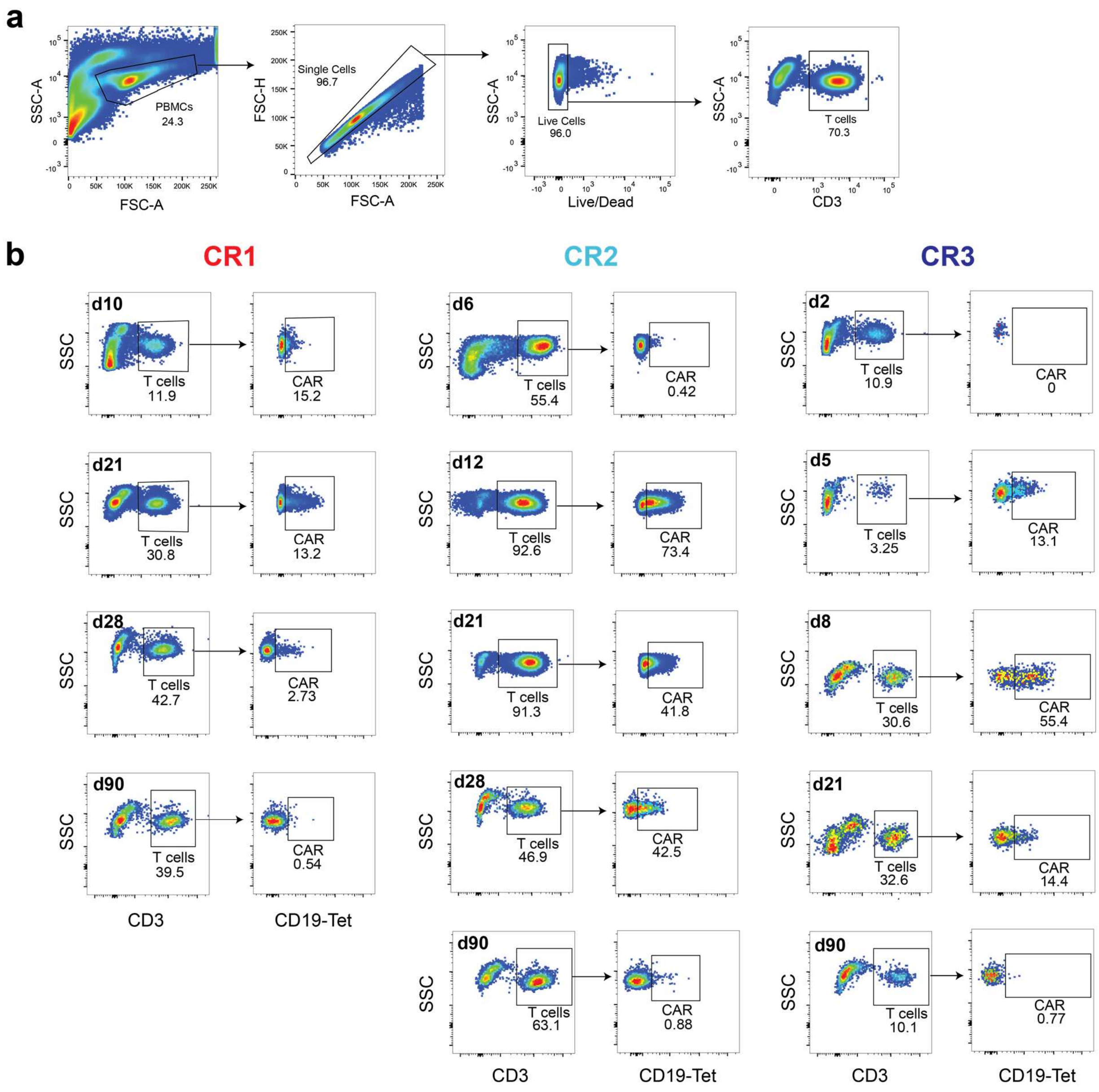

Figure IV-S2. CAR detection by CD19-tetramers. Flow plots demonstrating use of Brilliant Violet 421-labeled anti-CD3ε and Alexa Fluor 647-labeled CD19-tetramers for CAR T-cell detection, quantification, and sorting. (a) Gating strategy for CD3$^+$ T cells from patient PBMCs. (b) Gating for CAR T cells. PBMCs from a healthy donor (biological control) were used to draw CAR$^+$ gates. We analyzed post-infusion PBMCs at timepoints throughout the course of therapy from the 3 CR patients. Associated with Figure IV-1.

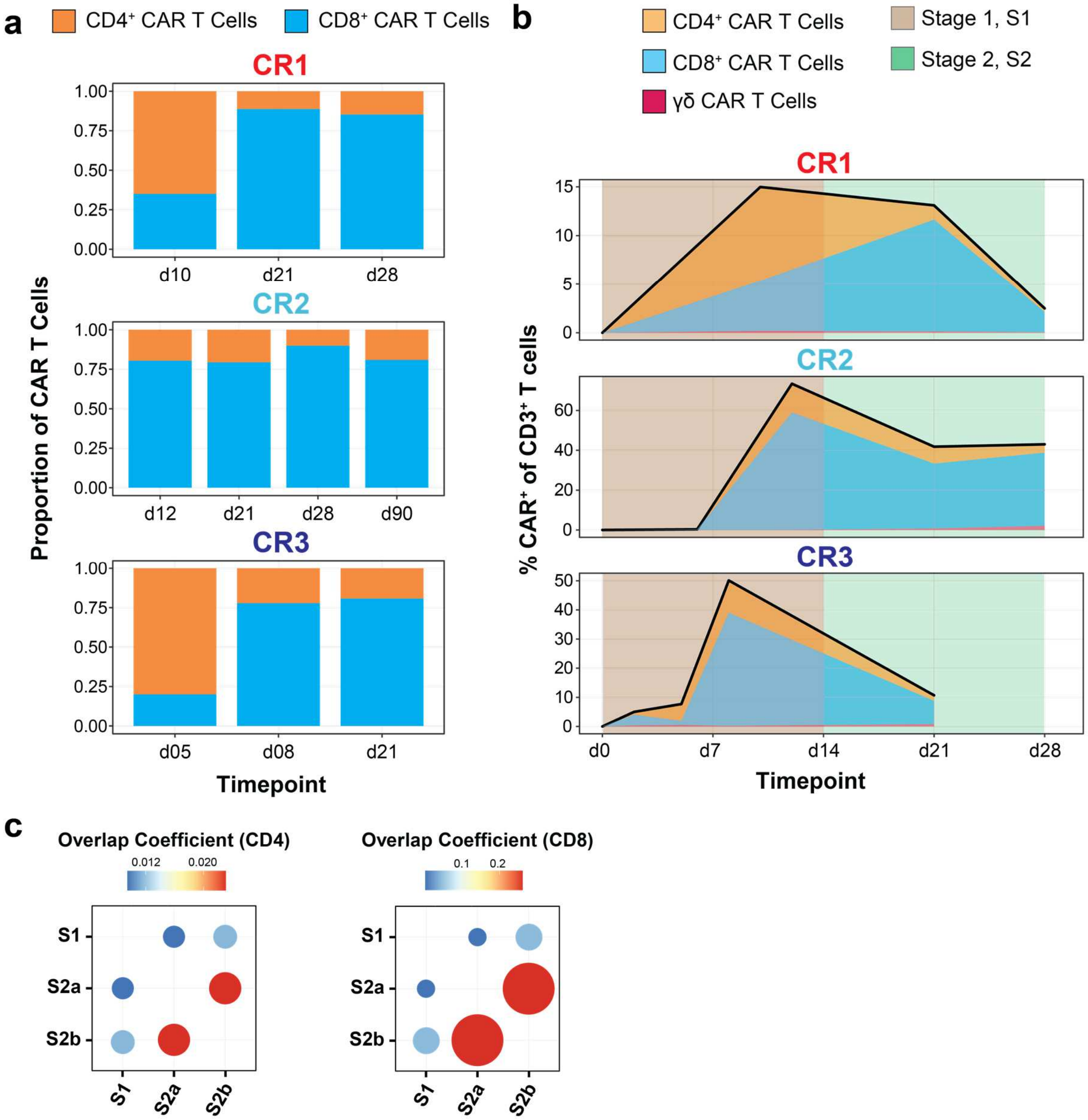

Figure IV-S3. CAR T-cell population characteristics. (a) Stacked bar graphs indicating the CD4 versus CD8 representation of CAR T cells (only αβ T cells) for each patient at various timepoints. (b) Line plots describing the CAR T-cell population at various timepoints. Total CAR abundance (black line) is depicted for each patient. The area under this line is colored according to proportion of CAR T cells that are CD4^{+}, CD8^{+}, or γδ T cells. The stage 1 (“S1”) and stage 2 (“S2”) timeframes are colored in the background accordingly. (c) Dot plot showing overlap coefficient between clonal repertoires of CD4^{+} CAR T cells (top) and CD8^{+} CAR T cells (bottom) from CR patients at different stages. Associated with Figure IV-1.

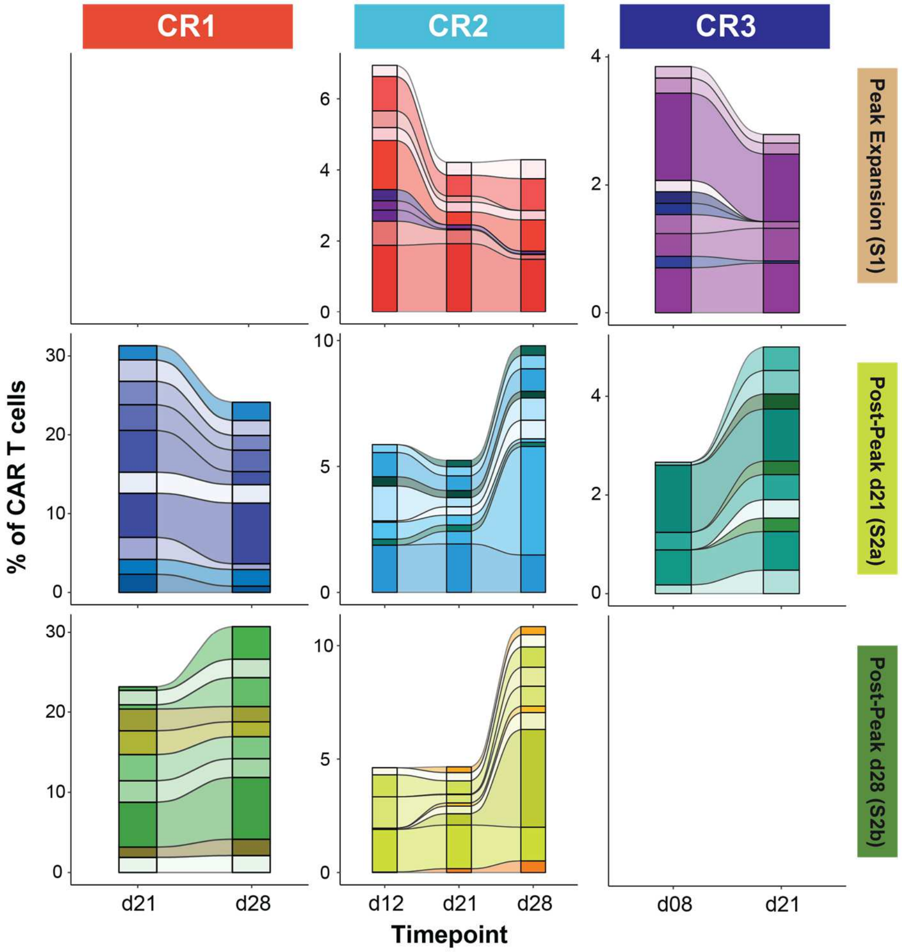

Figure IV-S4. Endogenous T-cell clonal kinetics. Clonal tracing maps depicting representation of the top ten most abundant endogenous T-cell clones from S1, S2a, and S2b (labeled by rows) at each timepoint (labeled on plots) for CR patients (labeled by columns). Associated with Figure IV-1.

Precursor exhausted-like (S1) to effector-like/memory-like (S2) CD8⁺ CAR T cells.

We hypothesized that unique CAR T-cell phenotypes dominate the two distinct waves of CAR T-cell clonal expansion. To test this hypothesis, we first focused on $CD8^+$ CAR T cells, the predominant CAR T cell at most timepoints. After filtering $CD8^+$ CAR T cells from the post-infusion dataset, twelve $CD8^+$ T-cell clusters were identified (**Figure IV-2A**) based on gene and protein markers (**Figure IV-2B**, expanded marker set in figure IV-S5A). No cluster was patient-specific (figure S6a). All clusters expressed the CAR transgene and CD8α, validating our CD19-tetramer sorting and filtering process, respectively. Most clusters expressed *CXCR3*, a chemokine receptor expressed by activated T cells. Moreover, most clusters expressed *CX3CR1* and *TBX21*, markers of effector and effector memory CD8$^+$ T cells, which is consistent with the established link between CD28 costimulation and effector memory (rather than central memory) differentiation.[87,147] Proliferative (*MKI67*$^+$*TOP2A*$^+$) and apoptotic (higher mitochondrial gene content) clusters, distinct from the other ten clusters, were also identified.

Clusters were annotated with their closest subset identity: effector-like (EFF, *CX3CR1*$^+$*TCF7*$^-$), memory-like (MEM, *CX3CR1*$^+$*TCF7*$^+$), or precursor exhausted-like[155,156] (PEX, *TCF7*$^+$*TOX*$^+$ and/or *TCF7*$^+$*NR4A2*$^+$). EFF clusters (3 in total) appeared to occupy an activation continuum delineated by a gradient in *CXCR3* and *CD38* expression along the top edge of the UMAP. The most activated EFF cluster (*CXCR3*$^+$*CD38*$^+$) exhibited the greatest clonal repertoire overlap with, and lay closest to, the proliferating cluster on the UMAP (see figure IV-S5B), suggesting a link between activation and proliferation. MEM clusters (3 in total) did not express *CCR7*, indicating an effector memory phenotype. PEX clusters (4 in total) exhibited upregulation of *GZMK*[157] and co-expressed multiple inhibitory receptors, including PD-1, TIM-3, LAG-3, CD39, and TIGIT (figure IV-S5C).

Phenotypic compositions of CD8$^+$ CAR T cells from S1 and S2 were compared (**Figure IV-2C**). S1 CAR T cells were predominantly PEX (90%) and expressed *CXCR6*, a chemokine receptor that facilitates CAR T-cell trafficking into solid tumors.[158] In contrast, S2 CAR T cells were EFF (50-70%) or MEM (20-30%). These findings were consistent across all three CR patients (figure IV-S6B-C). Between S2a and S2b, EFF CAR T cells shifted from *CXCR3*$^+$ towards *CXCR3*$^-$, MEM CAR T cells shifted from *CXCR6*$^+$ towards *CXCR6*$^-$, and proliferating T cells decreased from 8% to 2% (see figure IV-S6), indicative of less activated CAR T cells. However, the overall phenotypic composition at S2a and S2b remained largely similar, which reinforced our clonal tracing and repertoire overlap findings. Finally, late CD8$^+$ CAR T cells (day 90 from CR2) were predominantly *CXCR6*$^{-}$ PEX (80%), some of which also expressed *CCR7* (figure IV-S9a-b), which is consistent with prior studies linking *CCR7* with long-term CAR T-cell persistence.[47,148,159]

Transcriptional profiles from different stages were compared via gene set enrichment analysis (GSEA). S1 CAR T cells upregulated gene sets for cell contraction, apoptosis, and glycolysis, while S2 CAR T cells upregulated gene sets for memory and effector T cells (**Figure IV-2D**), in general agreement with the phenotypic shift from PEX to EFF/MEM between S1 and S2. Interestingly, the most differentially expressed gene sets involved cytokine response. TNFα response genes (including *TNFAIP3*, *NFKBIA*, *DUSP1*) were upregulated in S1 CAR T cells, while type I interferon (IFN-I) response genes (including *STAT1*, *SPON2*, *KLRD1*) were upregulated in S2 CAR T cells (figure IV-S5D). In accordance with GSEA findings, some S2 EFF and MEM clusters expressed *IRF7*, a transcription factor in the IFN-I pathway.[160] Finally, we compared S2a and S2b transcriptomic profiles (**Figure IV-2E**). S2a CAR T cells upregulated gene sets for negative regulation of apoptosis, while S2b CAR T cells upregulated gene sets for leukopenia and intrinsic apoptosis (figure IV-S5E). These apoptotic patterns explain the overall contraction of the CD8^{+} CAR T-cell population during S2.

Overall, we discovered that the CD8^{+} CAR T-cell phenotype shifted from PEX to EFF/MEM between S1 and S2 (**Figure IV-2F**), which supports our hypothesis that each wave is dominated by unique CAR T-cell phenotypes. Since exhaustion is a distinct trajectory from effector or memory T-cell differentiation[161], these findings support the categorization of S1 and S2 CAR T cells as separate lineages and reinforce our two-stage differentiation model.

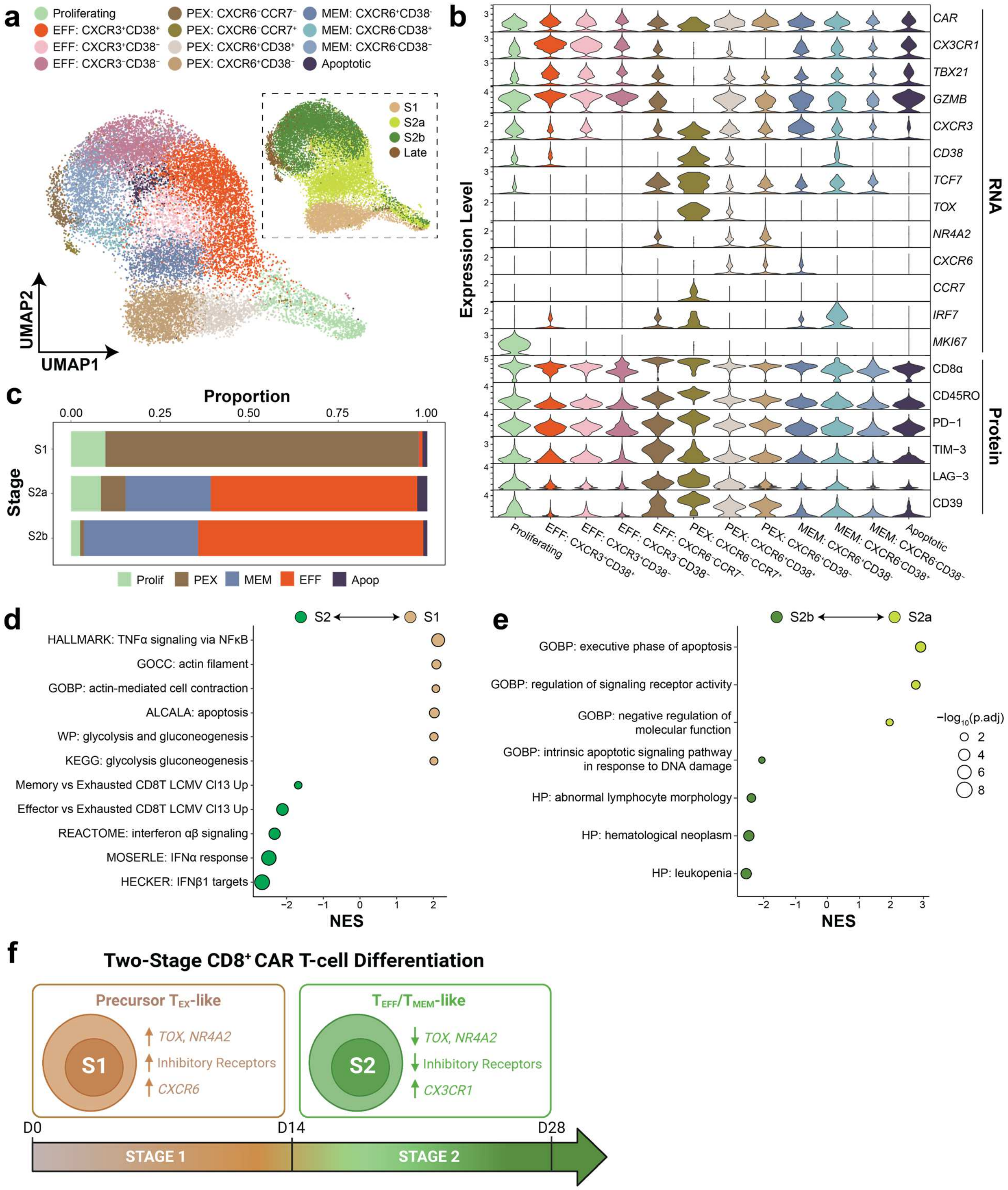

Figure IV-2. Precursor exhausted-like to effector-like/memory-like CD8$^+$ CAR T cells between S1 and S2. (a) UMAP depicting single-cell transcriptomes of CD8$^+$ CAR T cells from CR patients in 12 T-cell clusters. EFF, PEX, and MEM clusters are colored in shades of red, brown, and blue respectively. Inset depicts distribution of transcriptomes among stages of therapy. (b) Violin plots depicting normalized expression levels of key genes and proteins for annotation and phenotyping. For extended version, see figure IV-S6a. (c) Stacked bar graph depicting proportions of each T-cell subset at different stages.

Figure IV-2, continued. (d,e) Gene set enrichment analysis comparing CD8⁺ CAR T cells between S1 and S2 (d) or between S2a and S2b (e). For each gene set, direction and statistical significance of enrichment are indicated by the circle's color and size respectively. (f) Two-stage model of CD8⁺ CAR T-cell differentiation. Abbreviations: EFF, effector-like; PEX, precursor exhausted-like; MEM, memory-like; NES, normalized enrichment score. Associated with Figures IV-S5, IV-S6, and IV-S9.

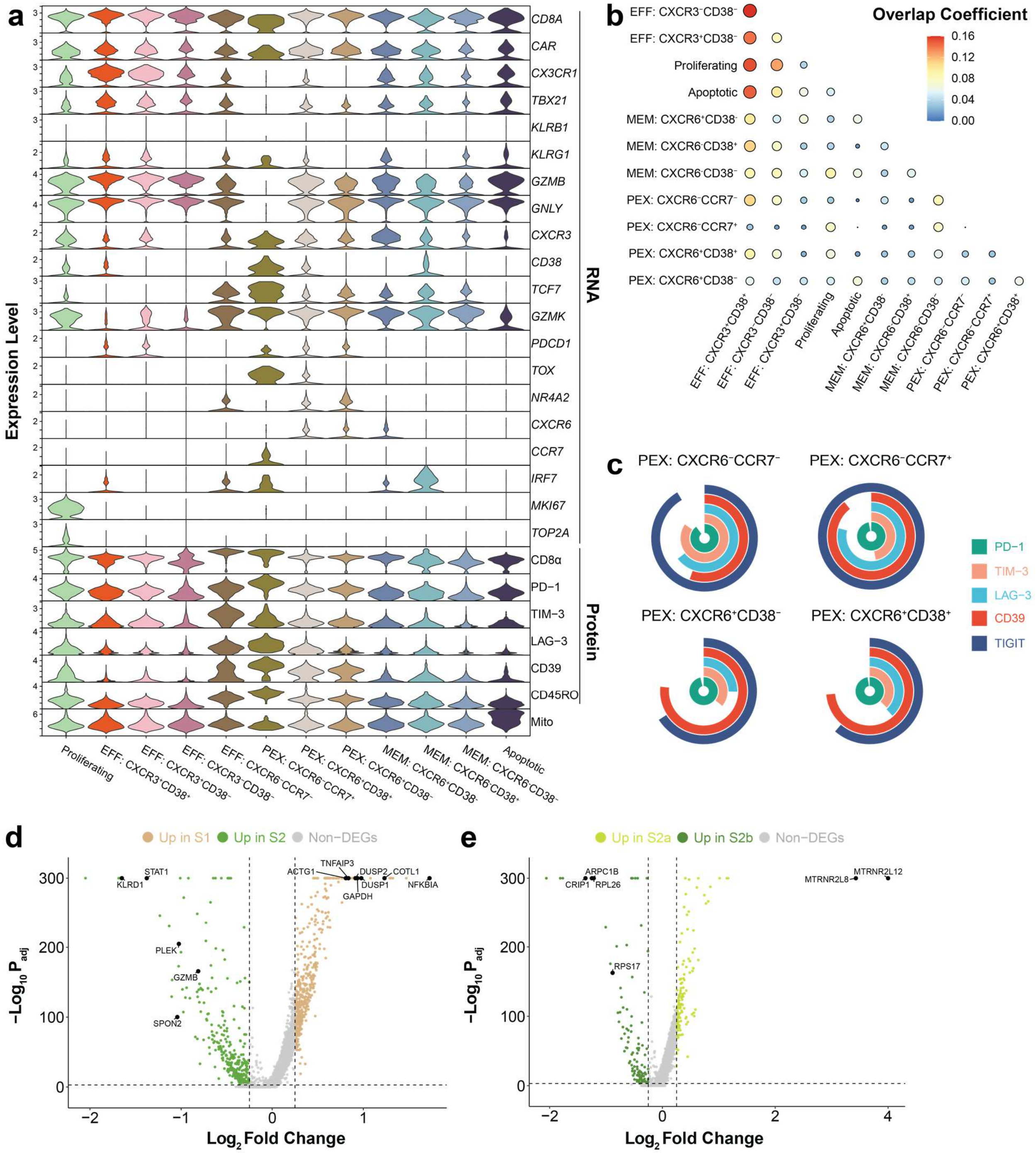

Figure IV-S5. Phenotypic heterogeneity of CD8⁺ CAR T cells. (a) Violin plots depicting normalized expression levels of key genes and proteins among the 12 CD8⁺ CAR T-cell clusters.

Figure IV-S5, continued. (b) Dot plot depicting overlap coefficient between clonal repertoires of clusters. (c) Overlapping pie charts depicting co-expression of inhibitory receptors on the four precursor exhausted clusters. (d,e) Volcano plot depicting log fold-change and adjusted p-value of differentially expressed genes in S1 versus S2 (d) and S2a versus S2b (e). Key genes are marked accordingly. Associated with Figure IV-2.

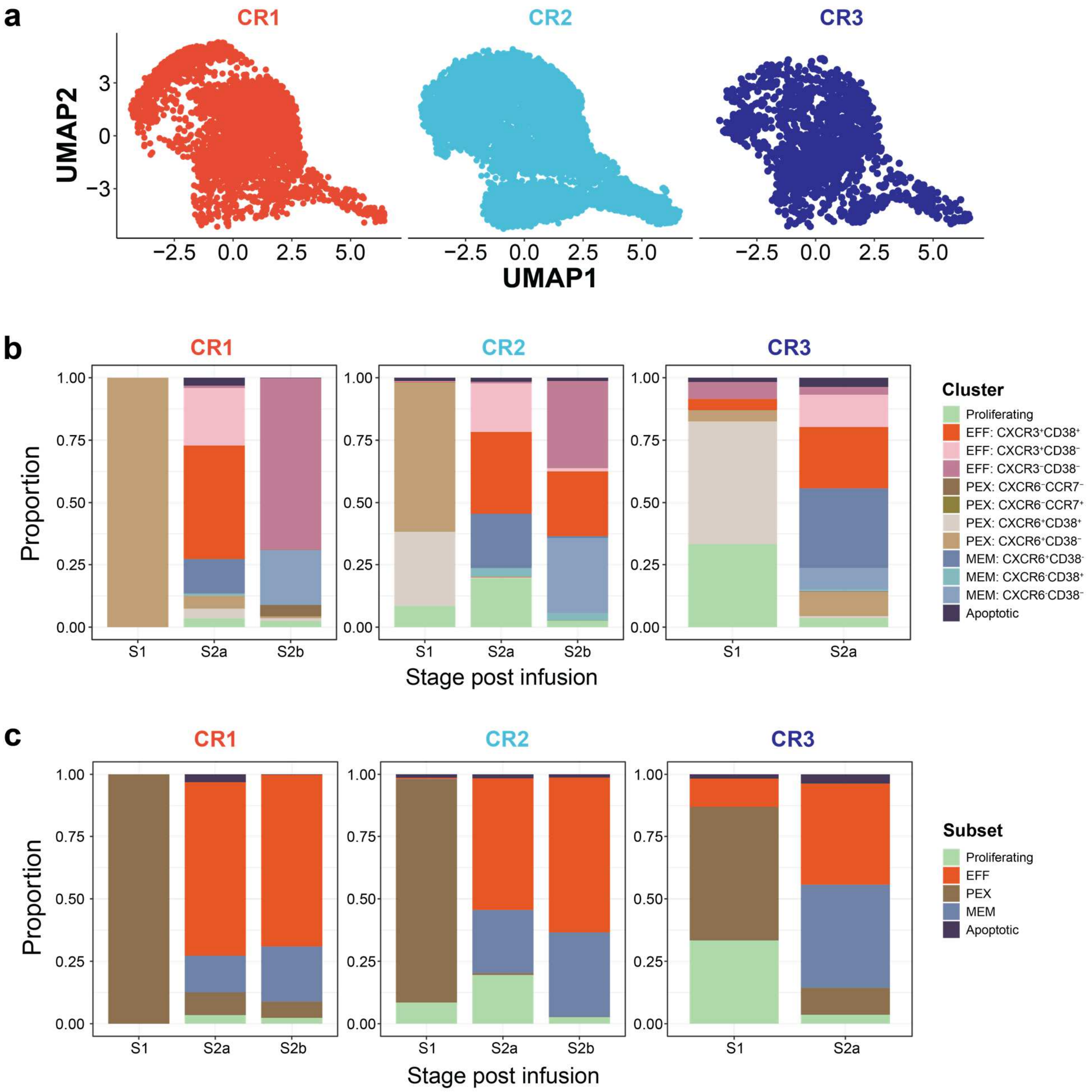

Figure IV-S6. Patient distribution of $CD8^+$ CAR T cells. (a) Colored UMAPs depicting how $CD8^+$ CAR T cells from each CR patient are distributed on the overall harmonized UMAP. (b,c) Stacked bar graphs depicting proportions of $CD8^+$ CAR T cells represented in each cluster (b) or T-cell subset (c) for each CR patient. Associated with Figure IV-2.

Effector T_h1-like (S1) to memory-like (S2) CD4$^+$ CAR T cells.

We next investigated whether each wave of clonal expansion is also associated with unique CD4$^+$ CAR T-cell phenotypes. Clustering, annotation, phenotypic composition analysis, and GSEA were carried out in the same manner as for CD8$^+$ CAR T cells. Six CD4$^+$ T-cell clusters, all expressing the CAR transgene and CD4, were identified based on gene and protein markers (**Figure IV-3A-B**, expanded marker set in figure IV-S7A). No cluster was patient-specific (figure IV-S8A). All clusters expressed *CXCR3*, indicating T-cell activation and type 1 helper differentiation. One cluster was proliferative (*MKI67*$^+$*TOP2A*$^+$).

Clusters were annotated as: effector type 1 helper-like (EFF-T_h1, *KLRB1*$^+$*TBX21*$^+$), memory-like[162] (MEM, *KLRB1*$^+$*TBX21*$^-$), and regulatory-like (REG, *FOXP3*$^+$*IL2RA*$^+$*IL7R*^{low} and CD25^{hi}). EFF-T_h1 clusters (2 in total, *CXCR6*$^+$ or *CXCR6*$^-$) upregulated cytolytic markers (*GZMK*, *GZMA*, *PRF1*, *GNLY*) and inhibitory receptors (*CTLA4*, *PDCD1*, *LAG3*, CD39), resembling cytolytic CD4$^+$ CAR T cells described recently.[148] IRF7 was upregulated in the *CXCR6*$^+$ EFF-T_h1 cluster, indicating response to IFN-I signaling. MEM clusters (2 in total) were *CCR7*$^+$ or *CCR7*$^-$, indicating central memory and effector memory phenotypes respectively. Consistent with their annotation, both MEM clusters downregulated inhibitory receptors (*CTLA4*, *PDCD1*, *LAG3*, PD-1, CD39) and cytolytic markers (*GNLY*, *GZMK*, *GZMA*, *PRF1*). The *CCR7*$^+$ MEM cluster upregulated *IRF7*, which is consistent with the role of IFN-I in central memory CD4$^+$ T-cell development.[163] *CCR7*$^+$ MEM and proliferative clusters overlapped in their clonal repertoires (figure IV-S7B) and lie in proximity on the UMAP, indicating that *CCR7*$^+$ MEM cells may self-renew. The REG cluster upregulated Treg markers (*FOXP3*, *IL2RA, CTLA4*, CD25), downregulated *KLRB1*, and upregulated *IKZF2*, indicating a stable and suppressive phenotype.[164,165] Although CAR Tregs can inhibit efficacy of effector CAR T cells in preclinical models[166], the existence of human CAR Tregs *in vivo* from clinical formulations has not been previously described.

Across all three CR patients, S1 CD4$^+$ CAR T cells were predominantly *CXCR6*$^-$ EFF-T$_h$1 cells (85%), while S2 CD4$^+$ CAR T cells were MEM (30-70%) or *CXCR6*$^+$ EFF-T$_h$1 cells (30-50%) (**Figure IV-3C**, figure IV-S8B-C). Between S2a and S2b, EFF-T$_h$1 representation decreased (50% to 27%) while MEM representation increased (30% to 70%), suggesting that memory-like CD4$^+$ CAR T cells are more persistent. REG representation was significant in S2a (12%), but became negligible during S2b (<1%). Finally, late CD4$^+$ CAR T cells (day 90 from CR2) were predominantly MEM (80%) or EFF-T$_h$1 (20%) (figure IV-S9C-D).

GSEA revealed upregulation of gene sets for cytoskeletal regulation and hypoxia in S1 CAR T cells, and ribosomal biogenesis in S2 CAR T cells (**Figure IV-3D**), in agreement with the phenotypic shift from EFF-T$_h$1 to MEM phenotype. Similar to the CD8$^+$ CAR T cell findings, some of the most differentially expressed gene sets involved cytokine response. S1 CAR T cells upregulated TNFα and TGFβ1 response genes (including *TNFAIP3*, *NFKBIA*, *PMAIP1*), while S2 CAR T cells upregulated IFN-I response genes (including *STAT1*) (figure IV-S7C). S1-specific upregulation of the TGFβ1 response gene set is consistent with the presence of REG cells during S1. Comparing S2a and S2b transcriptomic profiles (**Figure IV-3E**), we found that gene sets for negative regulation of apoptosis were upregulated in S2a CD4$^+$ CAR T cells, while gene sets for leukopenia were upregulated in S2b CD4$^+$ CAR T cells (see figure IV-S7D), which explains the overall contraction of the CD4$^+$ CAR T-cell population during S2.

Our findings that the CD4$^+$ CAR T cell phenotype shifted from EFF-T$_h$1 to MEM between S1 and S2 (**Figure IV-3F**), like the CD8$^+$ CAR T results, support our hypothesis that each wave is dominated by unique CAR T-cell phenotypes. Since lineage-committed T$_h$1-polarized effector CD4$^+$ T cells are not known to regress back into non-committed central or effector memory T cells[167,168], our phenotype findings further support the two-stage differentiation model. Furthermore, PEX CD8$^+$ and EFF-T$_h$1 CD4$^+$ T cells are both known to be antigen-dependent and short-lived populations, which is consistent with the transient nature of the S1 wave. Both CD4$^+$ and CD8$^+$ CAR T cell results suggest that the CAR T-cell population increasingly upregulates apoptosis and contracts over the course of S2. Notably, we observed S1- and S2-specific upregulation of TNFα and IFN-I response gene sets, respectively, for both CD4$^+$ and CD8$^+$ CAR T cells, which suggests that the cytokine milieu in peripheral blood may change over the course of therapy.

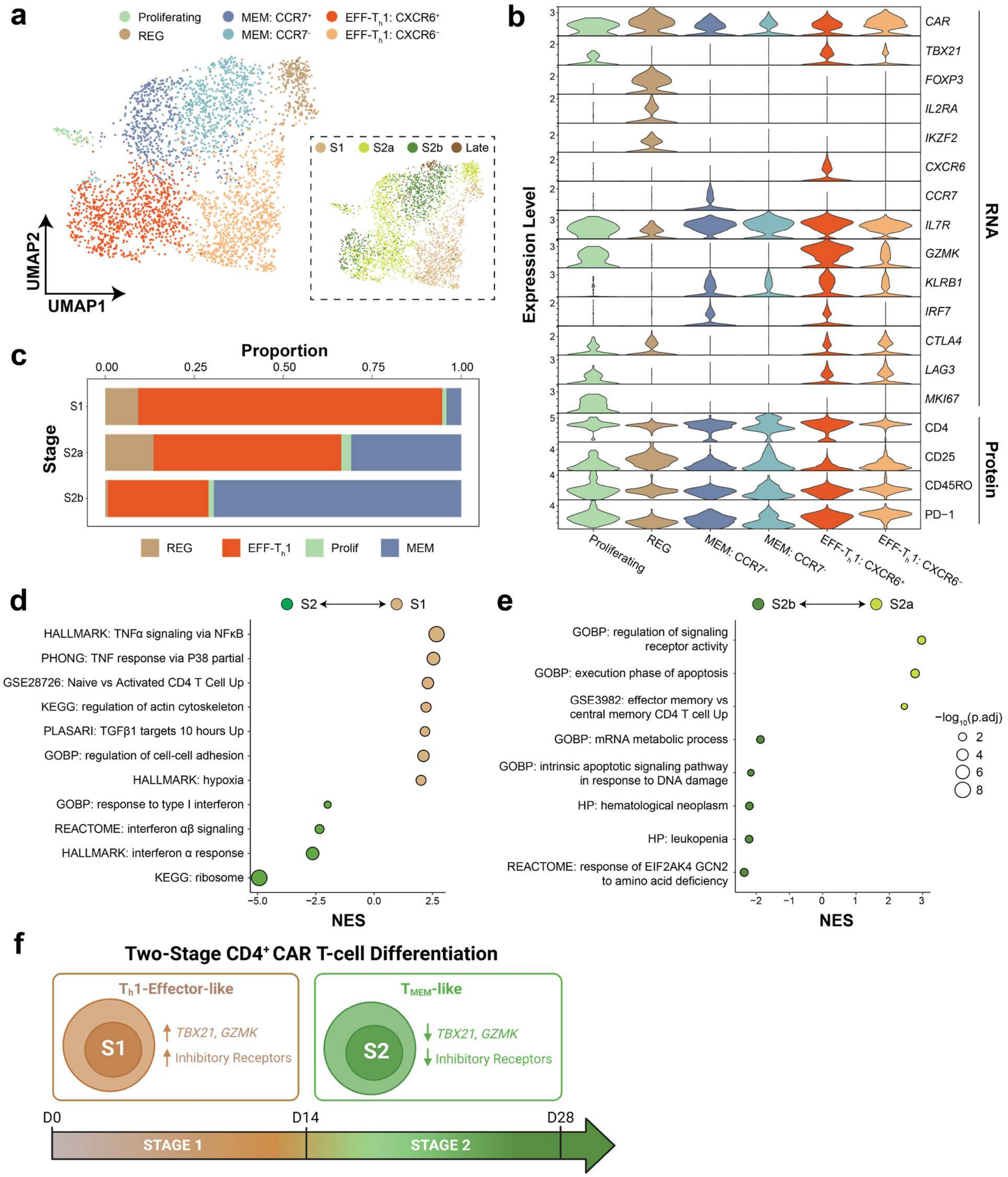

Figure IV-3. Effector-T$_h$1-like to memory-like CD4$^+$ CAR T cells between S1 and S2. (a) UMAP depicting single-cell transcriptomes of CD4$^+$ CAR T cells from CR patients in 6 T-cell clusters. REG, MEM, and EFF-T$_h$1 clusters are colored in shades of brown, blue, and red respectively. Inset depicts distribution of transcriptomes among stages of therapy. (b) Violin plots depicting normalized expression levels of key genes and proteins for annotation and phenotyping. For extended version, see figure IV-S8a. (c) Stacked bar graph depicting proportion represented within each T-cell cluster at different stages.

Figure IV-3, continued. (d,e) Gene set enrichment analysis comparing CD4$^+$ CAR T cells between S1 and S2 (d) or between S2a and S2b (e). For each gene set, direction and statistical significance of enrichment are indicated by the circle's color and size respectively. (f) Two-stage model of CD4$^+$ CAR T-cell differentiation. Abbreviations: REG, regulatory-like; MEM, memory-like; EFF-T$_h$1, effector T helper 1-like; NES, normalized enrichment score. Associated with Figures IV-S7, IV-S8, and IV-S9.

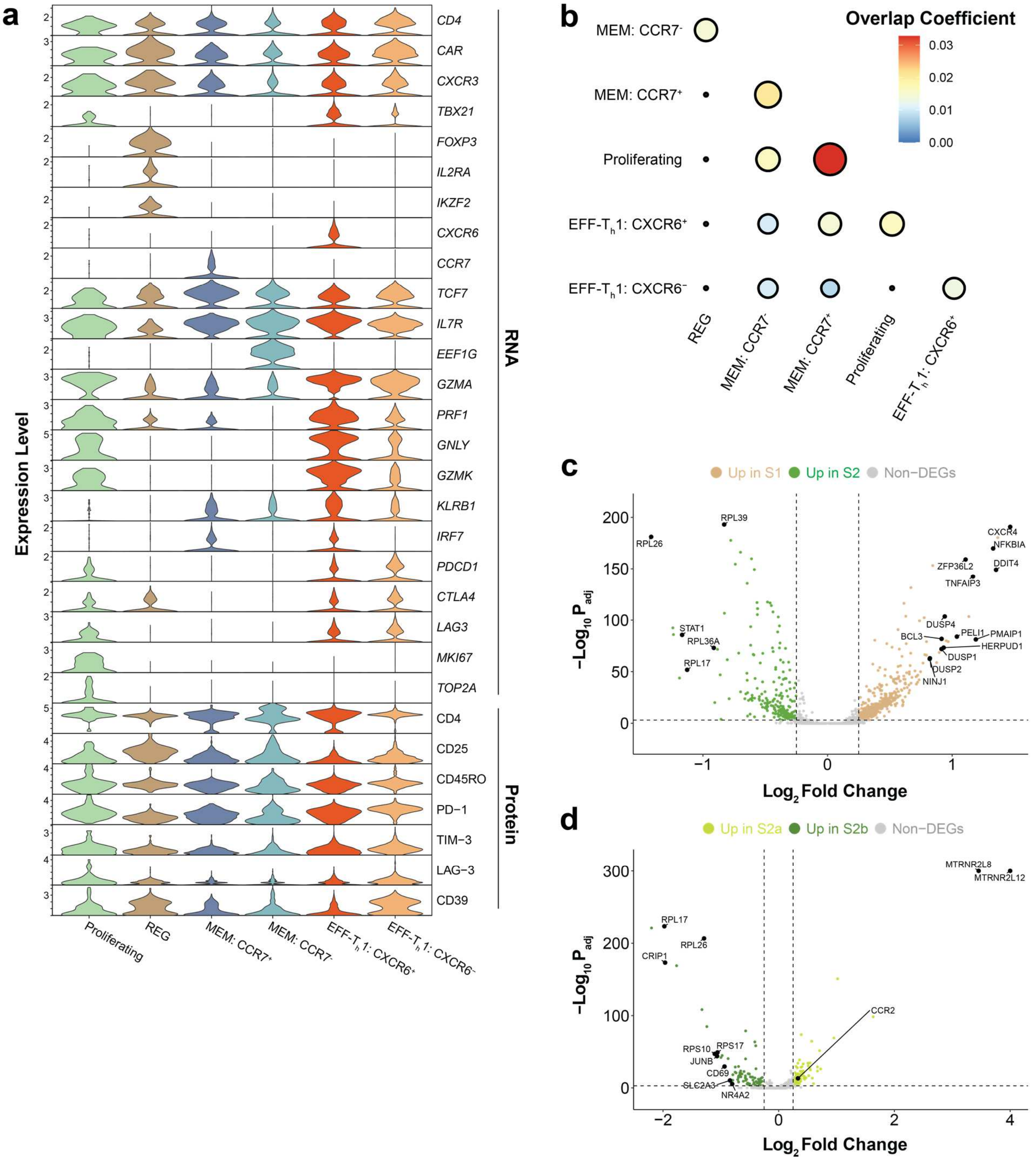

Figure IV-S7. Phenotypic heterogeneity of CD4$^+$ CAR T cells. (a) Violin plots depicting normalized expression levels of key genes and proteins among the 6 CD4$^+$ CAR T-cell clusters.

Figure IV-S7, continued. (b) Dot plot depicting overlap coefficient between clonal repertoires of clusters. (c,d) Volcano plot depicting log fold-change and adjusted p-value of differentially expressed genes in S1 versus S2 (c) and S2a versus S2b (d). Key genes are marked accordingly. Associated with Figure IV-3.

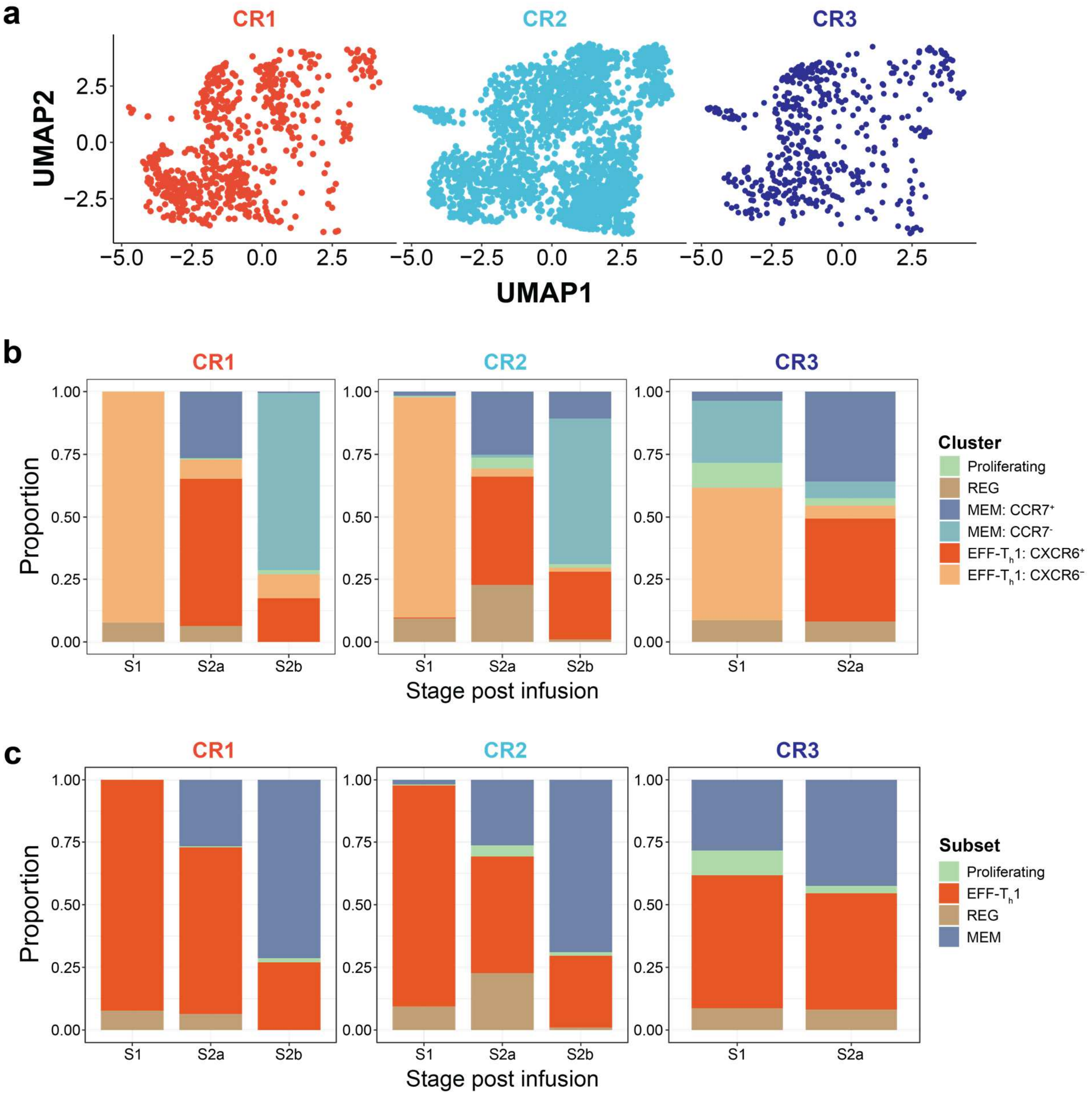

Figure IV-S8. Patient distributions of CD4$^+$ CAR T cells. (a) Colored UMAPs depicting how CD4$^+$ CAR T cells from each CR patient are distributed on the overall harmonized UMAP. (b,c) Stacked bar graphs depicting proportions of CD4$^+$ CAR T cells represented in each cluster (b) or T-cell subset (c) for each CR patient. Associated with Figure IV-3.

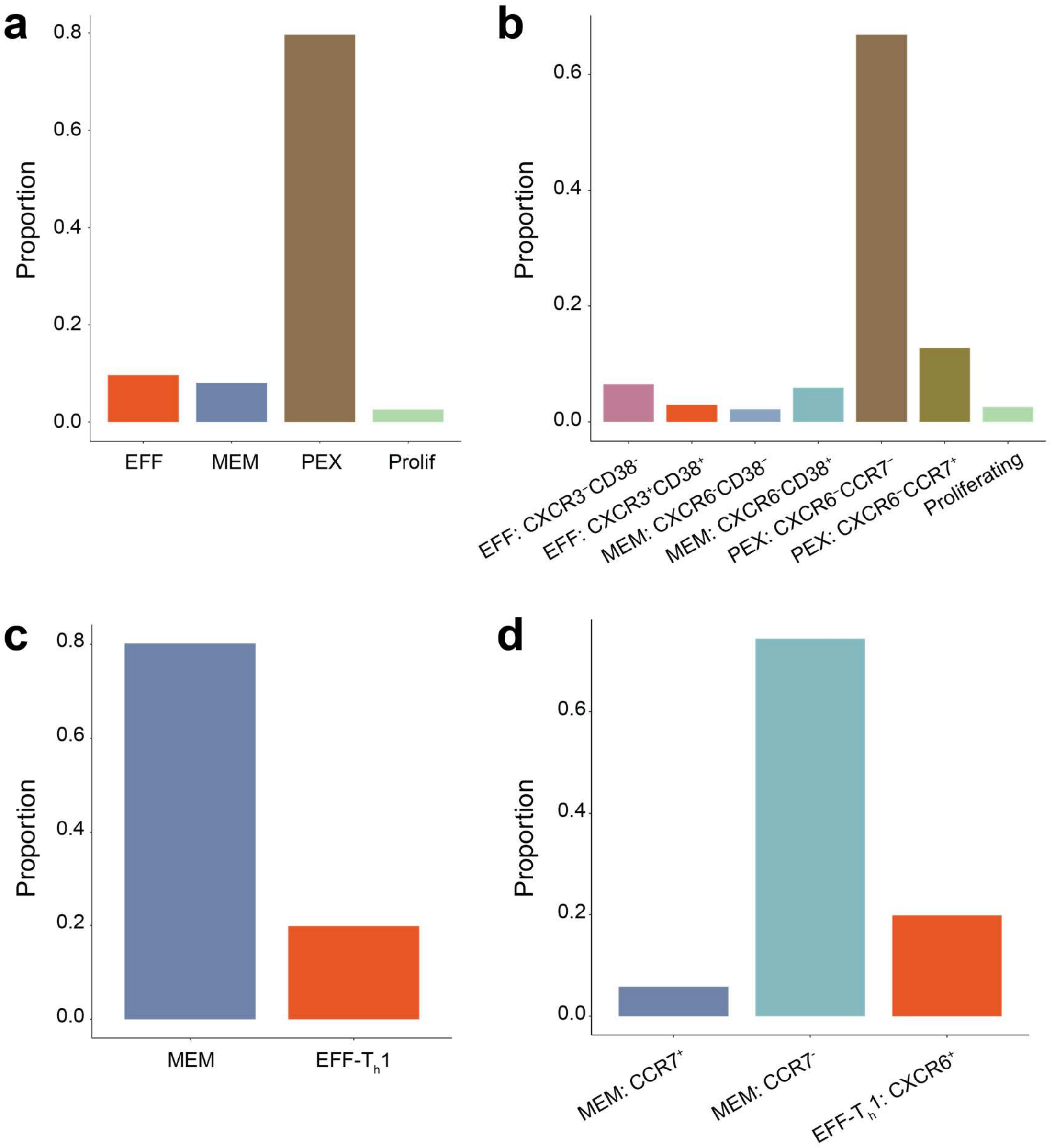

Figure IV-S9. Phenotypic heterogeneity of late CAR T cells from CR2. Bar graphs indicating the population composition of CAR T cells from CR2 at a late timepoint (d90). (a,b) Graph depicting CD8$^+$ CAR T-cell subsets (a, left) and clusters (b, right). (c,d) Graph depicting CD4$^+$ CAR T-cell subsets (c, left) and clusters (d, right). Associated with Figures IV-2 and IV-3.

Distinct regulatory networks underlie S1 and S2 CAR T cells.

Having established the clonal dynamics and phenotypes of S1 and S2 CAR T cells, we next interrogated S1- and S2-specific regulatory networks using a machine-learning model (**Figure IV-4A**). We transformed single-cell transcriptome data into regulomes and calculated regulon scores. These scores were used to train a machine-learning model to classify S1 and S2 CAR T cells. The model demonstrated high predictive accuracy (>90%) for S1 versus S2 classification in both $CD8^+$ and $CD4^+$ CAR T cells (figure IV-S10).

Top stage-specific regulatory networks were identified based on the importance of each regulon for the model's predictions (**Figure IV-4B-C**) (see figure IV-S11A-B for extended version). For $CD8^+$ CAR T cells, S1-predictive regulons with known functions included the FOSL2, FLI1, and ELF1 regulons (**Figure IV-4D-E**, figure IV-S11C). Based on the literature, FOSL2 antagonizes exhausted $CD8^+$ T-cell differentiation.[169] On the other hand, FLI1 antagonizes effector $CD8^+$ T-cell differentiation[170], and itself can be upregulated by ELF1.[171] Targets of these regulons included transcription factors associated with T-cell exhaustion, including *PRDM1*, *NR4A2*, *NFATC2*, and *IKZF3*.[172,173] In particular, concurrent activation of FLI1 and FOSL2 regulons, which play opposing roles in exhaustion versus effector differentiation, may account for the S1-specific PEX phenotype. On the other hand, S2-predictive regulons with known functions included the KLF6, JAZF1, and ELF4 regulons (**Figure IV-4F**, figure IV-S11D). KLF6 and JAZF1 transcription factors have previously been correlated with less dysfunctional and more cytotoxic $CD8^+$ tumor-infiltrating T cells[172], while ELF4 promotes memory $CD8^+$ T cells by maintaining quiescence.[174] Target of these regulons included genes (including *PRF1*, *CX3CR1*) and transcription factors (including *TBX21*, *ZEB2*, *ID2*) associated with effector and effector memory differentiation, which is consistent with S2-specific EFF/MEM phenotypes. In $CD4^+$ CAR T cells, S1-predictive regulons with known functions included the regulon for KLF2 (figure IV-S11E), which represses $CD4^+$ follicular helper T-cell differentiation and enhances T_h1 differentiation.[175] S1-specific upregulation of this regulon is consistent with S1-specific EFF-T_h1 phenotype. On the other hand, S2-predictive regulons with known functions included the STAT1, IRF1, and IRF7 regulons (figure IV-S11F), which is consistent with S2-specific upregulation of IFN-I response genes.

Based on our machine-learning model and regulon scores, we identified S1- and S2-predictive regulatory networks that are consistent with S1- and S2-specific phenotypes for both CD8$^+$ and CD4$^+$ CAR T cells. In addition to elucidating molecular determinants underlying the S1 and S2 waves, these analyses reveal previously characterized as well as new regulatory targets that may be manipulated in future endeavors to control CAR T-cell differentiation.

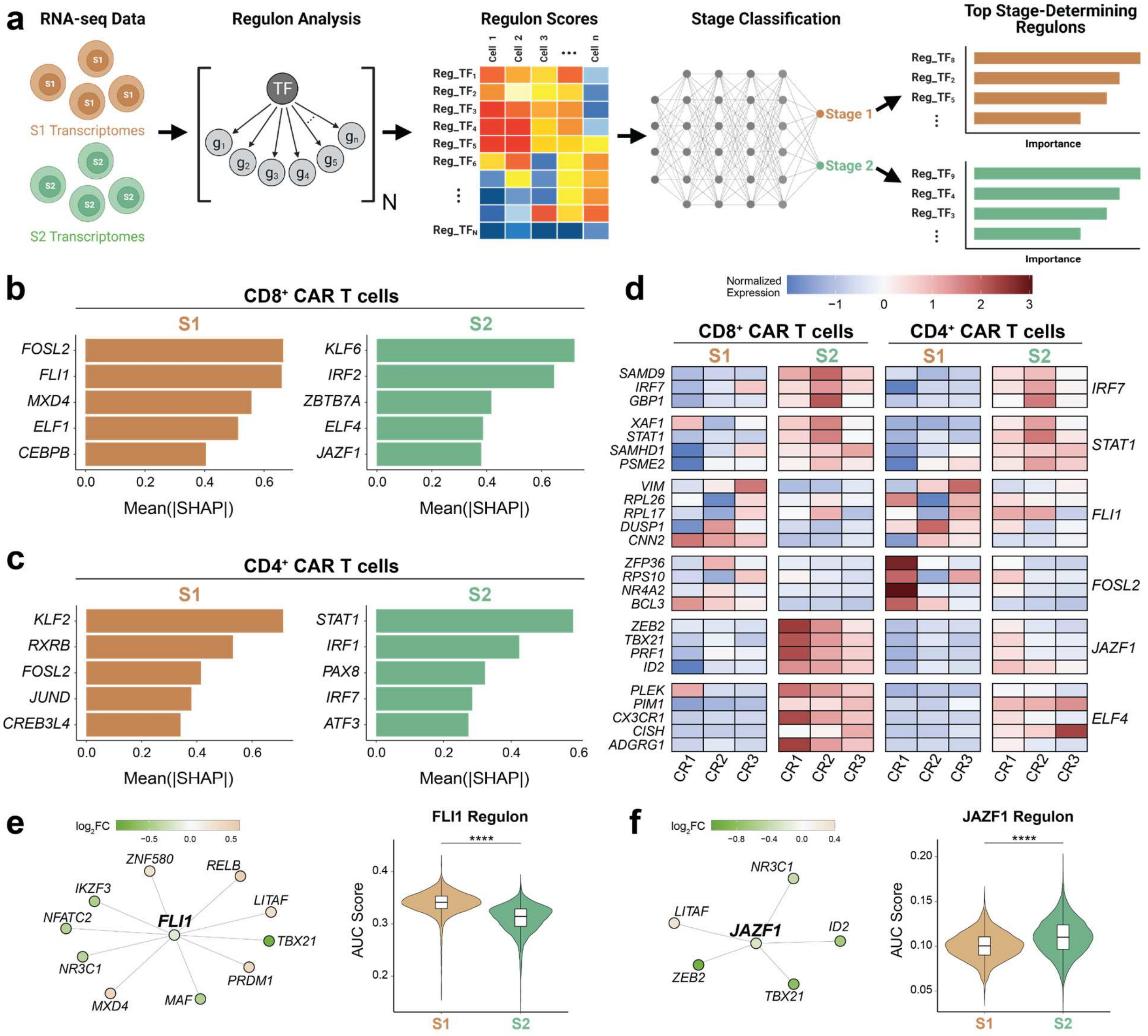

Figure IV-4. Transcriptional regulation of S1 and S2 CAR T cells. (a) Schematic for regulon construction and stage classification in S1 and S2 CAR T cells.

Figure IV-4, continued. After transcriptomes were transformed into regulomes, regulon scores were calculated and used to train a machine-learning model to classify S1/S2 CAR T cells. Key regulons were then determined based on their importance in the model's predictions. (b,c) Top five regulons that delineate S1 and S2 predictions in CD8$^+$ (b) and CD4$^+$ (c) CAR T cells. Each bar graph depicts the SHAP values of the top 5 regulons for that group. (d) Heatmap depicting expression of select genes (listed on left) along with the regulons they are part of (listed on right). (e,f) Representative target networks for the FLI1 (e) and JAZF1 (f) regulons, which help classify S1 and S2 CD8$^+$ CAR T cells respectively. Expression of each regulon among S1 and S2 CD8$^+$ CAR T cells is depicted as violin plots, and were compared by Wilcoxon Rank-Sum test, whereby **** indicates $p<0.0001$. Abbreviations: SHAP, Shapley additive explanations. Associated with Figures IV-S10 and IV-S11.

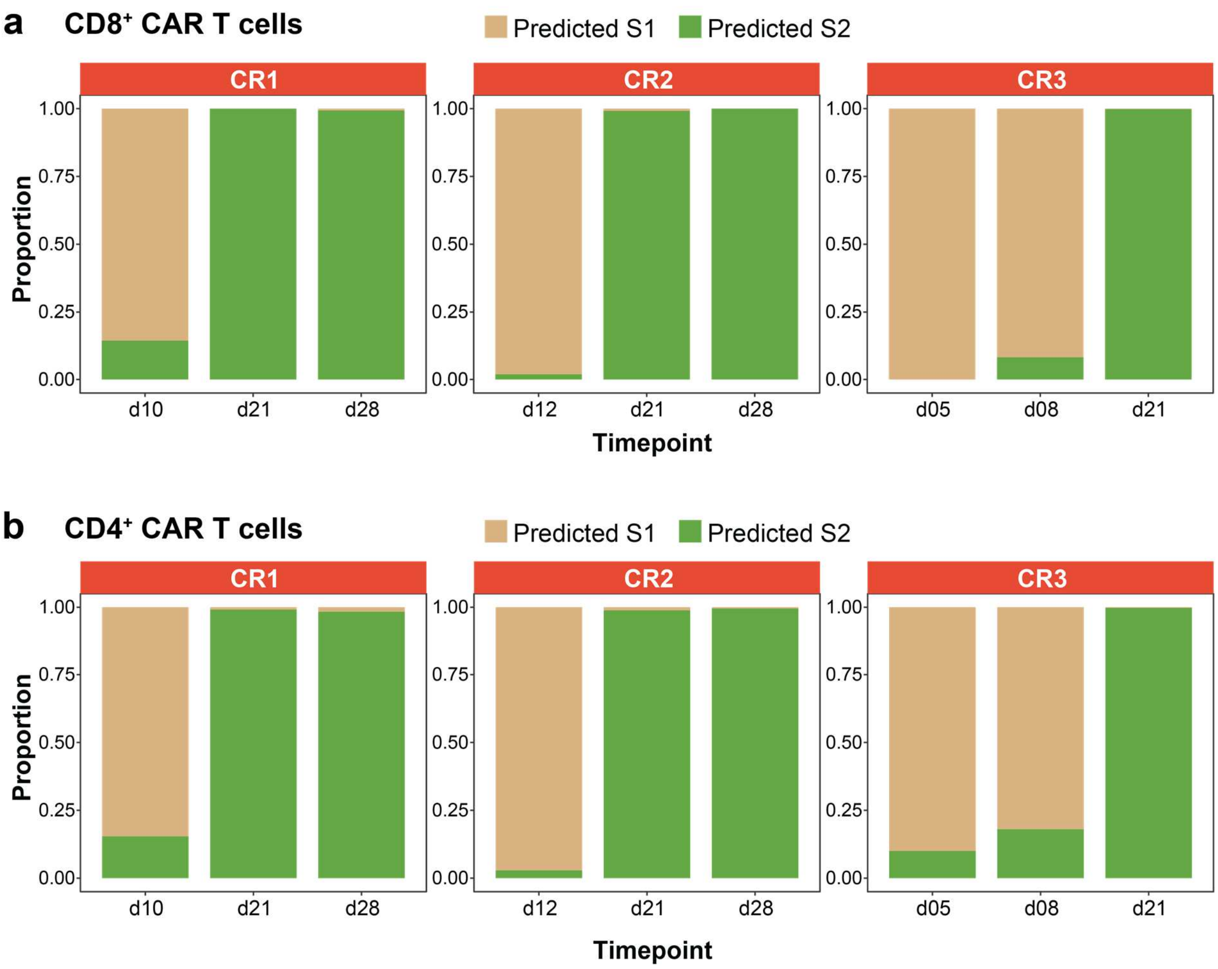

Figure IV-S10. Stage predictions from regulon-based machine-learning model. Stacked bar graphs indicating the proportions of CD8$^+$ (a) and CD4$^+$ (b) CAR T cells predicted to derive from the S1 or S2 clonal expansion wave. Actual timepoints are labeled on the bottom of each graph. Predictions from the model were based on regulon expression transformed from single-cell transcriptomes. Associated with Figure IV-4.

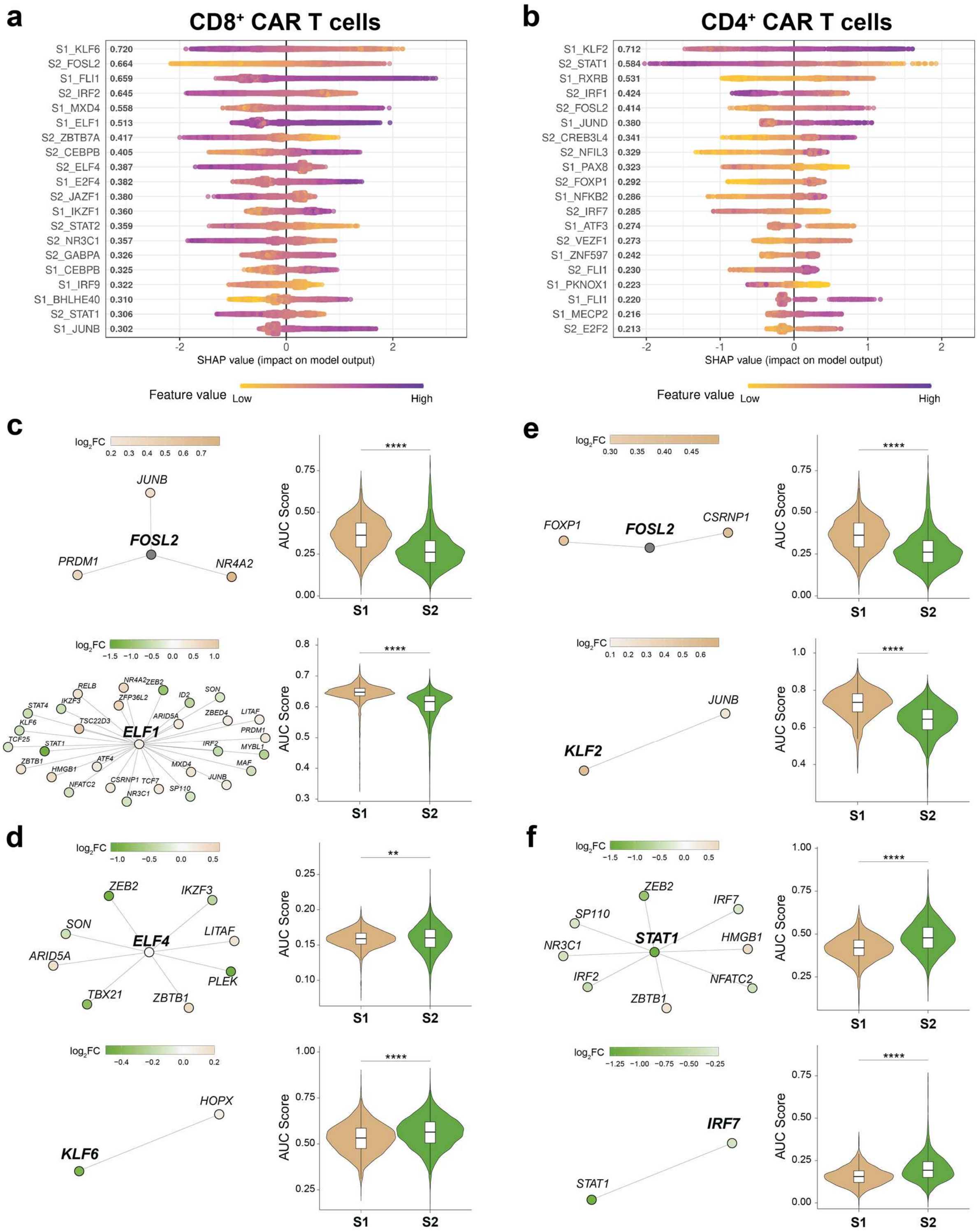

Figure IV-S11. Top stage-determining regulons based on machine-learning model. (a,b) Dot plots indicating SHAP values (x-axis) and direction of prediction (color) for each regulon's influence on predictions for single cells. Plots are depicted for CD8⁺ (a) and CD4⁺ (b) CAR T cells. (c-f) Representative target networks for regulons that help classify S1 CD8⁺ (c), S2 CD8⁺ (d), S1 CD4⁺ (e), and S2 CD4⁺ (f) CAR T cells.

Figure IV-S11, continued. Expression of each regulon among S1 and S2 CAR T cells is depicted as violin plots, and were compared by Wilcoxon Rank-Sum test, whereby **** indicates $p<0.0001$. Abbreviations: SHAP, Shapley additive explanations. Associated with Figure IV-4.

Infusion product precursors of S1 and S2 CD8$^+$ CAR T cells.

Our findings on the clonal dynamics, phenotypes, and regulatory networks underlying S1 and S2 CAR T cells led us to finally hypothesize that S1 and S2 CAR T cells originate from different precursors in the infusion product. We tested this hypothesis on CD8$^+$ CAR T cells because our dataset contained significantly fewer post-infusion CD4$^+$ CAR T cells for reliable analyses. As limited cell numbers precluded directly linking infusion product and post-infusion CAR T cells by TCR clonotypes, we instead employed trajectory analysis to order cells by pseudotime.

We identified three T-cell clusters from the transcriptomes of infusion product CD8$^+$ CAR T cells (**Figure IV-5A**): proliferative (*MKI67*$^+$*TOP2A*$^+$), effector-like (EFF, *GZMB*^{hi}*GNLY*$^+$*TCF7*$^-$), and memory-like (MEM, *GZMB*^{lo}*LEF1*$^+$*CCR7*$^+$*TCF7*$^+$) (**Figure IV-5B**, expanded marker set in figure IV-S12A). The clusters were not patient-specific (figure IV-S12B). We aggregated all infusion product and post-infusion CAR T cells onto the same UMAP, and transferred the previously adopted CD8$^+$ CAR T-cell cluster labels (PEX, MEM, EFF, proliferative, and apoptotic) (**Figure IV-5C**). Infusion product and post-infusion cells occupied the lower and upper lobes of the UMAP, respectively. Moreover, with each successive timepoint (from day 5 to day 90), the gene expression profiles moved increasingly towards the upper lobe on the UMAP (figure IV-S12C). Using trajectory analysis, we identified three distinct differentiation trajectories (**Figure IV-5D**) accounting for S1 PEX, S2 EFF, and S2 MEM CAR T cells. Progression of pseudotime along these trajectories was concordant with real time (**Figure IV-5E**, figure IV-S12C). S1 precursors were enriched in the proliferative phenotype (**Figure IV-5F**), which is consistent with both occurrence of peak expansion during S1 and the correlation between more proliferative infusion products and complete responders.[39] S2 precursors were enriched in the EFF and MEM phenotypes. We then compared the transcriptional profiles of S1 and S2 precursors via GSEA

(**Figure IV-5G**). S1 precursors upregulated gene sets for cell cycling, cell division, and oxidative phosphorylation, while S2 precursors upregulated gene sets for naïve-like T cells and response to interferon signaling. GSEA findings are consistent with the phenotypic compositions of S1 (proliferative) and S2 precursors (EFF, MEM).

In conclusion, trajectory analyses support our hypothesis that S1 and S2 CD8$^+$ CAR T cells differ in their infusion product precursors. Integrating these findings with the two-stage differentiation model paints a comprehensive picture of CD8$^+$ CAR T cells over the entire course of therapy (**Figure IV-5H**). CD8$^+$ CAR T cells begin as proliferative, EFF, or MEM T cells in the infusion product. Following infusion into the patient, the proliferative subset rapidly expands during S1 (pre-day 14), adopting functional and cytotoxic precursor-exhausted phenotypes. Peak expansion, lymphoma infiltration[176], CRS (begins ~day 2)[4], and ICANS (begins ~day 5)[4] all coincide with the S1 timeframe, suggesting that these CAR T cells mediate both tumor clearance and short-term side effects. Subsequently, these short-lived CAR T cells rapidly diminish as the EFF and MEM subsets from the infusion product expand during S2 (post-day 14). These new and longer-lived CAR T cells adopt more memory-like characteristics *in vivo*.

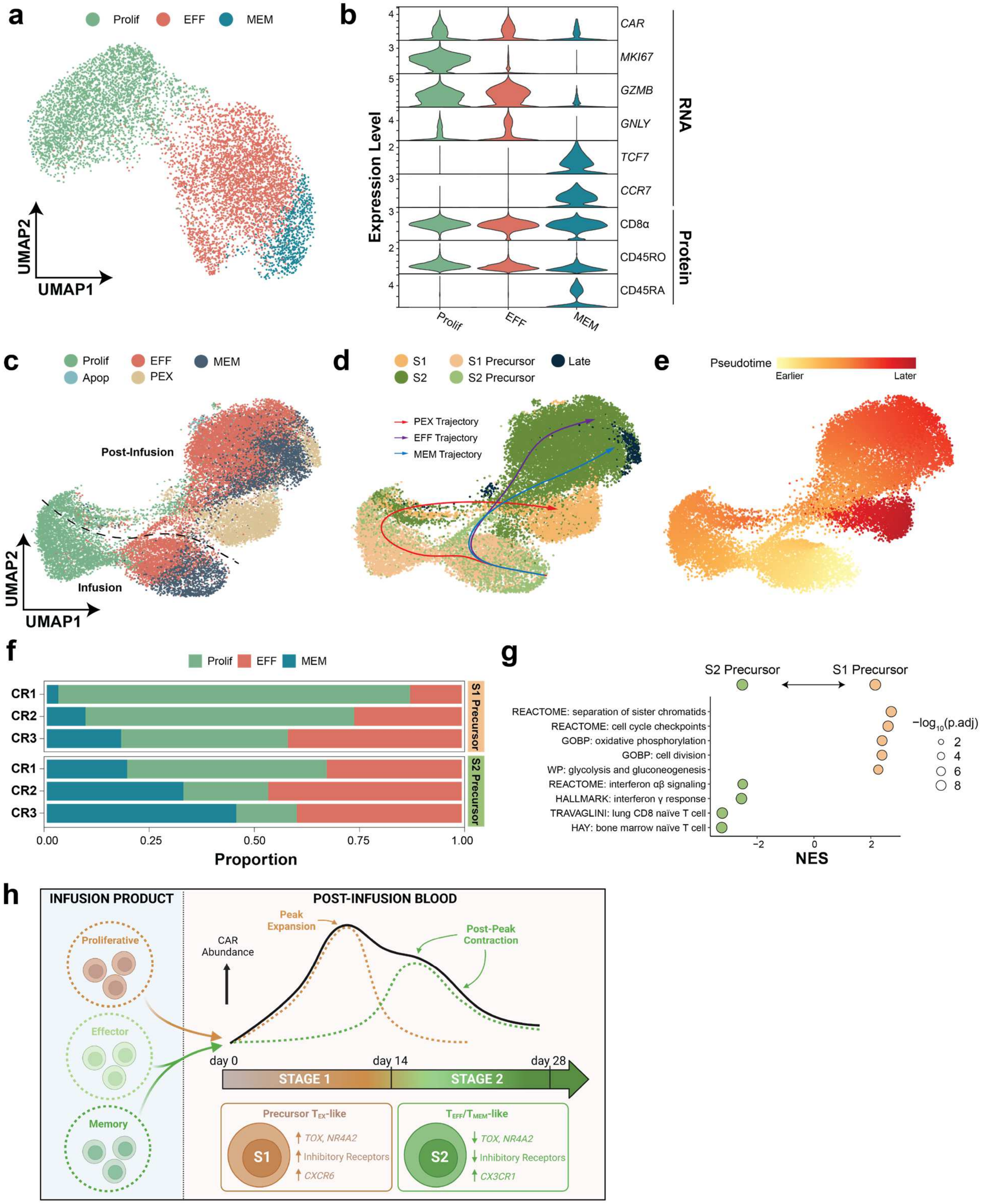

Figure IV-5. Infusion product precursors of post-infusion CD8$^+$ CAR T cells. (a) UMAP depicting single-cell transcriptomes of infusion product CD8$^+$ CAR T cells from CR patients in proliferating, effector-like, and memory-like T-cell clusters.

Figure IV-5, continued. (b) Violin plots depicting normalized expression levels of key genes and proteins for annotation and phenotyping. For extended version, see figure S13a. (c-e) UMAPs depicting single-cell transcriptomes from both infusion product and post-infusion CD8$^+$ CAR T cells. The UMAP is colored by T-cell clusters (c, dashed line delineates infusion product and post-infusion CAR T cells), timepoints with differentiation trajectories (d), and pseudotime (e). (f) Stacked bar graphs depicting proportion represented within each infusion product phenotype by S1 precursors (top) and S2 precursors (bottom) from each CR patient (labeled on left). (g) Gene set enrichment analysis comparing S1 precursors and S2 precursors. For each gene set, direction and statistical significance of enrichment are indicated by the circle's color and size respectively. (h) Cartoon depicting a comprehensive picture of CD8$^+$ CAR T cells over the entire course of therapy, from infusion product precursors to post-infusion S1 and S2 CAR T cells. Abbreviations: EFF, effector-like; PEX, precursor exhausted-like; MEM, memory-like; NES, normalized enrichment score. Associated with Figure IV-S12.

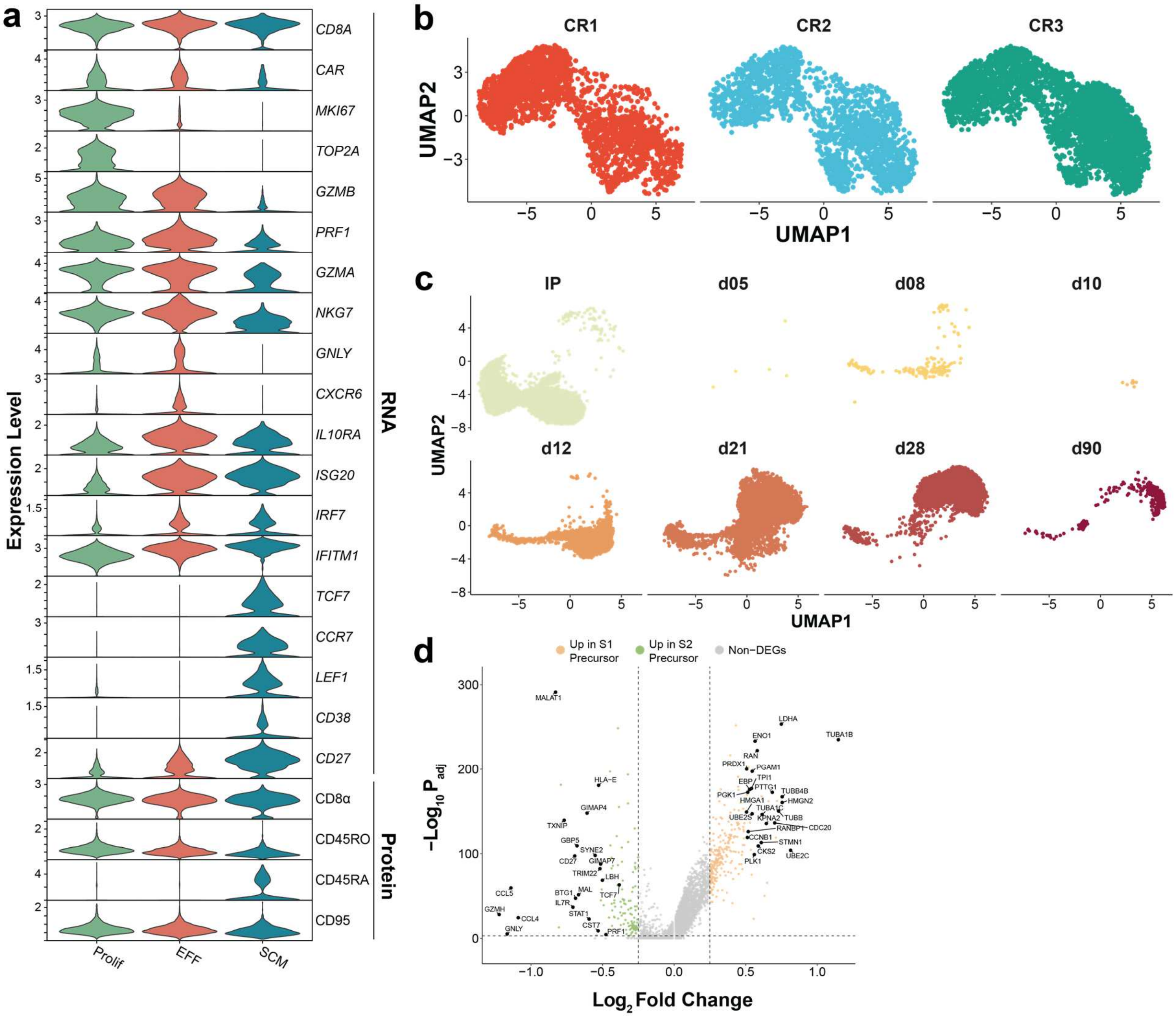

Figure IV-S12. Heterogeneity of infusion product and post-infusion CD8$^+$ CAR T cells. (a) Violin plots depicting normalized expression levels of key genes and proteins among the 3 CD8$^+$ infusion product CAR T-cell clusters.

Figure IV-S12, continued. (b) Colored UMAPs depicting how $CD8^+$ infusion product CAR T cells from each patient are distributed on the overall harmonized UMAP. (c) Colored UMAPs depicting distribution of infusion product and post-infusion $CD8^+$ CAR T cells aggregated from all three patients among different timepoints. (d) Volcano plot depicting log fold-change and adjusted p-value of differentially expressed genes in S1 precursors versus S2 precursors. Key genes are marked accordingly. Associated with Figure IV-5.

III: Discussion

In this study, we investigated CD28-costimulated CAR T-cell differentiation *in vivo* via single-cell, multi-omics, and longitudinal analyses of CAR T cells from patients with r/r DLBCL. Our conclusions are summarized in our two-stage model for CAR T-cell differentiation. According to our model, CAR T cells undergo two distinct clonal expansion stages (S1 and S2), each of which is dominated by unique CAR T-cell phenotypes. S1 is dominated by precursor exhausted-like $CD8^+$ and effector-T_h1-like $CD4^+$ CAR T cells, while S2 is dominated by effector-like $CD8^+$, memory-like $CD8^+$, and memory-like $CD4^+$ CAR T cells. Clonal tracing and T-cell phenotypes suggested that the more expansive S1 CAR T cells are a distinct lineage from the more persistent S2 CAR T cells, biologically uncoupling CAR T cells from peak expansion and post-peak contraction. Using regulon analysis and machine-learning predictions, we identified transcription factors and regulatory networks underlying S1 (including *FOSL1*, *FLI1*, and *ELF1* for $CD8^+$ CAR T cells, and *KLF2* for $CD4^+$ CAR T cells) and S2 (*KLF6*, *JAZF1*, and *ELF4* for $CD8^+$ CAR T cells, and *STAT1*, *IRF1*, and *IRF7* for $CD4^+$ CAR T cells) phenotypes. Finally, trajectory analysis suggested that S1 and S2 $CD8^+$ CAR T cells originate from proliferative and effector/memory-like precursors, respectively, in the infusion product, suggesting that baseline heterogeneity underlies the two stages of clonal expansion. Although limited by the size of our study set and unknowns regarding $CD4^+$ CAR T-cell precursors, our analyses also suggest that *in vivo* CAR T-cell differentiation may be controlled by altering the phenotypic composition of the infusion product.

Although two-stage differentiation is a new phenomenon that has not been reported in the literature, the various elements of our two-stage differentiation model are consistent with the field's current understanding. Previous studies on 4-1BB-costimulated CAR T-cell differentiation have described bursts of CAR T-cell clonal expansion leading to significant changes in the CAR T-cell clonal repertoire over time.[148,177] Our study not only generalizes this observation to CD28-costimulated CARs, but also pairs changes in the clonal repertoire with changes in T-cell phenotypes. Furthermore, CAR T-cell clones with memory-like phenotypes that exhibit delayed expansion after infusion have been reported[47], which supports the validity of the delayed S2 wave in our two-stage differentiation model. Finally, the S1-and S2-specific phenotypes described in our model are consistent with prior phenotyping studies.[153,178,179] Hence, our findings are compatible with existing studies. By integrating our findings from multiple data modalities with established studies in the CAR T-cell field, we form a more granular and cohesive two-stage model for *in vivo* CD28-costimulated CAR T-cell differentiation.

One noteworthy consequence of the two-stage differentiation model is that CD28-costimulated CAR T cells from peak expansion and post-peak contraction are biologically uncoupled. This uncoupling significantly informs how we understand CAR T-cell expansion and persistence. Expansion facilitates tumor clearance at the cost of CRS and ICANS[4,23], while persistence facilitates long-term immunosurveillance at the cost of B-cell aplasia and hypogammaglobulinemia.[144–146] Our findings suggest that expansion and persistence, both of which serve important clinical purposes, are actually mediated by distinct CAR T-cell populations. Effective and personalized CAR T-cell therapies balance expansion and persistence, taking into consideration each patient's tumor burden, tolerance for side effects, and risk of relapse. Our findings suggest that expansion and persistence may be independently tuned to meet a patient's needs. In support of this possibility, our analyses identified key S1- and S2-specific regulatory targets that may be manipulated. Furthermore, our findings suggest that engineering CAR T cells that simultaneously expand and persist competently may be difficult since these characteristics originate from distinct CAR T-cell populations *in vivo*.

In addition to clonal kinetics and phenotypic heterogeneity, we characterized S1- and S2-specific upregulation of TNFα and IFN-I response genes, respectively. As TNFα-secreting CD8$^+$ CAR T cells are a predictor of complete responders[149], TNFα may be signaling in an autocrine manner during S1. On the other hand, upregulation of IFN-I response genes during S2 was unexpected. Although IFN-I response signatures in the apheresis of patients with B-cell acute lymphoblastic leukemia predicts poor CAR T-cell persistence[180], IFN-I may also enhance CAR T-cell *in vivo* efficacy.[181] Hence, the roles of IFN-I are likely complex or time-dependent, which is supported by our finding that IFN-I response signatures are S2-specific.

Finally, we concluded our study by linking S1 and S2 CD8$^+$ CAR T cells with proliferative or effector/memory-like infusion product precursors, respectively. Importantly, this finding suggests that the existence or magnitude of the S1 and S2 waves can be changed by manipulating the relative quantities of their precursors in the infusion product. However, we cannot rule out the likely possibility that the *in vivo* peripheral blood environment of a patient with DLBCL may also play an instrumental role in determining whether a CAR T cell clonally expands during S1 or S2. Future studies can explore this possibility by analyzing interactions between CAR T cells and other blood cells (such as myeloid cells, B cells, NK cells) at S1 and S2.

Findings from the current study are based upon CD28-costimulated CAR T cells from complete responders. However, two-stage differentiation may be universally true in other settings. Others forms of adoptive cell therapy (such as those using 4-1BB-costimulated CARs) may follow a general two-stage differentiation strategy *in vivo*. Different forms of adoptive cell therapy may exhibit different S1 and S2 temporal dynamics or favor one wave over the other. Importantly, two-stage differentiation may be aberrant in non-responders. Future studies should investigate the differences in temporal dynamics, phenotypes, or major regulons at each stage in these alternative treatment settings.

While this current study represents a significant advancement for the CAR T-cell therapy field, we acknowledge three important technical limitations. Firstly, our study is based on a limited study set (3 complete responders). While this number is comparable to the sizes of study sets from existing studies[47,148,179], our findings may require external validation. To ameliorate this issue, we contextualized our findings with existing literature as much as possible. Secondly, our regulon and trajectory analyses are inferential in nature, requiring future experiments to definitively demonstrate their conclusions. Thirdly, our single-cell dataset is limited by low input cell numbers, which decreases the resolution of TCR repertoire analyses. Future studies can reinforce our findings with ensemble-level TCR repertoire analysis of greater cell numbers.

IV: Methods

Generation of CD19-tetramers.

Tetramers[154] were constructed from AviTag-biotinylated human His-tagged CD19 (Acro Biosystems, CD9-H82E9) and Alexa Fluor 647-labeled streptavidin (BioLegend, 405237). Biotinylated CD19 was added to the tetrameric streptavidin at a 4:1 molar ratio for 30 minutes at 4°C in the dark. This mixture was diluted with PBS to convenient concentrations for staining. Quality control was performed on each batch of biotinylated CD19 by generating corresponding CD19-tetramers for staining anti-CD19 CAR-transduced Jurkat T cells.

Single-cell omics assays.

Patient peripheral blood mononuclear cells were collected from blood biospecimens by Ficoll-Paque PLUS (Cytiva, 95021-205) and stored in freezing media (RPMI, 10% FBS, 10% DMSO). Residual infusion product cells were collected from the patient's spent infusion product bag and stored in CELLBANKER 1 (Amsbio, 11888). All cells were cryopreserved in liquid-phase nitrogen.

Cryopreserved biospecimens were thawed (RPMI, 10% FBS) and washed with cold FACS buffer (PBS, 2% BSA, 0.05% sodium azide). Fc receptors were blocked with Human TruStain FcX (BioLegend, 422301) at 1:50 dilution for 5 minutes at 4°C. Then, cells were incubated for 30 minutes at 4°C in the dark with a staining solution containing CITE-seq antibodies (described below), BV421-labeled anti-CD3ε (clone SK7, BioLegend, 344833), and AF647-labeled CD19-tetramers (3 nM final concentration) for CAR T-cell phenotyping and detection. Subsequently, stained cells were conjugated with LIVE/DEAD Fixable Near-IR viability dye (Invitrogen, L34975) at 1:1000 dilution in PBS for 5 minutes at room temperature. Finally, cells were washed three times in cold cell media (RPMI, 10% FBS) before fluorescence-activated cell sorting (BD Biosciences, FACSAria Fusion). CAR^+ sorting gates were drawn based on fluorescence of PBMCs from a similarly stained healthy donor.

Sorted endogenous T cells ($CD3^+CAR^-$) and CAR T cells ($CD3^+CAR^+$) were separately partitioned into droplets for single-cell omics assays via Chromium Next GEM Single-Cell 5'Kit v2 (10x Genomics, 1000263). RNA-seq libraries were prepared according to manufacturer protocols. CITE-seq libraries were prepared via the 5' Feature Barcode Kit (10x Genomics, 1000256). TCR-seq libraries were prepared via the Chromium Single-Cell Human TCR Amplification Kit (10x Genomics, 1000252). All libraries (RNA-seq, CITE-seq, TCR-seq) were quantified via the Qubit dsDNA HS Assay Kit (Invitrogen, Q32851), quality-checked for fragment sizes via high-sensitivity D5000 screentapes (Agilent, 5067-5592), pooled, and sequenced (Illumina, Novaseq-6000 and Nextseq-550).

CITE-seq antibody preparation.

31 human “Cellular Indexing of Transcriptomes and Epitopes by Sequencing” (CITE-seq[182]) antibodies were obtained from BioLegend (TotalSeq-C reagents): anti-CD3ε (clone UCHT1, 300479), anti-CD5 (clone UCHT2, 300637), anti-TCRα/β (clone IP26, 306743), anti-TCRγ/δ (clone B1, 331231), anti-CD4 (clone SK3, 344651), anti-CD8α (clone SK1, 344753), anti-CD45RA (clone HI100, 304163), anti-CD45RO (clone UCHL1, 304259), anti-CCR7 (clone G043H7, 353251), anti-CD95 (clone DX2, 305651), anti-CD57 (clone QA17A04, 393321), anti-CD25 (clone BC96, 302649), anti-CD127 (clone A019D5, 351356), anti-CD103 (clone Ber-ACT8, 350233), anti-CXCR3 (clone G025H7, 353747), anti-CCR4 (clone L291H4, 359425), anti-CCR6 (clone

G034E3, 353440), anti-PD-1 (clone EH12.2H7, 329963), anti-TIM-3 (clone F38-2E2, 345049), anti-LAG-3 (clone 11C3C65, 369335), anti-CD39 (clone A1, 328237), anti-TIGIT (clone A15153G, 372729), anti-CD27 (clone O323, 302853), anti-CD40L (clone 24-31, 310849), anti-GITR (clone 108-17, 371227), anti-OX40 (clone Ber-ACT35, 350035), anti-4-1BB (clone 4B4-1, 309839), anti-CD28 (clone CD28.2, 302963), mouse IgG1-κ isotype control (clone MOPC-21, 400187), mouse IgG2a-κ isotype control (clone MOPC-173, 400293), and mouse IgG2b-κ isotype control (clone MPC-11, 400381). Residual infusion product cells were stained with all 31 CITE-seq antibodies. Patient peripheral blood mononuclear cells were stained with all CITE-seq antibodies minus anti-CD3ε (30 in total) because T cells sorted from these samples were stained with BV421-labeled anti-CD3ε. To prepare the CITE-seq staining solution, the antibody pool was constructed and centrifuged at 14000 × *g* for 10 minutes at room temperature in FACS buffer (PBS, 2% BSA, 0.05% sodium azide) to remove aggregates. The antibody supernatant was extracted and diluted with fresh FACS buffer to appropriate staining concentrations.

Single-cell RNA-seq data processing.

The RNA-seq and paired CITE-seq reads were aligned to the GRCh38 reference genome, which was modified with the CAR transgene sequence used in axicabtagene ciloleucel, and quantified using the *cellranger count* (10x Genomics, version 6.0.0).[183] The filtered gene/feature-barcode matrices that contained only barcodes with unique molecular identifier (UMI) counts that passed the quality control were used for downstream analyses. We obtained a total of 32,741 cells from 13 samples with on average 97,036 reads per cell and a median of 1979 genes per cell.

UMAP analysis and clustering on single-cell RNA-seq data.

UMAP analysis and clustering were performed using the Seurat package (Version 4.0.5).[184] Raw count matrices were first converted to Seurat objects before being further merged into one Seurat object, with protein expression added as the ADT assay. Following that, cells with <300 genes detected or >10% mitochondrial RNA content were excluded from further analysis. 32,346 cells were retained after filtering.

Then, the raw count was log-normalized using the *NormalizeData* function with default options. Top 5,000 variable features were then identified using the *FindVariableFeatures* function with the default “vst” method. The data were then centered and scaled using the *ScaleData* function, with additional regression against 1) the percent of mitochondrial RNA content and 2) difference in cell cycle S-phase score and G2M-phase score. Scaled data were then used as input for principal component analysis (PCA) based on variable genes using the *RunPCA* function. Data harmonization to remove patient-specific effects was then performed on the principal components using the Harmony package (Version 1.0) through the *RunHarmony* function.[143] Next, UMAP was constructed based on the first 50 harmony components, with “n.neighbors=30” and “min.dist=0.3” in most cases, and “n.neighbors=50” and “min.dist=0.5” in Figure 5. The same harmony components were then used to construct the shared nearest neighbor (SNN) graph using the *FindNeighbors* function, which was then partitioned to identify clusters using the *FindClusters* function with default Louvain algorithm and “resolution = 0.8” in most cases. These clusters were then manually aggregated and classified as T-cell subsets based on known markers. CD8 and CD4 T-cell classification were done based on both gene and protein expression of CD4, CD8α, and CD8β.

For subset analysis, the corresponding subset were extracted from the master Seurat object using the *subset* function. The above detailed preprocessing steps were repeated to generate the corresponding UMAP and subset annotations.

Differential gene expression (DEG) analysis on single-cell RNA-seq data.

DEG analyses were all performed using the *FindMarkers* function in Seurat package, with default parameters and the appropriate ‘ident.1” and “ident.2” set as contrast. Unless otherwise stated, the results were then filtered with p_val_adj < 0.05 and abs(avg_logFC) > 0.25.

GSEA and pathway enrichment analysis.

Gene Set Enrichment Analysis (GSEA) and pathway enrichment analysis were done using the clusterProfiler (version 3.16.1)[185] package based on the msigdb database built in msigdbr package (version 7.4.1).[186]

Regulon analysis.

To construct regulons in a specific cell subset, we first extracted the raw count matrix of that subset. Then, we supplied it as input for the pySCENIC package (version 0.10.4) and ran through the workflow as detailed in its documentation and publication.[187,188] More specifically, the base script was adapted from the "PBMC10K" example script on the pyScenic website.[189] In addition, the arboreto component was used to speed up analysis. Each resultant regulon is a gene list with a central TF and all its putative target genes determined through the SCENIC algorithm, and each set of regulons is sample/subset-specific and represent putative regulatory unit in that specific sample/subset.

Regulon or general gene set signature scoring.

Individual cells were scored using the AUCell package (version 1.10.0)[187] for a particular gene set from the msidb database or from a single-cell-derived regulon as follows. The normalized gene expression was first used as input into the *AUCell_buildRankings* function to score each cell for gene set enrichment and to build a ranking matrix. The signature score was then calculated as an AUC score using the *AUCell_calcAUC* function with all default parameters.

Machine learning classification on regulon scores.

To classify any two subsets of T cells (e.g., S1 CD8$^+$ T cells and S2 CD8$^+$ T cells), we first built a regulon set for each subset independently. Then, we merged all regulon sets into a master regulon set. We then calculated the regulon scores using the master regulon set for all cells from the two subsets, resulting in a regulon score matrix of cell by regulon. Each cell would then serve as an observation and each regulon as a feature for machine learning. In the case of fate prediction/tracing, we built regulons for both the two descendent subsets and the progenitor subset and use the union as the master regulon set. This allowed us to incorporate any changes in regulatory module from the progenitor cells to the descendants.

The machine learning classification models were built in the caret framework using the caret package (version 6.0-90).[190] Briefly, we divided the input data into training (75%), validation (15%), test sets (10%), and then we trained and optimized xgboost models[191] through grid hyperparameter search and with a 5-fold cross-validation until reaching a best accuracy of >85% (refer to figures for specific accuracies).

We then interrogated the final models for feature importance evaluation using the Shapley Additive Explanation (SHAP) method[192] implemented in the SHAPforxgboost package(version 0.1.1).[193] In the case of fate prediction/tracing, we then applied the final models on the progenitor subset to predict the descendent fate of each progenitor cell, assigning it as the respective precursor cell.

RNA velocity and trajectory analysis.

RNA velocity analyses were done using the scVelo package (version 0.2.2)[194], adapting the tutorial script from the scVelo website.[195] Briefly, spliced and unspliced reads were marked from the mapped sequencing data by velocyto package (version 0.17.17).[196] The results, along with the gene expression and sample metadata, were assembled into an anndata object via scanpy (version 1.6.0).[197] RNA velocity was then estimated with dynamic modelling through scVelo, and the results were visualized through grid embedding on the UMAP. Cell trajectories were then constructed in a semi-supervised manner using the slingshot package (version 1.6.1).[198] Besides taking into account the RNA velocity embedding, the starting clusters were chosen to be from the infusion product during the trajectory construction.

Single-cell TCR-seq data processing and analysis.

The TCR-seq reads from each sample were aligned to the 10x curated GRCh38 vdj reference genome and quantified using the cellranger vdj (10x Genomics, version 6.0.0). The results were then aggregated using the cellranger aggr function, with the source patient (donor) and timepoint (origin) of each sample supplied in the metadata to guide the clonotype assignment. The resultant clonotype and filtered contig annotation data were used for downstream analyses. Each unique clonotype is defined by the nucleotide sequence of CDR3 regions for paired productive TCRα and TCRβ chains. TCR clonality overlap and tracing analyses were done using the immunarch package (version 0.6.7).[199]

When linking the TCR clonotype to the corresponding cell phenotype, we keep only data with matching cell barcodes from both the TCR-seq and RNA-seq data. Where necessary, the frequency of each clonotype in each sample was recalculated based on those successfully matched to the corresponding RNA data.

CAR transgene mapping.

The axicabtagene ciloleucel CAR design is documented.[65] Its sequence was confirmed by Sanger sequencing of genomic DNA extracted from axicabtagene ciloleucel infusion products. The CAR sequence was then added to the GRCh38 FASTA and GTF files accordingly. A custom reference for cellranger was built from these annotation files using cellranger mkref (10x Genomics, version 6.0.0). The resultant custom reference was used for the CAR transgene mapping through cellranger count.

V: Acknowledgements

We thank Phi Beta Psi, the Ullman Fund in Cancer Immunology, the Hoogland Lymphoma Research Pilot Projects, Chicago Immunoengineering Innovation Center, and NIH New Innovator award (1DP2AI144245) for financial support (to J.H.). Y.H. was supported by the University of Chicago MSTP Training Grant (T32GM007281). This project was supported by the National Center for Advancing Translational Sciences of the National Institutes of Health through Grant Number 5UL1TR002389-02 that funds the Institute for Translational Medicine. We thank the UChicago Human Immunologic Monitoring Facility for patient biospecimen cryopreservation, as well as the Pritzker School of Molecular Engineering Single-Cell Immunophenotyping Core and UChicago Genomics Facility for instrumentation to generate single-cell sequencing data. The authors thank Dr. Karen M. Watters for scientific editing of the manuscript.

VI: Contributions

Guoshuai Cao[1,#], Yifei Hu[1,2,#], Thomas Althaus[6], Peter A. Riedell[4,5,6], Michael R. Bishop[5,6], Justin P. Kline[3,4,5,6], Jun Huang[1,3,4,*]

[1]Pritzker School of Molecular Engineering, University of Chicago, Chicago, IL 60637, USA

[2]Pritzker School of Medicine, University of Chicago, Chicago, IL 60637, USA

[3]Committee on Immunology, University of Chicago, Chicago, IL 60637, USA

[4]Committee on Cancer Biology, University of Chicago, Chicago, IL 60637, USA

[5]Department of Medicine, University of Chicago, Chicago, IL 60637, USA

[6]The David and Etta Jonas Center for Cellular Therapy, University of Chicago, Chicago, IL 60637, USA

[#]These authors contributed equally.

Y.H., G.C., J.K., and J.H. conceived and designed all experiments. J.H. supervised the project. T.A., P.R., and M.B. coordinated patient biospecimens for these studies. Y.H. sorted CAR T cells and generated data for single-cell omics. G.C. performed single-cell omics and machine-learning analyses. G.C. and Y.H. jointly interpreted the data. Y.H. and G.C. prepared while J.H. and J.K. edited the manuscript. P.R. and M.B. reviewed the manuscript.

SECTION V: TYPE I INTERFERONS FOR ENHANCING CAR T-CELL EFFICACY

Chimeric antigen receptor (CAR) T-cell therapy has expanded therapeutic options for patients with diffuse large B-cell lymphoma (DLBCL). Despite ~40% complete response rates, efficacy is limited by significant non-response rates. Here, we demonstrate that type I interferons are promising cytokines for increasing the efficacy of CAR T cells *in vitro*. Interferon-treated CAR T cells exhibited a more memory-like phenotype, characterized by enrichment of $CD8^+$ stem cell memory ($CD45RA^+CCR7^+$) and $CD4^+$ ($CD45RA^+CCR7^-$) central memory phenotypes. Furthermore, upon engagement with antigen-expressing target cells, interferon-treated CAR T cells increased cytotoxicity, polyfunctional cytokine secretion, and proliferation. In sum, our promising *in vitro* findings suggest that interferon-treatment may increase CAR T-cell *in vivo* efficacy, leading to a new and easily implemented solution to decrease CAR T-cell therapy non-response rates.

I: Introduction

Efforts to develop improved CAR T-cell therapy formulations are underway.[30] Existing studies have aimed to decipher correlates and mechanisms for CAR T-cell therapy non-response.[137] Non-response to CAR T-cell therapy correlates with decreased *in vivo* CAR T-cell persistence[4,5,39] and expansion[4], less polyfunctional cytokine production in the infusion product[23], and signatures of T-cell exhaustion in the infusion product[22,39] or apheresis[149]. More recently, non-response was correlated with *TIGIT* expression on post-infusion CAR T cells. Although anti-TIGIT blockade increased CAR T-cell cytotoxicity and cytokine secretion *in vitro* and boosted survival *in vivo* in a xenograft mouse model, these experiments were performed with target cells constitutively and non-physiologically expressing PVR, the TIGIT ligand.[153] Hence, the relevance of anti-TIGIT blockade for improving CAR T-cell therapy is questionable. In summary, although these studies established biomarkers for clinical response, a clear limitation is the lack translatable directions for improving therapy response rates.

Type I interferons (IFN-Is) are promising cytokines for increasing efficacy and decreasing non-response rates of CAR T-cell therapy. In humans, IFN-I family members, including 13 IFN-α and 2 IFN-β subtypes[200], are secreted upon induction by virus. After secretion, IFN-Is diffuse and subsequently can bind to the IFNAR heterodimeric receptor on T cells and activate transcription factors, such as signal transducer and activator transcription 1 (STAT1), STAT2, and interferon regulatory factor 7 (IRF7) to coordinate expression of genes involved in anti-viral immunity.[160,200] In CD4$^+$ T cells, IFN-I signaling promotes T_h1 polarization[201] while antagonizing T_h2[202] and T_h17[203] polarization. In CD8$^+$ T cells, IFN-I enhances cytotoxic T-cell responses[204] and induces central memory T-cell differentiation.[205] Due to their potent immunomodulatory effects, IFN-I clinical formulations (such as INTRON A) have been used to treat viral infections (e.g. hepatitis, influenza, HIV, and COVID-19)[206,207] and cancer (e.g. leukemias, myelomas, and melanomas).[208] Importantly, the Sadelain group demonstrated that IRF7 supported the effector functions, persistence, and expansion of anti-CD19 CAR T cells.[181] In their xenograft mouse model, *IRF7* knockdown in CAR T cells accelerated tumor progression and reduced overall survival.[181] However, it was still unknown whether the IFN-I/IRF7 pathway was clinically relevant in human patient CAR T cells.

Based on existing studies, we hypothesize that IFN-I signaling affects *in vivo* CAR T-cell differentiation, enhances *in vitro* CAR T-cell effector functions, and improves *in vivo* CAR T-cell efficacy. To test this hypothesis, we will experimentally determine how priming patient CAR T cells with IFN-I affects *in vitro* effector functions and *in vivo* efficacy in xenograft mouse models.

II: Results

IFN-I signaling increases CAR T-cell memory phenotype in vitro*.*

We hypothesized that IFN-I signaling promotes memory CAR T-cell differentiation. To test this hypothesis, we transduced human peripheral blood T cells from independent donors with a CD28-costimulated anti-CD19 CAR (clone FMC63, **Figure V-1A**). CAR T cells were cultured with and without IFN-I for 10 days prior to flow phenotyping for memory T-cell markers (**Figure V-1B**). While IFN-I includes many subtypes, we chose IFN-α2 for these experiments because this subtype is highly potent and clinically used. As expected, IFN-α2 signaling upregulated cytoplasmic expression of the IRF7 transcription factor in both CAR-transduced Jurkat T cells and primary human T cells (**Figure V-1C**). Higher IFN-α2 concentrations caused greater IRF7 upregulation, which saturated at 3000 units/mL. In order to maximize IFN-I signaling in our experiments, we used the saturation concentration to test our hypothesis.

After a 10-day culturing period, CAR T cells were phenotyped for expression of memory markers. Based on CD45RA and CCR7 expression, $CD8^+$ (**Figure V-1D-E**) and $CD4^+$ (**Figure V-1F-G**) CAR T cells were annotated as belonging to the stem cell memory (SCM, $CD45RA^+CCR7^+$), central memory (CM, $CD45RA^-CCR7^+$), effector memory (EM, $CD45RA^-CCR7^-$), or effector memory re-expressing CD45RA (EMRA, $CD45RA^+CCR7^-$) phenotypes. In $CD8^+$ CAR T cells, IFN-α2 signaling enriched the SCM and depleted the EMRA phenotypes (**Figure V-1D**), which was consistent across three independent donors (**Figure V-1E**). In CD4$^+$ CAR T cells, IFN-α2 signaling enriched the CM and depleted the EMRA phenotypes (**Figure V-1F**), which was also consistent across three independent donors (**Figure V-1G**). IFN-α2 signaling upregulated expression of the IL-7 receptor (CD127, a marker for memory T cells), though this did not reach statistical significance (**Figure V-1H**). On the other hand, IFN-α2 signaling downregulated expression of CD57, a marker of terminally differentiated and senescent T cells, in CD8$^+$ CAR T cells (**Figure V-1I**). Finally, we labeled cells with and assayed for accumulation of MitoSpy Orange, a dye that localizes to active mitochondria and measures cell health. IFN-α2 signaling increased MitoSpy Orange accumulation in both CD8$^+$ and CD4$^+$ CAR T cells, though this did not reach statistical significance (**Figure V-1J**).

Overall, our phenotyping results demonstrated that IFN-I signaling during *in vitro* expansion increased the CD8$^+$ SCM and CD4$^+$ CM phenotypes, increased memory marker expression, and decreased T-cell senescence among primary human CAR T cells. These results are consistent with our hypothesis that IFN-I signaling promotes memory CAR T-cell differentiation. Moreover, based on MitoSpy Orange accumulation results, IFN-α2 signaling increases the numbers of active mitochondria, indicating that the CAR T cells' overall viability and resistance to apoptosis have increased. Increased memory differentiation and resistance to apoptosis suggest that IFN-I signaling may increase CAR T-cell persistence *in vivo*.

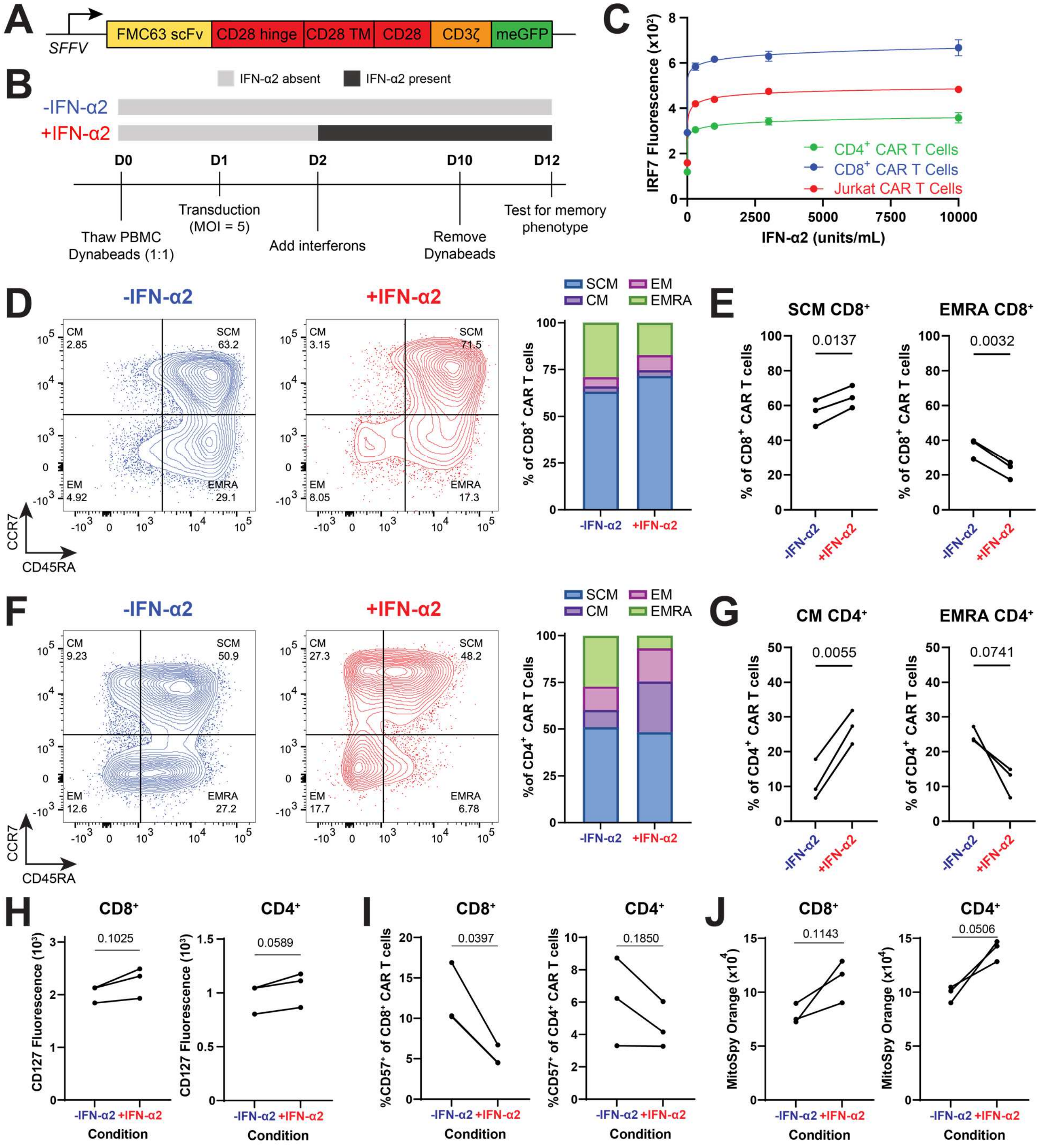

Figure V-1. IFN-I signaling increases CAR T-cell memory phenotype *in vitro*. (A) Design of the CD28-costimulated CAR used to test the influence of IFN-I signaling. (B) Schematic depicting transduction and culturing of CAR T cells in the -IFN-α2 and +IFN-α2 conditions. Cultured CAR T cells were tested at day 12 for their memory phenotype. (C) Titration curves depicting upregulation of cytoplasmic IRF7 with increasing IFN-α2 concentrations. (D, F) Flow plot with summary stacked bar plot depicting memory phenotypes of CD8$^+$ (D) and CD4$^+$ (F) CAR T cells from a representative donor.

Figure V-1, continued. (E, G) Paired dot plots depicting SCM/EMRA or CM/EMRA representation in CD8$^+$ (E) and CD4$^+$ (G) CAR T cells, respectively. Results are representative of 3 independent donors. (H-J) Paired dot plots depicting CD127 expression (H), % CD57$^+$ (I), and MitoSpy Orange staining (J) of CD8$^+$ and CD4$^+$ CAR T cells in the -IFN-α2 and +IFN-α2 conditions. Results are representative of 3 independent donors. All statistical testing in this figure were performed via paired *t*-tests, whereby p-values are indicated. Abbreviations: SCM, stem cell memory; CM, central memory; EM, effector memory; EMRA, effector memory re-expressing CD45RA

IFN-I signaling increases CAR T-cell effector functions* in vitro*.

We hypothesized that IFN-I signaling also promotes CAR T-cell effector functions, including cytotoxicity and cytokine secretion. To test this hypothesis, CAR T cells (generated using peripheral blood T cells from independent donors) were cultured with and without IFN-I for 12 days prior to co-culturing with OCI-Ly8 cells, a CD19$^+$ human DLBCL cell line. OCI-Ly8 cells were transduced with firefly luciferase so that luminescence measures target cell viability after T-cell killing.[209] Cytotoxicity was measured at effector-to-target (E:T) ratios ranging from 3:1 to 1:100. At higher ratios, IFN-α2 signaling increased cytotoxicity (**Figure V-2A**). At lower ratios, no differences were observed, which may result from limitations of the assay's sensitivity. Next, cytokine secretion (IFN-γ, TNF-α, IL-2) was measured by intracellular flow cytometry. In both CD8$^+$ and CD4$^+$ CAR T cells, IFN-α2 signaling enhanced polyfunctionality (IFN-γ$^+$TNF-α$^+$IL-2$^+$) across three independent donors (**Figure V-2B**). Our cytotoxicity and cytokine secretion findings support our hypothesis that IFN-I promotes CAR T-cell effector functions. Furthermore, increased polyfunctionality is correlated with CAR T cells from complete responders.[23] Increased effector functions suggests that IFN-α2 signaling may augment a CAR T cell's ability to control tumors *in vivo*.

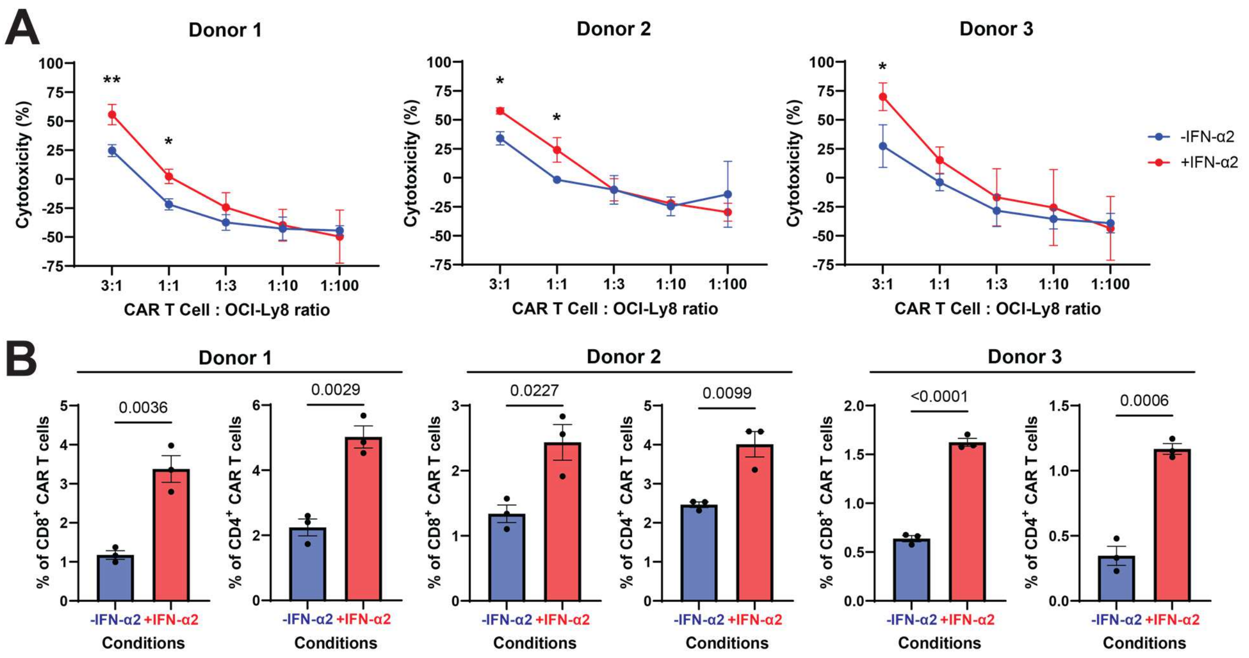

Figure V-2. IFN-I signaling increases CAR T-cell effector functions *in vitro*. (A) Line plot depicting cytotoxicity of CAR T cells upon co-culture with OCI-Ly8 target cells at various effector-to-target ratios (n=3 replicates). Cytotoxicity was compared by mixed 2-way ANOVA and post-hoc *t*-tests, whereby ** denotes $p<0.01$ and * denotes $p<0.05$. (B) Bar graphs depicting percentage of polyfunctional CAR T cells (IFN-γ^+TNF-α^+IL-2^+) as measured by intracellular flow cytometry after co-culture with OCI-Ly8 cells at 1:1 ratio. Percentages were compared by independent *t*-tests (n=3 replicates).

IFN-I signaling increases CAR T-cell proliferation in vitro*.*

Finally, we hypothesized that IFN-I signaling promotes CAR T-cell proliferation. To test this hypothesis, CAR T cells (generated using peripheral blood T cells from independent donors) were cultured with and without IFN-α2. IFN-α2 was removed from the media at various times prior to labeling with CellTrace Violet (CTV). CTV-labeled CAR T cells were then co-cultured with OCI-Ly8 cells for 4 days prior to flow phenotyping for CTV dilution (**Figure V-3A**). After engagement with OCI-Ly8 cells, IFN-α2-treated CD8$^+$ (**Figure V-3B**) and CD4$^+$ (**Figure V-3C**) CAR T cells generally exhibited less CTV fluorescence compared to non-treated controls. The decrease was statistically significant for donors 1 and 3, but not for donor 2. CTV dilution was maximized when IFN-α2 was removed at day 12, hence proliferation was maximized when IFN-α2 was removed two days before antigen engagement. Our findings based on CTV dilution support our hypothesis that IFN-I promotes CAR T-cell proliferation.

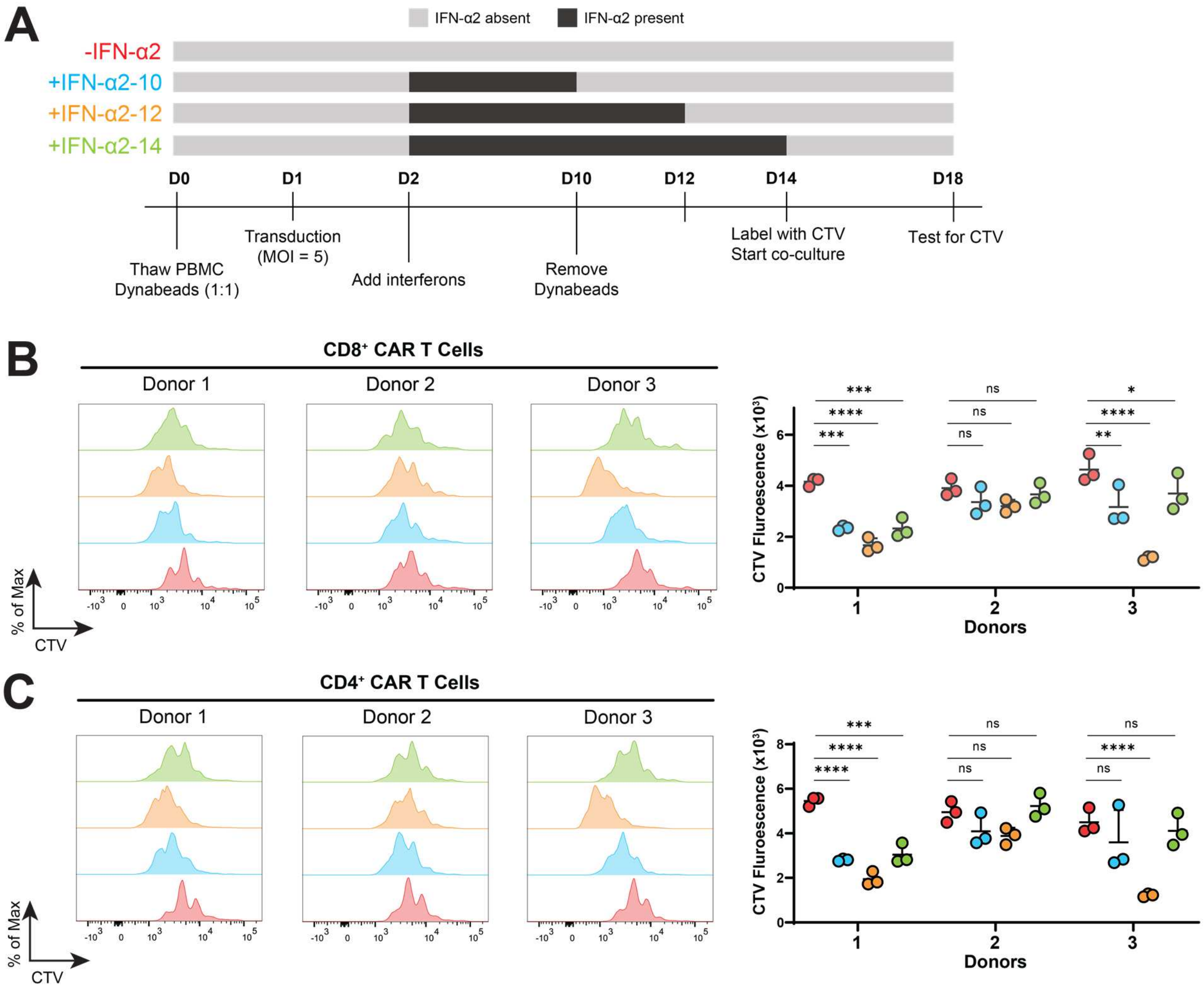

Figure V-3. IFN-I signaling increases CAR T-cell proliferation *in vitro*. (A) Schematic depicting transduction and culturing of CAR T cells in the -IFN-α2 and various +IFN-α2 conditions. IFN-α2 was removed from the culture medium at either day 10, day 12, or day 14. (B-C) CellTrace Violet fluorescence of OCI-Ly8-stimulated CD8$^+$ (B) or CD4$^+$ (C) CAR T cells from a representative donor (left, histogram) or from three independent donors (right, dot plot). Fluorescence values were compared by mixed 2-way ANOVA and post-hoc *t*-tests, whereby **** denotes $p<0.0001$, *** denotes $p<0.001$, ** denotes $p<0.01$, * denotes $p<0.05$, and ns denotes not significant.

III: Discussion

In this study, we investigated how IFN-I signaling influences CAR T-cell differentiation, effector functions, and proliferation *in vitro*. Using IFN-α2 as our exemplary IFN-I family member, we demonstrated that IFN-I signaling enriches for the $CD8^+$ stem cell memory ($CD45RA^+CCR7^+$) and $CD4^+$ ($CD45RA^+CCR7^-$) central memory phenotypes. Upon engagement with antigen-expressing lymphoma target cells, interferon-treated CAR T cells exhibited increased cytotoxicity, polyfunctional cytokine secretion, and proliferation compared to non-treated controls. All results were replicable across three independent healthy donors. Our promising *in vitro* findings suggest that IFN-I signaling may also increase CAR T-cell *in vivo* efficacy, leading to an effective and easily implemented solution to decrease CAR T-cell therapy non-response rates.

Our findings are compatible with existing literature on the direct effects of IFN-I signaling on T cells. Enhancement of cytotoxicity and induction of memory differentiation among $CD8^+$ T cells has been reported.[204,210] Direct type I interferon signaling in T cells is known to have different consequences, depending on whether TCR stimulation precedes (in-sequence signaling) or follows (out-of-sequence signaling) IFN-I signaling. In-sequence signaling generally enhances T-cell survival, effector functions, and proliferation, while out-of-sequence signaling generally does the opposite.[200] In our studies, since T-cell activation (via CD3/CD28 Dynabeads) preceded IFN-I treatment, the T cells were subject to in-sequence signaling. Our findings are aligned with this model, since they mirror the expected consequences of in-sequence IFN-I signaling. Finally, an existing CAR study demonstrated that IRF7 supported the persistence, effector functions, and expansion of anti-CD19 CAR T cells[181], which is well-aligned with our *in vitro* findings.

Although these findings highlight IFN-I as a promising enhancer during the CAR T-cell production process, there are important limitations to consider. Firstly, our results are based on *in vitro* experiments. Future work should test the *in vivo* efficacy of interferon-treated CAR T cells in mouse lymphoma models, including xenograft and syngeneic models. Secondly, our results are based on CAR T cells generated from healthy donors. However, CAR T cells generated from patients may exhibited different responses to IFN-I signaling, due to baseline imprinted epigenetic differences prior to CAR transduction. Thirdly, our results are limited to $CD19^+$ B-cell lymphomas, but different mechanisms are at work when T cells kill epithelial cells in non-hematological solid tumors.[211] Future studies should test whether interferon-treated CAR T cells also exhibit greater functionality against epithelial target cells. Finally, our findings are based on a limited study set of 3 healthy donors. Future studies should expand this limited study set in order to capture whether the effects of IFN-I signaling on CAR T cells are more generalizable across different human donors.

IV: Methods

Lentiviral production and transduction.

A green fluorescence protein-tagged, CD28-costimulated, anti-CD19 human CAR was cloned onto the pHR vector backbone to constitute the transfer plasmid.[93] Transfer plasmids were transfected into the Lenti-X 293T packaging cell line (Takara, 632180) for lentiviral production. Lenti-X 293T cells were routinely cultured in DMEM and 10% fetal bovine serum (X&Y Cell Culture, FBS-500). In brief, Lenti-X 293T cells were seeded and grown overnight. During the following day, transfer plasmids (0.95 µg, pJH052), packaging plasmids (0.72 µg, psPAX2), and envelope plasmids (0.22 µg, pMD2.G) were co-transfected into Lenti-X 293T cells via Lipofectamine 3000 (Invitrogen, L3000001). After 72 hours, the viral supernatant was stored at -80°C until transduction.

Concentrated lentiviruses were used to transduce E6-1 Jurkat T cells or primary human T cells. During transduction, lentiviruses were added to cells along with protamine sulfate (Millipore Sigma, P3369-10G) to a final concentration of 10 µg/mL. Cells were spinoculated at 800 x *g* for 60 minutes at room temperature. Then, cells were grown for 72 hours before analysis of transduction efficiency by flow cytometry. Untransduced cells were used for gating.

CAR T-cell production and culturing.

Cryopreserved human peripheral blood mononuclear cells (PBMCs) from healthy donors were thawed in warm T-cell media (RPMI supplemented with 10% FBS, 1% penicillin/streptomycin, 2 mM L-glutamine, and 50 µM 2-mercaptoethanol). Subsequently, PBMCs were cultured for 3 hours in complete T-cell media (T-cell media supplemented with 50 units/mL of IL-2) in order to allow monocytes to adhere to the culture flask. Finally, the non-adhered cells were transferred to a new culture flask. Cell counts and T-cell representation (% CD3$^+$ of total cells) were calculated by flow cytometry.

T cells were seeded in complete T-cell media at 0.75 M/mL. CD3/CD28 Dynabeads (Gibco, 11161D) were washed and added at 1:1 ratio. After overnight activation, T cells were transduced with CAR lentiviruses (multiplicity of infection of 5). After T cells were mixed with lentiviruses for 24 hours, the media was changed, cells were washed, and media was replaced with complete T-cell media with and without 3000 units/mL of recombinant IFN-α2 (BioLegend, 592702). T cells were subsequently expanded, and media was completely replaced every 2-3 days.

Multiparameter flow cytometry.

T cells were washed with cold FACS buffer (PBS, 2% BSA, 0.05% sodium azide). Fc receptors were blocked by incubation with Human TruStain FcX (BioLegend, 422301) at 1:50 dilution for 5 minutes at 4°C. Then, cells were incubated for 30 minutes at 4°C in the dark with a staining solution containing antibodies. Antibodies were generally used according to manufacturer recommendations. After staining, cells were incubated briefly with LIVE/DEAD Fixable Near-IR viability dye (Invitrogen, L34975) diluted 1:1000 in PBS for 5 minutes at room temperature. Then, cells were three times in FACS buffer at 4°C. If no intracellular markers are profiled, then stained cells are directed analyzed by flow cytometry.

For intracellular staining, stained cells are subject to the BD Fixation/Permeabilization Kit (BD Biosciences, 554714) for cytoplasmic antigens or True-Nuclear Transcription Factor Buffer Set (BioLegend, 424401) for nuclear antigens. Kits were used according to manufacturer recommendations. In general, cells were fixed in the fixation buffer, washed thrice in the permeabilization buffer, and incubated for 60 minutes at 4°C in the dark with a staining solution containing antibodies and permeabilization buffer. After staining, cells were washed three times in permeabilization buffer and once in FACS buffer. Cells were then analyzed by flow cytometry.

Flow phenotyping panels.

Unless otherwise stated, all antibodies originate from BioLegend and were used according to manufacturer recommendations.

For profiling CAR T-cell memory phenotype, the surface staining solution contained: BV510-anti-CD4 (clone SK3, 344633), PerCP/Cy5.5-anti-CD8α (clone SK1, 344709), PE-anti-CD45RA (clone HI100, 304107), BV421-anti-CD45RO (clone UCHL1, 304223), AF647-anti-CCR7 (clone G043H7, 353217), AF700-anti-CD62L (clone DREG-56, 304820), BV650-anti-CD127 (clone A019D5, 351325), BV711-anti-CD27 (clone O323, 302833), PE/Dazzle594-anti-CD28 (clone CD28.2, 302941), BV605-anti-CD57 (clone QA17A04, 393303), and PE/Cy7-anti-KLRG1 (clone 14C2A07, 368613). No intracellular antigens were tested.

For profiling mitochondrial potential and content via MitoSpy Orange, the surface staining solution contained: BV510-anti-CD4 (clone SK3, 344633) and PerCP/Cy5.5-anti-CD8α (clone SK1, 344709). No intracellular antigens were tested.

For profiling cytokine secretion, the surface staining solution contained: BV510-anti-CD4 (clone SK3, 344633) and PerCP/Cy5.5-anti-CD8α (clone SK1, 344709). The intracellular staining solution contained BV605-anti-IFN-γ (clone 4S.B3, 502535), BV650-anti-TNF-α (clone Mab11, 502937), AF647-anti-IL-2 (clone MQ1-17H12, 500315), PE-anti-IL-10 (clone JES3-9D7, 501403), and BV421-anti-IL-4 (clone MP4-25D2, 500825).

Cytotoxicity testing.

CAR T cells and luciferized target cells were seeded at chosen effector-to-target ratios in 100 µL of T-cell medium in black 96-well plate (Corning, CLS3603). After a 6-hour co-culture, 100 µL of Bright-Glo Luciferase substrate (Promega, E2610) was added, and each well were tested for luciferase activity. As a positive control for cytotoxicity, target cells were directly lysed with NP-40 (Abcam, ab142227) at 1% final concentration.

V: Acknowledgements

We thank Phi Beta Psi, the Ullman Fund in Cancer Immunology, the Hoogland Lymphoma Research Pilot Projects, Chicago Immunoengineering Innovation Center, and NIH New Innovator award (1DP2AI144245) for financial support (to J.H.). Y.H. was supported by the University of Chicago MSTP Training Grant (T32GM007281). We thank the UChicago Blood Donation Center for healthy donor PBMCs.

VI: Contributions

Yifei Hu[1,2,#], Guoshuai Cao[1,#], Erting Tang[1,#], Nick Asby[1], Lishi Xie[3], Xiufen Chen[3], Thomas Althaus[6], Peter A. Riedell[4,5,6], Michael R. Bishop[5,6], Justin P. Kline[3,4,5,6], Jun Huang[1,3,4,*]

[1]Pritzker School of Molecular Engineering, University of Chicago, Chicago, IL 60637, USA

[2]Pritzker School of Medicine, University of Chicago, Chicago, IL 60637, USA

[3]Committee on Immunology, University of Chicago, Chicago, IL 60637, USA

[4]Committee on Cancer Biology, University of Chicago, Chicago, IL 60637, USA

[5]Department of Medicine, University of Chicago, Chicago, IL 60637, USA

[6]The David and Etta Jonas Center for Cellular Therapy, University of Chicago, Chicago, IL 60637, USA

[#]These authors contributed equally.

Y.H., G.C., and J.H. conceived the ideas. E.T., Y.H., G.C., J.P.K., and J.H. designed all experiments. J.H. supervised the project. T.A., P.A.R., and M.R.B. coordinated patient biospecimens for these studies. E.T. and Y.H. performed *in vitro* experimentation. Y.H. generated single-cell patient data. G.C. performed single-cell omics and machine-learning analyses. N.A. designed and cloned the knockdown constructs. E.T., L.X., X.C., and Y.H. performed *in vivo* experimentation.

REFERENCES

1. Diffuse Large B-Cell Lymphoma - Cancer Stat Facts. https://seer.cancer.gov/statfacts/html/dlbcl.html.
2. Liu, Y. & Barta, S. K. Diffuse large B-cell lymphoma: 2019 update on diagnosis, risk stratification, and treatment. *Am J Hematol* **94**, 604–616 (2019).
3. Longo, D. L., Sehn, L. H. & Salles, G. Diffuse Large B-Cell Lymphoma. *https://doi-org.proxy.uchicago.edu/10.1056/NEJMra2027612* **384**, 842–858 (2021).
4. Neelapu, S. S. *et al.* Axicabtagene Ciloleucel CAR T-Cell Therapy in Refractory Large B-Cell Lymphoma. *New England Journal of Medicine* **377**, 2531–2544 (2017).
5. Schuster, S. J. *et al.* Tisagenlecleucel in adult relapsed or refractory diffuse large B-cell lymphoma. *New England Journal of Medicine* **380**, 45–56 (2019).
6. Abramson, J. S. *et al.* Pivotal Safety and Efficacy Results from Transcend NHL 001, a Multicenter Phase 1 Study of Lisocabtagene Maraleucel (liso-cel) in Relapsed/Refractory (R/R) Large B Cell Lymphomas. *Blood* **134**, 241–241 (2019).
7. Abramson, J. S. *et al.* Lisocabtagene maraleucel for patients with relapsed or refractory large B-cell lymphomas (TRANSCEND NHL 001): a multicentre seamless design study. *The Lancet* **396**, 839–852 (2020).
8. Gross, G., Waks, T. & Eshhar, Z. Expression of immunoglobulin-T-cell receptor chimeric molecules as functional receptors with antibody-type specificity. *Proc Natl Acad Sci U S A* **86**, 10024–10028 (1989).
9. Eshhar, Z., Waks, T., Gross, G. & Schindler, D. G. Specific activation and targeting of cytotoxic lymphocytes through chimeric single chains consisting of antibody-binding domains and the γ or ζ subunits of the immunoglobulin and T-cell receptors. *Proc Natl Acad Sci U S A* **90**, 720–724 (1993).
10. Lenschow, D. J., Walunas, T. L. & Bluestone, J. A. CD28/B7 SYSTEM OF T CELL COSTIMULATION. *http://dx.doi.org/10.1146/annurev.immunol.14.1.233* **14**, 233–258 (2003).
11. Jenkins, M. K., Taylor, P. S., Norton, S. D. & Urdahl, K. B. CD28 delivers a costimulatory signal involved in antigen-specific IL-2 production by human T cells. *The Journal of Immunology* **147**, (1991).
12. Krause, A. *et al.* Antigen-dependent CD28 Signaling Selectively Enhances Survival and Proliferation in Genetically Modified Activated Human Primary T Lymphocytes. *Journal of Experimental Medicine* **188**, 619–626 (1998).
13. Maher, J., Brentjens, R. J., Gunset, G., Rivière, I. & Sadelain, M. Human T-lymphocyte cytotoxicity and proliferation directed by a single chimeric TCRζ /CD28 receptor. *Nature Biotechnology 2002 20:1* **20**, 70–75 (2002).
14. Brentjens, R. J. *et al.* Genetically targeted T cells eradicate systemic acute lymphoblastic leukemia xenografts. *Clinical Cancer Research* **13**, 5426–5435 (2007).
15. Finney, H. M., Akbar, A. N. & Lawson, A. D. G. Activation of Resting Human Primary T Cells with Chimeric Receptors: Costimulation from CD28, Inducible Costimulator, CD134, and CD137 in Series with Signals from the TCRζ Chain. *The Journal of Immunology* **172**, 104–113 (2004).
16. Imai, C. *et al.* Chimeric receptors with 4-1BB signaling capacity provoke potent cytotoxicity against acute lymphoblastic leukemia. *Leukemia* **18**, 676–684 (2004).
17. Milone, M. C. *et al.* Chimeric receptors containing CD137 signal transduction domains mediate enhanced survival of T cells and increased antileukemic efficacy in vivo. *Molecular Therapy* **17**, 1453–1464 (2009).

18. Cappell, K. M. & Kochenderfer, J. N. A comparison of chimeric antigen receptors containing CD28 versus 4-1BB costimulatory domains. *Nature Reviews Clinical Oncology 2021 18:11* **18**, 715–727 (2021).
19. Kochenderfer, J. N. *et al.* Eradication of B-lineage cells and regression of lymphoma in a patient treated with autologous T cells genetically engineered to recognize CD19. *Blood* **116**, 4099–4102 (2010).
20. Kalos, M. *et al.* T cells with chimeric antigen receptors have potent antitumor effects and can establish memory in patients with advanced leukemia. *Sci Transl Med* **3**, 1–12 (2011).
21. Meng, J. *et al.* Efficacy and Safety of CAR-T Cell Products Axicabtagene Ciloleucel, Tisagenlecleucel, and Lisocabtagene Maraleucel for the Treatment of Hematologic Malignancies: A Systematic Review and Meta-Analysis. *Front Oncol* **11**, 2699 (2021).
22. Deng, Q. *et al.* Characteristics of anti-CD19 CAR T cell infusion products associated with efficacy and toxicity in patients with large B cell lymphomas. *Nat Med* **26**, 1878–1887 (2020).
23. Rossi, J. *et al.* Preinfusion polyfunctional anti-CD19 chimeric antigen receptor T cells are associated with clinical outcomes in NHL. *Blood* **132**, 804–814 (2018).
24. Blank, C. U. *et al.* Defining 'T cell exhaustion'. *Nat Rev Immunol* **19**, 665–674 (2019).
25. Wherry, E. J. T cell exhaustion. *Nat Immunol* **12**, 492–499 (2011).
26. Chen, J. *et al.* Nr4a transcription factors limit CAR T-cell function in solid tumors. *Nature* **567**, 530–534 (2019).
27. Long, A. H. *et al.* 4-1BB costimulation ameliorates T cell exhaustion induced by tonic signaling of chimeric antigen receptors. *Nat Med* **21**, 581–590 (2015).
28. Yang, Y. *et al.* TCR engagement negatively affects CD8 but not CD4 CAR T cell expansion and leukemic clearance. *Sci Transl Med* **9**, (2017).
29. Sterner, R. C. & Sterner, R. M. CAR-T cell therapy: current limitations and potential strategies. *Blood Cancer Journal* vol. 11 1–11 Preprint at https://doi.org/10.1038/s41408-021-00459-7 (2021).
30. Milone, M. C. *et al.* Engineering-enhanced CAR T cells for improved cancer therapy. *Nature Cancer 2021 2:8* **2**, 780–793 (2021).
31. Locke, F. L. *et al.* Axicabtagene Ciloleucel as Second-Line Therapy for Large B-Cell Lymphoma. *New England Journal of Medicine* **386**, 640–654 (2022).
32. Bishop, M. R. *et al.* Second-Line Tisagenlecleucel or Standard Care in Aggressive B-Cell Lymphoma. *New England Journal of Medicine* **386**, 629–639 (2022).
33. Kamdar, M. *et al.* Lisocabtagene Maraleucel (liso-cel), a CD19-Directed Chimeric Antigen Receptor (CAR) T Cell Therapy, Versus Standard of Care (SOC) with Salvage Chemotherapy (CT) Followed By Autologous Stem Cell Transplantation (ASCT) As Second-Line (2L) Treatment in Patients (Pts) with Relapsed or Refractory (R/R) Large B-Cell Lymphoma (LBCL): Results from the Randomized Phase 3 Transform Study. *Blood* **138**, 91–91 (2021).
34. Westin, J. & Sehn, L. H. CAR T cells as a second-line therapy for large B-cell lymphoma: a paradigm shift? *Blood* **139**, 2737–2746 (2022).
35. Neelapu, S. S. *et al.* Axicabtagene ciloleucel as first-line therapy in high-risk large B-cell lymphoma: the phase 2 ZUMA-12 trial. *Nat Med* **28**, 735–742 (2022).
36. Liu, J., Zhou, G., Zhang, L. & Zhao, Q. Building potent chimeric antigen receptor T cells with CRISPR genome editing. *Frontiers in Immunology* vol. 10 456 Preprint at https://doi.org/10.3389/fimmu.2019.00456 (2019).
37. Hamada, M. *et al.* Integration Mapping of piggyBac-Mediated CD19 Chimeric Antigen Receptor T Cells Analyzed by Novel Tagmentation-Assisted PCR. *EBioMedicine* **34**, 18–26 (2018).

38. Maude, S. L. *et al.* Tisagenlecleucel in Children and Young Adults with B-Cell Lymphoblastic Leukemia. *New England Journal of Medicine* **378**, 439–448 (2018).
39. Fraietta, J. A. *et al.* Determinants of response and resistance to CD19 chimeric antigen receptor (CAR) T cell therapy of chronic lymphocytic leukemia. *Nat Med* **24**, 563–571 (2018).
40. Wang, H. *et al.* Establishment of a Quantitative Polymerase Chain Reaction Assay for Monitoring Chimeric Antigen Receptor T Cells in Peripheral Blood. *Transplant Proc* **50**, 104–109 (2018).
41. Kunz, A. *et al.* Optimized Assessment of qPCR-Based Vector Copy Numbers as a Safety Parameter for GMP-Grade CAR T Cells and Monitoring of Frequency in Patients. *Mol Ther Methods Clin Dev* **17**, 448–454 (2020).
42. Ståhlberg, A. & Kubista, M. Technical aspects and recommendations for single-cell qPCR. *Molecular Aspects of Medicine* vol. 59 28–35 Preprint at https://doi.org/10.1016/j.mam.2017.07.004 (2018).
43. Vogelstein, B. & Kinzler, K. W. Digital PCR. *Proc Natl Acad Sci U S A* **96**, 9236–9241 (1999).
44. Fehse, B. *et al.* Digital PCR Assays for Precise Quantification of CD19-CAR-T Cells after Treatment with Axicabtagene Ciloleucel. *Mol Ther Methods Clin Dev* **16**, 172–178 (2020).
45. Santeramo, I. *et al.* Vector copy distribution at a single cell level enhances analytical characterisation of gene-modified cell therapies. *Mol Ther Methods Clin Dev* **17**, 944–956 (2020).
46. Nobles, C. L. *et al.* CD19-targeting CAR T cell immunotherapy outcomes correlate with genomic modification by vector integration. *Journal of Clinical Investigation* **130**, 673–685 (2020).
47. Fraietta, J. A. *et al.* Disruption of TET2 promotes the therapeutic efficacy of CD19-targeted T cells. *Nature* 1 (2018) doi:10.1038/s41586-018-0178-z.
48. Hacien-Bey-Abina, S. *et al.* LMO2-Associated Clonal T Cell Proliferation in Two Patients after Gene Therapy for SCID-X1. *Science (1979)* **302**, 415–419 (2003).
49. Wu, X., Li, Y., Crise, B. & Burgess, S. M. Transcription start regions in the human genome are favored targets for MLV integration. *Science (1979)* **300**, 1749–1751 (2003).
50. Brady, T. *et al.* A method to sequence and quantify DNA integration for monitoring outcome in gene therapy. *Nucleic Acids Res* **39**, 1–8 (2011).
51. Berry, C. C. *et al.* INSPIIRED: Quantification and Visualization Tools for Analyzing Integration Site Distributions. *Mol Ther Methods Clin Dev* **4**, 17–26 (2017).
52. Sherman, E. *et al.* INSPIIRED: A Pipeline for Quantitative Analysis of Sites of New DNA Integration in Cellular Genomes. *Mol Ther Methods Clin Dev* **4**, 39–49 (2017).
53. Wang, W. *et al.* Joint profiling of chromatin accessibility and CAR-T integration site analysis at population and single-cell levels. *Proc Natl Acad Sci U S A* **117**, 5442–5452 (2020).
54. Berry, C. C. *et al.* Estimating abundances of retroviral insertion sites from DNA fragment length data. *Bioinformatics* **28**, 755–762 (2012).
55. Gomes-Silva, D. *et al.* Tonic 4-1BB Costimulation in Chimeric Antigen Receptors Impedes T Cell Survival and Is Vector-Dependent. *Cell Rep* **21**, 17–26 (2017).
56. Walker, A. J. *et al.* Tumor Antigen and Receptor Densities Regulate Efficacy of a Chimeric Antigen Receptor Targeting Anaplastic Lymphoma Kinase. *Molecular Therapy* **25**, 2189–2201 (2017).
57. Zhang, Q. *et al.* Transcriptome and Regulatory Network Analyses of CD19-CAR-T Immunotherapy for B-ALL. *Genomics Proteomics Bioinformatics* **17**, 190–200 (2019).
58. Sheih, A. *et al.* Clonal kinetics and single-cell transcriptional profiling of CAR-T cells in patients undergoing CD19 CAR-T immunotherapy. *Nat Commun* **11**, 1–13 (2020).

59. Wang, N., Rajasekaran, N., Hou, T., Lisowski, L. & Mellins, E. D. Comparison of transduction efficiency among various lentiviruses containing GFP reporter in bone marrow hematopoietic stem cell transplantation. *Exp Hematol* **41**, 934–943 (2013).
60. Wang, F. *et al.* RNAscope: A novel in situ RNA analysis platform for formalin-fixed, paraffin-embedded tissues. *Journal of Molecular Diagnostics* **14**, 22–29 (2012).
61. O'Rourke, D. M. *et al.* A single dose of peripherally infused EGFRvIII-directed CAR T cells mediates antigen loss and induces adaptive resistance in patients with recurrent glioblastoma. *Sci Transl Med* **9**, eaaa0984 (2017).
62. Pimentel, H. *et al.* Abstract 2324: Preclinical safety, biodistribution, and tumor infiltration analysis of CAR T cell targets using in situ hybridization technology. in *Immunology* vol. 79 2324–2324 (American Association for Cancer Research, 2019).
63. Yang, Y. *et al.* TCR engagement negatively affects CD8 but not CD4 CAR T cell expansion and leukemic clearance. *Sci Transl Med* **9**, 1–13 (2017).
64. Hamieh, M. *et al.* CAR T cell trogocytosis and cooperative killing regulate tumour antigen escape. *Nature* **568**, 112–116 (2019).
65. Kochenderfer, J. N. *et al.* Construction and preclinical evaluation of an anti-CD19 chimeric antigen receptor. *Journal of Immunotherapy* **32**, 689–702 (2009).
66. Nilson, B. H. K., Lögdberg, L., Kastern, W., Björck, L. & Åkerström, B. Purification of antibodies using protein L-binding framework structures in the light chain variable domain. *J Immunol Methods* **164**, 33–40 (1993).
67. Zheng, Z., Chinnasamy, N. & Morgan, R. A. Protein L: A novel reagent for the detection of Chimeric Antigen Receptor (CAR) expression by flow cytometry. *J Transl Med* **10**, (2012).
68. Han, X. *et al.* Masked Chimeric Antigen Receptor for Tumor-Specific Activation. *Molecular Therapy* **25**, 274–284 (2017).
69. Sun, M. *et al.* Construction and evaluation of a novel humanized HER2-specific chimeric receptor. *Breast Cancer Research* **16**, 1–10 (2014).
70. Ruella, M. *et al.* Dual CD19 and CD123 targeting prevents antigen-loss relapses after CD19-directed immunotherapies. *Journal of Clinical Investigation* **126**, 3814–3826 (2016).
71. de Oliveira, S. N. *et al.* A CD19/Fc fusion protein for detection of anti-CD19 chimeric antigen receptors. *J Transl Med* **11**, (2013).
72. Chang, Z. L. *et al.* Rewiring T-cell responses to soluble factors with chimeric antigen receptors. *Nat Chem Biol* **14**, 317–324 (2018).
73. Teplyakov, A., Obmolova, G., Luo, J. & Gilliland, G. L. Crystal structure of B-cell co-receptor CD19 in complex with antibody B43 reveals an unexpected fold. *Proteins: Structure, Function and Bioinformatics* **86**, 495–500 (2018).
74. Lobner, E. *et al.* Getting CD19 Into Shape: Expression of Natively Folded "Difficult-to-Express" CD19 for Staining and Stimulation of CAR-T Cells. *Front Bioeng Biotechnol* **8**, 1–13 (2020).
75. Toebes, M., Rodenko, B., Ovaa, H. & Schumacher, T. N. M. Generation of peptide MHC class I monomers and multimers through ligand exchange. *Curr Protoc Immunol* 1–20 (2009) doi:10.1002/0471142735.im1816s87.
76. Bentzen, A. K. & Hadrup, S. R. Evolution of MHC-based technologies used for detection of antigen-responsive T cells. *Cancer Immunology, Immunotherapy* **66**, 657–666 (2017).
77. Huang, J. *et al.* Detection, phenotyping, and quantification of antigen-specific T cells using a peptide-MHC dodecamer. *Proceedings of the National Academy of Sciences* **113**, E1890–E1897 (2016).
78. Batard, P. *et al.* Dextramers: New generation of fluorescent MHC class I/peptide multimers for visualization of antigen-specific CD8+ T cells. *J Immunol Methods* **310**, 136–148 (2006).

79. Jena, B. *et al.* Chimeric Antigen Receptor (CAR)-Specific Monoclonal Antibody to Detect CD19-Specific T Cells in Clinical Trials. *PLoS One* **8**, e57838 (2013).
80. Lee, D. W. *et al.* T cells expressing CD19 chimeric antigen receptors for acute lymphoblastic leukaemia in children and young adults: A phase 1 dose-escalation trial. *The Lancet* **385**, 517–528 (2015).
81. Ruella, M. *et al.* A Cellular Antidote to Specifically Deplete Anti-CD19 Chimeric Antigen Receptor (CAR19) Positive Cells. *Blood* **130**, 4463–4463 (2017).
82. Yvon, E. *et al.* Immunotherapy of metastatic melanoma using genetically engineered GD2-specific T cells. *Clinical Cancer Research* **15**, 5852–5860 (2009).
83. Sievers, S. A., Kelley, K. A., Astrow, S. H., Bot, A. & Wiltzius, J. J. Abstract 1204: Design and development of anti-linker antibodies for the detection and characterization of CAR T cells. in *Experimental and Molecular Therapeutics* 1204–1204 (American Association for Cancer Research, 2019). doi:10.1158/1538-7445.SABCS18-1204.
84. Chen, P.-H. *et al.* Analysis of CAR-T and Immune Cells within the Tumor Micro-Environment of Diffuse Large B-Cell Lymphoma Post CAR-T Treatment By Multiplex Immunofluorescence. *Blood* **132**, 678–678 (2018).
85. Gopalakrishnan, R. *et al.* A novel luciferase-based assay for the detection of Chimeric Antigen Receptors. *Sci Rep* **9**, 1–13 (2019).
86. Ramello, M. C. *et al.* An immunoproteomic approach to characterize the CAR interactome and signalosome. *Sci Signal* **12**, 1–16 (2019).
87. Salter, A. I. *et al.* Phosphoproteomic analysis of chimeric antigen receptor signaling reveals kinetic and quantitative differences that affect cell function. *Sci Signal* **11**, 1–18 (2018).
88. Davenport, A. J. *et al.* Chimeric antigen receptor T cells form nonclassical and potent immune synapses driving rapid cytotoxicity. *Proc Natl Acad Sci U S A* **115**, E2068–E2076 (2018).
89. Jang, J. H. *et al.* Imaging of Cell–Cell Communication in a Vertical Orientation Reveals High-Resolution Structure of Immunological Synapse and Novel PD-1 Dynamics. *The Journal of Immunology* **195**, 1320–1330 (2015).
90. Xiong, W. *et al.* Immunological Synapse Predicts Effectiveness of Chimeric Antigen Receptor Cells. *Molecular Therapy* **26**, 963–975 (2018).
91. Libby, K. A. & Su, X. Imaging Chimeric Antigen Receptor (CAR) Activation. in *Methods in Molecular Biology* vol. 2111 153–160 (Humana, New York, NY, 2020).
92. Su, X. & Vale, R. Mechanisms of Chimeric Antigen Receptor (CAR) Signaling during T Cell Activation. *Biophys J* **114**, 107a–108a (2018).
93. Morrissey, M. A. *et al.* Chimeric antigen receptors that trigger phagocytosis. *Elife* **7**, (2018).
94. Sasmal, D. K. *et al.* TCR–pMHC bond conformation controls TCR ligand discrimination. *Cell Mol Immunol* **17**, 203–217 (2020).
95. Rosenberg, J. & Huang, J. Visualizing surface T-cell receptor dynamics four-dimensionally using lattice light-sheet microscopy. *Journal of Visualized Experiments* **2020**, e59914 (2019).
96. Rosenberg, J., Cao, G., Borja-Prieto, F. & Huang, J. Lattice Light-Sheet Microscopy Multi-dimensional Analyses (LaMDA) of T-Cell Receptor Dynamics Predict T-Cell Signaling States. *Cell Syst* **10**, 433-444.e5 (2020).
97. Nerreter, T. *et al.* Super-resolution microscopy reveals ultra-low CD19 expression on myeloma cells that triggers elimination by CD19 CAR-T. *Nat Commun* **10**, 3137 (2019).
98. Mezzanotte, L., van ‘t Root, M., Karatas, H., Goun, E. A. & Löwik, C. W. G. M. In Vivo Molecular Bioluminescence Imaging: New Tools and Applications. *Trends Biotechnol* **35**, 640–652 (2017).

99. Torres Chavez, A. *et al.* Expanding CAR T cells in human platelet lysate renders T cells with in vivo longevity. *J Immunother Cancer* **7**, 1–15 (2019).
100. Dawson, N. A. J. *et al.* Systematic testing and specificity mapping of alloantigen-specific chimeric antigen receptors in regulatory T cells. *JCI Insight* **4**, (2019).
101. Serganova, I. *et al.* Enhancement of PSMA-Directed CAR Adoptive Immunotherapy by PD-1/PD-L1 Blockade. *Mol Ther Oncolytics* **4**, 41–54 (2017).
102. Stowe, C. L. *et al.* Near-infrared dual bioluminescence imaging in mouse models of cancer using infraluciferin. *Elife* **8**, 1–22 (2019).
103. Kuchimaru, T. *et al.* A luciferin analogue generating near-infrared bioluminescence achieves highly sensitive deep-tissue imaging. *Nat Commun* **7**, 1–5 (2016).
104. Alavi, A. & Huang, S. S. Positron emission tomography in medicine: An overview. *Cancer Imaging* **31**, 39–44 (2008).
105. Keu, K. V. *et al.* Reporter gene imaging of targeted T cell immunotherapy in recurrent glioma. *Sci Transl Med* **9**, (2017).
106. Eissenberg, L. G., Rettig, M., Dehdashti, F., Piwnica-Worms, D. & DiPersio, J. F. Suicide genes: Monitoring cells in patients with a safety switch. *Front Pharmacol* **5**, 5–8 (2014).
107. Krebs, S. *et al.* Antibody with infinite affinity for in vivo tracking of genetically engineered lymphocytes. *Journal of Nuclear Medicine* **59**, 1894–1900 (2018).
108. Sellmyer, M. A. *et al.* Imaging CAR T Cell Trafficking with eDFHR as a PET Reporter Gene. *Molecular Therapy* **28**, 42–51 (2019).
109. Park, S. *et al.* Micromolar affinity CAR T cells to ICAM-1 achieves rapid tumor elimination while avoiding systemic toxicity. *Sci Rep* **7**, 1–15 (2017).
110. Bhanat, E., Koch, C. A., Parmar, R., Garla, V. & Vijayakumar, V. Somatostatin receptor expression in non-classical locations – clinical relevance? *Rev Endocr Metab Disord* 123–132 (2018) doi:10.1007/s11154-018-9470-3.
111. Emami-Shahri, N. *et al.* Clinically compliant spatial and temporal imaging of chimeric antigen receptor T-cells. *Nat Commun* **9**, 1–12 (2018).
112. Minn, I. *et al.* Imaging CAR T cell therapy with PSMA-targeted positron emission tomography. *Sci Adv* **5**, (2019).
113. Lee, S. H. *et al.* Feasibility of real-time in vivo 89Zr-DFO-labeled CAR T-cell trafficking using PET imaging. *PLoS One* **15**, 1–21 (2020).
114. Ishii, T. & Ishii, M. Intravital two-photon imaging: A versatile tool for dissecting the immune system. *Ann Rheum Dis* **70**, 113–115 (2011).
115. Cazaux, M. *et al.* Single-cell imaging of CAR T cell activity in vivo reveals extensive functional and anatomical heterogeneity. *Journal of Experimental Medicine* **216**, 1038–1049 (2019).
116. Mulazzani, M. *et al.* Long-term in vivo microscopy of CAR T cell dynamics during eradication of CNS lymphoma in mice. *Proc Natl Acad Sci U S A* **116**, 24275–24284 (2019).
117. Ma, B. *et al.* Two-photon fluorescent polydopamine nanodots for CAR-T cell function verification and tumor cell/tissue detection. *J Mater Chem B* **6**, 6459–6467 (2018).
118. Harris, D. T. *et al.* Comparison of T Cell Activities Mediated by Human TCRs and CARs That Use the Same Recognition Domains. *The Journal of Immunology* **200**, 1088–1100 (2018).
119. Hu, Y. & Huang, J. The Chimeric Antigen Receptor Detection Toolkit. *Front Immunol* **11**, 1–16 (2020).
120. Laurent, E. *et al.* Directed Evolution of Stabilized Monomeric CD19 for Monovalent CAR Interaction Studies and Monitoring of CAR-T Cell Patients. *ACS Synth Biol* **10**, 712–717 (2021).

121. Wooldridge, L. *et al.* Tricks with tetramers: how to get the most from multimeric peptide-MHC. *Immunology* vol. 126 147–164 Preprint at https://doi.org/10.1111/j.1365-2567.2008.02848.x (2009).
122. Davis, M. M., Altman, J. D. & Newell, E. W. Interrogating the repertoire: Broadening the scope of peptide-MHC multimer analysis. *Nat Rev Immunol* **11**, 551–558 (2011).
123. Altman, J. D. *et al.* Phenotypic analysis of antigen-specific T lymphocytes. *Science* **274**, 94–6 (1996).
124. Fairhead, M. & Howarth, M. Site-specific biotinylation of purified proteins using BirA. *Methods Mol Biol* **1266**, 171–84 (2015).
125. Ghorashian, S. *et al.* Enhanced CAR T cell expansion and prolonged persistence in pediatric patients with ALL treated with a low-affinity CD19 CAR. *Nat Med* **25**, 1408–1414 (2019).
126. Sharma, P. *et al.* Structure-guided engineering of the affinity and specificity of CARs against Tn-glycopeptides. *Proc Natl Acad Sci U S A* **117**, 15148–15159 (2020).
127. Chmielewski, M., Hombach, A., Heuser, C., Adams, G. P. & Abken, H. T Cell Activation by Antibody-Like Immunoreceptors: Increase in Affinity of the Single-Chain Fragment Domain above Threshold Does Not Increase T Cell Activation against Antigen-Positive Target Cells but Decreases Selectivity. *The Journal of Immunology* **173**, 7647–7653 (2004).
128. Brudno, J. N. *et al.* Safety and feasibility of anti-CD19 CAR T cells with fully human binding domains in patients with B-cell lymphoma. *Nat Med* **26**, 270–280 (2020).
129. Li, W. *et al.* Chimeric Antigen Receptor Designed to Prevent Ubiquitination and Downregulation Showed Durable Antitumor Efficacy. *Immunity* **53**, 456–470 (2020).
130. Maude, S. L. *et al.* Chimeric Antigen Receptor T Cells for Sustained Remissions in Leukemia. *New England Journal of Medicine* **371**, 1507–1517 (2014).
131. Day, C. L. *et al.* Ex vivo analysis of human memory CD4 T cells specific for hepatitis C virus using MHC class II tetramers. *Journal of Clinical Investigation* **112**, 831–842 (2003).
132. Jose, E. S., Borroto, A., Niedergang, F., Alcover, A. & Alarcon, B. Triggering the TCR complexes causes the downregulation of nonengaged receptors by a signal transduction-dependent mechanism. *Immunity* **12**, 161–170 (2000).
133. Feucht, J. *et al.* Calibration of CAR activation potential directs alternative T cell fates and therapeutic potency. *Nat Med* **25**, 82–88 (2019).
134. Landgraf, K. E. *et al.* convertible CARs : A chimeric antigen receptor system for flexible control of activity and. 1–13 doi:10.1038/s42003-020-1021-2.
135. Cook, W. J., Choi, Y., Gacerez, A., Bailey-Kellogg, C. & Sentman, C. L. A Chimeric Antigen Receptor That Binds to a Conserved Site on MICA. *Immunohorizons* **4**, 597–607 (2020).
136. Davis, S. J. & van der Merwe, P. A. The kinetic-segregation model: TCR triggering and beyond. *Nature Immunology 2006 7:8* **7**, 803–809 (2006).
137. Rafiq, S., Hackett, C. S. & Brentjens, R. J. Engineering strategies to overcome the current roadblocks in CAR T cell therapy. *Nature Reviews Clinical Oncology* vol. 17 147–167 Preprint at https://doi.org/10.1038/s41571-019-0297-y (2020).
138. A Ajina, J. M. Strategies to address chimeric antigen receptor tonic signaling. *Mol. Cancer Ther.* **17**, 1795–1815 (2018).
139. Prommersberger, S., Hudecek, M. & Nerreter, T. Antibody-Based CAR T Cells Produced by Lentiviral Transduction. *Curr Protoc Immunol* **128**, e93 (2020).
140. Sheih, A. *et al.* Clonal kinetics and single-cell transcriptional profiling of CAR-T cells in patients undergoing CD19 CAR-T immunotherapy. *Nat Commun* **11**, 1–13 (2020).
141. He, Y. *et al.* Multiple cancer-specific antigens are targeted by a chimeric antigen receptor on a single cancer cell. *JCI Insight* **4**, (2019).

142. Stuart, T. *et al.* Comprehensive Integration of Single-Cell Data Resource Comprehensive Integration of Single-Cell Data. *Cell* **177**, 1888-1902.e21 (2019).
143. Korsunsky, I. *et al.* Fast, sensitive and accurate integration of single-cell data with Harmony. *Nat Methods* **16**, 1289–1296 (2019).
144. Locke, F. L. *et al.* Long-term safety and activity of axicabtagene ciloleucel in refractory large B-cell lymphoma (ZUMA-1): a single-arm, multicentre, phase 1–2 trial. *Lancet Oncol* **20**, 31–42 (2019).
145. Gupta, A. & Gill, S. CAR-T cell persistence in the treatment of leukemia and lymphoma. *https://doi-org.proxy.uchicago.edu/10.1080/10428194.2021.1913146* **62**, 2587–2599 (2021).
146. Chavez, J. C., Bachmeier, C. & Kharfan-Dabaja, M. A. CAR T-cell therapy for B-cell lymphomas: clinical trial results of available products. *Ther Adv Hematol* **10**, 2040620719841581 (2019).
147. Kawalekar, O. U. *et al.* Distinct Signaling of Coreceptors Regulates Specific Metabolism Pathways and Impacts Memory Development in CAR T Cells. *Immunity* **44**, 380–390 (2016).
148. Melenhorst, J. J. *et al.* Decade-long leukaemia remissions with persistence of CD4+ CAR T cells. *Nature* **602**, 503–509 (2022).
149. Finney, O. C. *et al.* CD19 CAR T cell product and disease attributes predict leukemia remission durability. *Journal of Clinical Investigation* **129**, 2123–2132 (2019).
150. Neelapu, S. S. CAR-T efficacy: is conditioning the key? *Blood* **133**, 1799–1800 (2019).
151. Turtle, C. J. *et al.* CD19 CAR–T cells of defined CD4+:CD8+ composition in adult B cell ALL patients. *J Clin Invest* **126**, 2123–2138 (2016).
152. Michelozzi, I. M. *et al.* The Enhanced Functionality of Low-Affinity CD19 CAR T Cells Is Associated with Activation Priming and Polyfunctional Cytokine Phenotype. *Blood* **136**, 52–53 (2020).
153. Jackson, Z. *et al.* Sequential single cell transcriptional and protein marker profiling reveals TIGIT as a marker of CD19 CAR-T cell dysfunction in patients with non-Hodgkin's lymphoma. *Cancer Discov* (2022) doi:10.1158/2159-8290.CD-21-1586/696778/SEQUENTIAL-SINGLE-CELL-TRANSCRIPTIONAL-AND-PROTEIN.
154. Hu, Y. *et al.* Antigen multimers: Specific, sensitive, precise, and multifunctional high-avidity CAR-staining reagents. *Matter* **4**, 1–24 (2021).
155. Kallies, A., Zehn, D. & Utzschneider, D. T. Precursor exhausted T cells: key to successful immunotherapy? *Nature Reviews Immunology 2019 20:2* **20**, 128–136 (2019).
156. Utzschneider, D. T. *et al.* Early precursor T cells establish and propagate T cell exhaustion in chronic infection. *Nat Immunol* **21**, 1256–1266 (2020).
157. Galletti, G. *et al.* Two subsets of stem-like CD8+ memory T cell progenitors with distinct fate commitments in humans. *Nature Immunology 2020 21:12* **21**, 1552–1562 (2020).
158. Lesch, S. *et al.* T cells armed with C-X-C chemokine receptor type 6 enhance adoptive cell therapy for pancreatic tumours. *Nature Biomedical Engineering 2021 5:11* **5**, 1246–1260 (2021).
159. Biasco, L. *et al.* Clonal expansion of T memory stem cells determines early anti-leukemic responses and long-term CAR T cell persistence in patients. *Nature Cancer 2021 2:6* **2**, 629–642 (2021).
160. Ning, S., Pagano, J. S. & Barber, G. N. IRF7: Activation, regulation, modification and function. *Genes and Immunity* vol. 12 399–414 Preprint at https://doi.org/10.1038/gene.2011.21 (2011).
161. Tonnerre, P. *et al.* Differentiation of exhausted CD8+ T cells after termination of chronic antigen stimulation stops short of achieving functional T cell memory. *Nature Immunology 2021 22:8* **22**, 1030–1041 (2021).

162. Truong, K. L. *et al.* Killer-like receptors and GPR56 progressive expression defines cytokine production of human CD4+ memory T cells. *Nature Communications 2019 10:1* **10**, 1–15 (2019).
163. Davis, A. M., Ramos, H. J., Davis, L. S. & Farrar, J. D. Cutting Edge: A T-bet-Independent Role for IFN-α/β in Regulating IL-2 Secretion in Human CD4 + Central Memory T Cells. *The Journal of Immunology* **181**, 8204–8208 (2008).
164. Kim, H. J. *et al.* Stable inhibitory activity of regulatory T cells requires the transcription factor Helios. *Science (1979)* **350**, 334–339 (2015).
165. Pesenacker, A. M. *et al.* CD161 defines the subset of FoxP3+ T cells capable of producing proinflammatory cytokines. *Blood* **121**, 2647–2658 (2013).
166. Lee, J. C. *et al.* In vivo inhibition of human CD19-targeted effector T cells by natural T regulatory cells in a xenotransplant murine model of B cell malignancy. *Cancer Res* **71**, 2871–2881 (2011).
167. Zhu, J., Yamane, H. & Paul, W. E. Differentiation of Effector CD4 T Cell Populations*. *http://dx.doi.org/10.1146/annurev-immunol-030409-101212* **28**, 445–489 (2010).
168. Pepper, M. & Jenkins, M. K. Origins of CD4+ effector and central memory T cells. *Nature Immunology 2011 12:6* **12**, 467–471 (2011).
169. Stelekati, E. *et al.* Long-Term Persistence of Exhausted CD8 T Cells in Chronic Infection Is Regulated by MicroRNA-155. *Cell Rep* **23**, 2142–2156 (2018).
170. Chen, Z. *et al.* In vivo CD8+ T cell CRISPR screening reveals control by Fli1 in infection and cancer. *Cell* **184**, 1262-1280.e22 (2021).
171. Svenson, J. L., Chike-Harris, K., Amria, M. Y. & Nowling, T. K. The mouse and human Fli1 genes are similarly regulated by Ets factors in T cells. *Genes & Immunity 2010 11:2* **11**, 161–172 (2009).
172. Li, H. *et al.* Dysfunctional CD8 T Cells Form a Proliferative, Dynamically Regulated Compartment within Human Melanoma. *Cell* **176**, 775-789.e18 (2019).
173. Wherry, E. J. & Kurachi, M. Molecular and cellular insights into T cell exhaustion. *Nat Rev Immunol* **15**, 486–499 (2015).
174. Mamonkin, M., Puppi, M. & Lacorazza, H. D. Transcription factor ELF4 promotes development and function of memory CD8+ T cells in Listeria monocytogenes infection. *Eur J Immunol* **44**, 715–727 (2014).
175. Lee, J. Y. *et al.* The Transcription Factor KLF2 Restrains CD4+ T Follicular Helper Cell Differentiation. *Immunity* **42**, 252–264 (2015).
176. Chen, P. H. *et al.* Activation of CAR and non-CAR T cells within the tumor microenvironment following CAR T cell therapy. *JCI Insight* **5**, (2020).
177. Shah, N. N. *et al.* Clonal expansion of CAR T cells harboring lentivector integration in the CBL gene following anti-CD22 CAR T-cell therapy. *Blood Adv* **3**, 2317–2322 (2019).
178. Goldberg, L. *et al.* Single-cell analysis by mass cytometry reveals CD19 CAR T cell spatiotemporal plasticity in patients. *Oncoimmunology* **11**, (2022).
179. Li, X. *et al.* Single-Cell Transcriptomic Analysis Reveals BCMA CAR-T Cell Dynamics in a Patient with Refractory Primary Plasma Cell Leukemia. *Molecular Therapy* **29**, 645–657 (2021).
180. Chen, G. M. *et al.* Integrative bulk and single-cell profiling of pre-manufacture T-cell populations reveals factors mediating long-term persistence of CAR T-cell therapy. *Cancer Discov* candisc.1677.2020 (2021) doi:10.1158/2159-8290.cd-20-1677.
181. Zhao, Z. *et al.* Structural Design of Engineered Costimulation Determines Tumor Rejection Kinetics and Persistence of CAR T Cells. *Cancer Cell* **28**, 415–428 (2015).
182. Stoeckius, M. *et al.* Simultaneous epitope and transcriptome measurement in single cells. *Nature Methods 2017 14:9* **14**, 865–868 (2017).

183. What is Cell Ranger? -Software -Single Cell Gene Expression -Official 10x Genomics Support. https://support.10xgenomics.com/single-cell-gene-expression/software/pipelines/latest/what-is-cell-ranger.
184. Hao, Y. *et al.* Integrated analysis of multimodal single-cell data. *Cell* **184**, 3573-3587.e29 (2021).
185. Wu, T. *et al.* clusterProfiler 4.0: A universal enrichment tool for interpreting omics data. *The Innovation* **2**, (2021).
186. Subramanian, A. *et al.* Gene set enrichment analysis: A knowledge-based approach for interpreting genome-wide expression profiles. *Proc Natl Acad Sci U S A* **102**, 15545–15550 (2005).
187. Aibar, S. *et al.* SCENIC: Single-cell regulatory network inference and clustering. *Nat Methods* **14**, 1083–1086 (2017).
188. van de Sande, B. *et al.* A scalable SCENIC workflow for single-cell gene regulatory network analysis. *Nature Protocols 2020 15:7* **15**, 2247–2276 (2020).
189. PBMC10k_downstream-analysis. http://htmlpreview.github.io/?https://github.com/aertslab/SCENICprotocol/blob/master/notebooks/PBMC10k_downstream-analysis.html.
190. Kuhn, M. Building Predictive Models in R Using the caret Package. *J Stat Softw* **28**, 1–26 (2008).
191. Tianqi, C. & Guestrin, C. XGBoost: A Scalable Tree Boosting System. *KDD* (2016).
192. Lundberg, S. M. & Lee, S. I. A Unified Approach to Interpreting Model Predictions. *Adv Neural Inf Process Syst* **2017-December**, 4766–4775 (2017).
193. Liu, Y. & Just, A. SHAPforxgboost: SHAP Plots for 'XGBoost'. Preprint at https://github.com/liuyanguu/SHAPforxgboost/ (2020).
194. Bergen, V., Lange, M., Peidli, S., Wolf, F. A. & Theis, F. J. Generalizing RNA velocity to transient cell states through dynamical modeling. *Nature Biotechnology 2020 38:12* **38**, 1408–1414 (2020).
195. RNA Velocity Basics — scVelo 0.2.5.dev6+g1805ab4.d20210829 documentation. https://scvelo.readthedocs.io/VelocityBasics/.
196. la Manno, G. *et al.* RNA velocity of single cells. *Nature 2018 560:7719* **560**, 494–498 (2018).
197. Wolf, F. A., Angerer, P. & Theis, F. J. SCANPY: Large-scale single-cell gene expression data analysis. *Genome Biol* **19**, 1–5 (2018).
198. Street, K. *et al.* Slingshot: Cell lineage and pseudotime inference for single-cell transcriptomics. *BMC Genomics* **19**, 1–16 (2018).
199. ImmunoMind Team. immunarch: An R Package for Painless Bioinformatics Analysis of T-Cell and B-Cell Immune Repertoires. Preprint at https://doi.org/10.5281/zenodo.3367200 (2019).
200. Crouse, J., Kalinke, U. & Oxenius, A. Regulation of antiviral T cell responses by type I interferons. *Nature Reviews Immunology* vol. 15 231–242 Preprint at https://doi.org/10.1038/nri3806 (2015).
201. Cho, S. S. *et al.* Activation of STAT4 by IL-12 and IFN-alpha: evidence for the involvement of ligand-induced tyrosine and serine phosphorylation. *The Journal of Immunology* **157**, (1996).
202. Huber, J. P., Ramos, H. J., Gill, M. A. & Farrar, J. D. Cutting Edge: Type I IFN Reverses Human Th2 Commitment and Stability by Suppressing GATA3. *The Journal of Immunology* **185**, 813–817 (2010).
203. Ramgolam, V. S., Sha, Y., Jin, J., Zhang, X. & Markovic-Plese, S. IFN-β Inhibits Human Th17 Cell Differentiation. *The Journal of Immunology* **183**, 5418–5427 (2009).

204. Curtsinger, J. M., Valenzuela, J. O., Agarwal, P., Lins, D. & Mescher, M. F. Cutting Edge: Type I IFNs Provide a Third Signal to CD8 T Cells to Stimulate Clonal Expansion and Differentiation. *The Journal of Immunology* **174**, 4465–4469 (2005).
205. Ramos, H. J. *et al.* Reciprocal responsiveness to interleukin-12 and interferon-α specifies human CD8+ effector versus central memory T-cell fates. *Blood* **113**, 5516–5525 (2009).
206. Li, S. F. *et al.* Type i interferons: Distinct biological activities and current applications for viral infection. *Cellular Physiology and Biochemistry* vol. 51 2377–2396 Preprint at https://doi.org/10.1159/000495897 (2018).
207. Lee, J. S. & Shin, E. C. The type I interferon response in COVID-19: implications for treatment. *Nature Reviews Immunology* vol. 20 585–586 Preprint at https://doi.org/10.1038/s41577-020-00429-3 (2020).
208. Musella, M., Manic, G., de Maria, R., Vitale, I. & Sistigu, A. Type-I-interferons in infection and cancer: Unanticipated dynamics with therapeutic implications. *Oncoimmunology* **6**, 1–12 (2017).
209. Karimi, M. A. *et al.* Measuring Cytotoxicity by Bioluminescence Imaging Outperforms the Standard Chromium-51 Release Assay. *PLoS One* **9**, e89357 (2014).
210. Ramos, H. J. *et al.* Reciprocal responsiveness to interleukin-12 and interferon-α specifies human CD8+ effector versus central memory T-cell fates. *Blood* **113**, 5516–5525 (2009).
211. Weigelin, B. *et al.* Cytotoxic T cells are able to efficiently eliminate cancer cells by additive cytotoxicity. *Nature Communications 2021 12:1* **12**, 1–12 (2021).